Master's thesis

NTNU
Norwegian University of Science and Technology
Faculty of Engineering
Department of Marine Technology

Caspar Cappelen Smith

Mooring system and hydrodynamic analysis of a closed fish cage using the BIEM method

Master's thesis in Marine Technology
Supervisor: Pål Lader
June 2019

NTNU
Kunnskap for en bedre verden

Caspar Cappelen Smith

Mooring system and hydrodynamic analysis of a closed fish cage using the BIEM method

Master's thesis in Marine Technology
Supervisor: Pål Lader
June 2019

Norwegian University of Science and Technology
Faculty of Engineering
Department of Marine Technology

NTNU
Norwegian University of
Science and Technology

Preface

The scope of this paper is to analyze mooring systems used in the aquaculture industry and to investigate if they have the necessary strength to support implementation of closed containment technology. To do this, dynamic and static analysis have been performed using WAMIT, accounting for wave forces. In addition, current forces have been investigated using Morison's Equation. The forces and motions are used directly in a mooring system analysis, conducted for one mooring line in an orthogonal mooring system.

I would like to thank my main Supervisor Professor Pål Lader, NTNU/SINTEF Ocean, Research Scientist Per Christian Endresen at SINTEF Ocean and professor II Kjell Larsen, NTNU, for excellent guidance and informative meetings throughout the process. I would also like to thank senior scientist David Kristiansen, NTNU/SINTEF Ocean for providing critical information in the start-up phase of the project.

Trondheim, July 2019

Caspar Cappelen Smith

Abstract

As the number one producer of Atlantic salmon, the Norwegian aquaculture industry is growing rapidly. The success is closely connected to the use of so-called net-based structures, taking advantage of the rich and prosperous Norwegian environmental conditions. Due to the rapid growth and nature of the open net-based facilities, the industry is faced with numerous environmental challenges including fish escape, pollution, disease and infectious parasites in the form of sea lice. As well as affecting the ongrowing salmon within the facilities, it affects natural habitats, causing major threat to a large number of natural species.

A possible solution showing great promise is the closed flexible fish cage (CFFC), produced in the form of independent structures or as membranes customized for implementation in already existing facilities. This paper investigates the hydrodynamic forces and motions on four different geometries inspired by the CFFC Botngaard design. The forces and motions are further used to evaluate the integrity of a traditional mooring system suspected to high and substantial exposure for waves, and substantial exposure for current. This is to investigate if traditional mooring grid systems used by the industry can withhold increased forces connected to closed containment technology.

Due to its increased mass, CFFC facilities share many of the same characteristics as offshore structures, widely different from open net-based fish farm facilities. In addition to increased mass, as of today, there are few large volume ocean-based structures having flexible properties with a free surface.

Using the BIEM and low order panel method implemented in the simulation software WAMIT based on linear and potential wave theory, the motion of the structures has been found in the form of RAO's in the wave frequency regime, including second-order nondimensional mean drift force coefficients. Forces from uniform current has been found using Morison's equation. Combining the results with high wave and substantial current exposure, forces and motions show that the top side tension of the mooring lines in the orthogonal mooring system is either in the vicinity or exceeding material properties and operational limits. Lowering the wave exposure to substantial improves the operational limits, but the bridle lines stretching from the connector plate to the top side connection point is still outside operational limits. This can be solved by exchanging the components with the more robust supertec 8 ropes used in the anchor line component of the system.

The internal sloshing problem has been investigated in the dynamic and static analysis in WAMIT, responding well with recognized literature when interpreting the outcome from the different tests. In addition, similar investigations confirm that the results from the static and dynamic analysis give realistic results for the different simulations.

Modeling the stiffness from the bottom chain and damping from viscous effects linearly in WAMIT makes the analysis suspect to uncertainty, especially when evaluating the mooring system integrity. In addition, the mooring system analysis has been carried out from solely evaluating the top side tension in one mooring line, neglecting the elasticity of the rope components. There is also uncertainty tied to nonlinear effects such as slowly varying drift forces, which has been evaluated purely based on a qualitative evaluation based on similar research carried out by other actors.

Overall, it is evident that the mooring system should be investigated more closely using numerical software considering nonlinear effects. In addition, more attention on the elasticity of the bag, and its effect on mooring system integrity should be carried out in future work.

Contents

List of Figures

List of Tables

Nomenclature

Abbreviations

$BIEM$	Boundary integral equation method
$CFFC$	Closed flexible fish cage
EQM	Equation of motion
FAO	Food and Agriculture Organization of the United Nations
FRC	Force file in WAMIT
GDF	Geometry file in WAMIT
$HDPE$	High density polyethylene
KC	Keulegan carpenter number
PN	Nominal pressure ratio
POT	Potential file in WAMIT
RAO_i	Response amplitude operator in i-direction
SDR	Standard dimension ratio
$WAMIT$	Wave Analysis At Massachusetts Institute of Technology

Boundary conditions

Ω	Fluid domain
n_k	Normal vector in x, y and z direction for k = 1,2,3 respectively
S_B	Body surface boundary
S_b	Surface area of body
S_{FS}	Free surface boundary
S_k	Surface area of panels defining the body surface
S_{SB}	Bottom boundary

S_T	Surface area of internal tank
U_N	Normal component of body surface velocity
V	Velocity vector
V_N	Normal component of the fluid velocity

Constants

ν	Viscosity of seawater
ρ / ρ_{sea}	Density of sea water
ρ_s	Density of steel
C_d	Drag coefficient
E	Elastic modulus
g	Acceleration of gravity

Forces and motions

ΔP	Pressure difference
ΔT_H	Difference in horizontal mooring line tension between two different tension states
ΔX	Offset in x -direction
η_j	Motion in Surge, Sway, Heave, Roll, Pitch and Yaw for j = 1,...,6 respectively
η_{jA}	Amplitude of motion in Surge, Sway, Heave, Roll, Pitch and Yaw for j = 1,...,6 respectively
$\overline{F}_{(md)}$	Nondimensional mean drift coefficient
F_D / F_C	Drag force / force from current
F_R	Restoring force
F_S	Force acting on the body surface
F_T	Forces exerted on the structure from the tank fluid
F_V	Force acting on the fluid volume
$F_{(lin)}$	Linear damping force
$F_{(qd)}$	Quadratic damping force
F_{dyn}	Maximum dynamic force obtained from most likely maximum dynamic offset X_{dyn}^{max}

F_{env}	Forces from environmental effects
$F_{i\,(c)}$	Total mean drift force in i-direction
$F_{i\,(md\,tot)}$	Total mean drift force in i-direction
$F_{i\,(md)}$	Mean drift force in i-direction
$F_{i\,exc}$	Excitation force in i-direction
$F_{i\,rad}$	Radiation force in i-direction
$F_{x\,tot}$	Total force from environmental effects in x-direction
M_B	Rolling moment from change in displaced volume
M_D	Rolling moment from free surface effect
P	Pressure
P_{dyn}	Dynamic pressure
P_{quad}	Quadratic pressure
P_{stat}	Hydrostatic pressure
S_k	Motion in x, y and z direction including translatory and angular motion for k = 1,...,3 respectively
T_H	Horizontal mooring line tension
T_V	Vertical mooring line tension
T_{des}	Inline design tension
$T_{H\,pre}$ / T_{Hp}	Mooring line horizontal pretension
$T_{Hx\,line}$	Mooring line tension in x-direction
$T_{Hx\,max}$	Limit state before vertical forces on anchor
$T_{Hx\,pre}$	Mooring line pretension in x-direction
T_{Hx}	Mooring line tension in x-direction
T_{line}	In-line mooring line tension
$X_{current}$	Offset from current
X_{drift}	Offset from mean wave drift force
X_{dyn}	Offset from dynamic motion

X_{dyn}^{max}	Maximum offset from dynamic motion
X_{mean}	Offset from mean effects

Functions used by WAMIT

$G(\boldsymbol{\xi}\,;\boldsymbol{x})$	The Green function
H_θ	Kochin function
$J_0\,(KR)$	Bessel function of zero order

Mooring system parameters and notation

γ_l	Load factor
γ_m	Material factor
A_B	Cross section of bridle line rope
A_R	Cross section of anchor line rope
$B_1, ..., B_3$	ID's for Different bridle line ropes
$C_1, ..., C_6$	ID's for different bottom chains and chain layouts
h_c	Vertical extension of chain, from anchor to P_1 connection point
h_R	Vertical extension of anchor line rope, from P_1 to P_3
k_B	Stiffness of bridle lines
k_C	Stiffness of bottom chain
k_e	Elastic stiffness
k_g	Geometric stiffness
k_M	Stiffness of complete mooring line
k_R	Stiffness of anchor line rope
K_{11}	Total system stiffness in surge due to surge motion
K_{22}	Total system stiffness in sway due to sway motion
K_{66}	Total system stiffness in yaw due to yaw motion
L_C	Length of bottom chain
L_R	Length of mooring line rope

l_s	Active part of bottom chain
$M_1, ..., M_6$	ID's for different mooring lines consisting of chains, anchor line ropes and bridles
MBL	Mean breaking load
$R_1, ..., R_6$	ID's for different anchor line ropes and rope layouts
W_a	Weight In air
W_w	Weight In water
X_C	Horizontal extension of bottom chain
X_R	Horizontal extension of anchor line rope
X_t	Horizontal extension of from anchor to connector plate P_3

Coefficients

A_{ij}	Added mass in i-direction due to motion in j-direction
$B^{(1)}$	linear damping coefficient for linear damping outside potential damping
$B^{(2)}$	Linearized quadratic damping coefficient
$B^{(cr)}$	Critical damping
B_{ij}	Potential damping coefficient in i-direction due to motion in j-direction
$B_{ij}^{(e)}$	User specified Damping coefficient in i-direction due to motion in j-direction
B_{lin}	Linear damping coefficient
B_{qd}	Quadratic damping coefficient
C_{ij}	Stiffness coefficient in i-direction due to motion in j-direction
M_{ij}	Mass in i-direction due to motion in j-direction
$M_{ij}^{(e)}$	User specified Mass in i-direction due to motion in j-direction
p_1	Linear coefficient used to find linear damping coefficient
p_2	quadratic coefficient used to find quadratic damping coefficient

System parameters and notation

A	Cross section area

A_m	Projected area of membrane
$B(O)$	Body fixed coordinate system
D_1	Diameter from center of structure to center of first floating collar
$D_1, ..., D_4$	ID's for the four different designs
D_2	Diameter from center of structure to center of second floating collar
D_m	Diameter of membrane
D_p	Diameter of floating collar pipe
$E(O)$	Earth fixed coordinate system
G	Center of gravity
G'	Displaced center of gravity
H/H_m	Drought of structure
H_d	Drought of model used in decay test
H_{liq}	Height of liquid within structure
I_{xy} / I_{xy}	Moment of inertia
M_m	Mass of membrane
M_p	Mass of pipe in floating collar
M_T	Total mass of structure excluded water-filling
R_1	Radius from center of structure to center of first floating collar
R_2	Radius from center of structure to center of second floating collar
R_d	Radius of model used in decay test
R_m	Radius of membrane
r_{xy} / r_{xy}	Radius of gyration
T_{1n}	Eigenperiod of structure in surge
z_g	Center of gravity

Other symbols

β	Heading angle

δ	Logarithmic decrement
$\boldsymbol{\xi}$	Point source
ζ	Damping ratio
L^k	Characteristic length defined by the geometry file in WAMIT
t	Time
T_m	Mean period between oscillations
V_c	Current velocity
x_i	Point on the body surface denoting panel centroids in the low order panel method

Velocity potentials

ϕ_1	Total first-order velocity potential
ϕ_B	Sum of scattering and radiation velocity potential
$\phi_{(k)}$	Velocity potential over the k'th panel using the low order panel method
ϕ_{01} / φ	First-order wave velocity potential
ϕ_0	First-order wave velocity potential
ϕ_D	First-order velocity potential for diffraction problem
ϕ_j	First-order unit amplitude velocity potential in the j'th mode
ϕ_R	First-order velocity potential for radiation problem
ϕ_S	First-order velocity potential for Scattering problem

Wave properties

ϵ	Random phase angle between 0 and 2π
λ	Wave length
ω_j	Frequency of the j'th wave in any given sea state
ω_p	Peak wave frequency
σ_x	Standard deviation of response spectrum
ζ_A	Wave amplitude for regular waves
$\zeta_{(t)}$	Wave elevation irregular sea state

ζ_{max}	maximum wave amplitude from regular waves
H	Wave height
h	water depth
H_s	Significant wave height
K	Wave number for deep water waves
k	Generalized wave number
$S(\omega)_m$	Maximum spectral energy in sea state
$S_{(\omega)}$	Wave spectrum
$S_{x(\omega)}$	Response spectrum
$S_x(\omega)_m$	Maximum spectral energy in response spectrum
T	Wave period
T_L	Eigenperiod of internal water mass
T_p	Peak wave period
T_z	Zero up-crossing period

1 Introduction

Since its start in the 1970s the Norwegian aquaculture industry has seen major growth. In 2016, revenue from fish farming alone was 63 billion NOK, making it the second most profitable sector prior to oil and gas. The major increase in fish farm facilities in fjords and numerous locations along the Norwegian coastline has lead to more pollution and environmental concerns for natural habitats and ecosystems. Also, during recent times, the farmed fish itself has been prone to infectious fish lice and other parasites, leading to reduced fish welfare and loss of revenue.

To deal with the problems and make future fish farming more sustainable, the industry is investigating different solutions and designs. Many of these solutions revolve around Closed Containment technology, where the surrounding water is separated from the internal water mass. This makes the structures highly different from traditional net-based structures, giving farmers more control regarding waste and exposure to external threats.

Numerous different designs are being investigated by different actors in the aquaculture industry. To differentiate between the different solutions, the industry mainly categorize closed fish farm designs into three main groups based on material properties and physical behavior, as illustrated in figure 1.

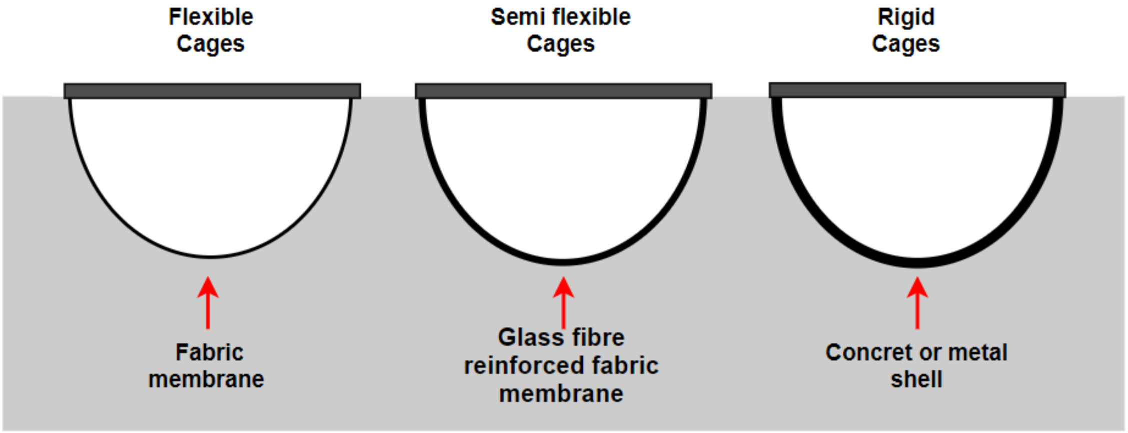

Figure 1: Main classes of closed fish farm designs

Compared to traditional net-based structures, closed containment systems have largely different physical behavior and properties. Most importantly, they have significantly increased mass due to the internal water volume being part of the structure mass, and a closed membrane, which makes them prone to amplified loads and motions when suspected to environmental forces from waves and current.

Many solutions that are already developed or are in development by the industry, is based on implementation at already existing fish farm locations. This means that in many cases, the mooring systems designed for net-based technology must be able to absorb amplified forces when used in connection with closed technology. Mooring system failure can in many cases lead to devastating results, connected to fish escape or structural damage. Also, with the increased mass of closed systems, damage to third-party actors can be significantly worse in the case of mooring line failure and drift off to nearby installations.

This calls for further investigation of mooring system integrity to evaluate if existing systems utilized by the aquaculture industry has the necessary strength, or needs to be improved to assure safe operation when implementing closed technology.

1.1 Motivation

By 2050 UN estimates that the world population will grow to approximately 9.7 billion. The ocean covers 70% of the earth‘s surface, but despite the large surface area, only 6% of the protein source for human consumption originates from the sea. To assure a sustainable future, this number has to be increased. Aquaculture is the fastest growing animal based food producing sector and Norway is a major contributor. In 2015 aquaculture alone supplied the market with 50% of supplies meant for human consumption. Atlantic salmon is the third most important fish species when it comes to raw volume, as illustrated in figure 2, and Norway is the worlds largest supplier [4].

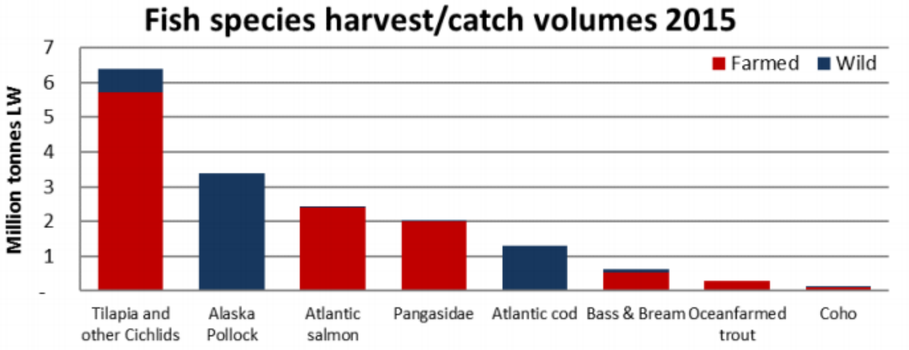

Figure 2: Harvest and catch volumes of most valuable fish species [4]

Norway‘s success in the aquaculture industry comes from years of experience and technological developments. To this day, the use of gravitational net based cages are still dominating the industry due to their simple and cost-efficient design, but has in recent times been found to pose a great threat to natural species and the environment itself. As one of the world leading actors, Norway should always strive to find new and innovative solutions that contribute to a more sustainable future. To address the problems listed above, the Norwegian government is continuously issuing technology development licenses to encourage companies to invest in new and innovative solutions [40].

Closed containment systems bring benefits with regards to fish escape, which is often connected to salmon lice treatment or structural failures in net-based facilities. Also, as the internal water mass is separated from the surrounding water, higher survival rates among the ongrowing salmon are expected together with a decrease in loss of feed. This comes at the cost of higher structural expenses and the will to invest in new solutions without the insurance of a beneficial outcome. This makes investigating into closed containment systems highly relevant, improving its viability for future use [37].

1.2 Scope of work and limitations

This thesis investigates a conventional mooring system used in a typical fish farm location, which due to acceptable environmental conditions could be relevant for merging with closed fish farm technology. The analysis is performed for a single closed containment structure leaving multiple body analysis for further work. This is to simulate a realistic scenario, investigating if a traditional grid mooring system used in the aquaculture industry can withhold the increased forces from closed technology. The mooring system analysis is force driven, rather than using the horizontal displacement of the system when suspected to environmental forces.

To do this, the computational software WAMIT (Wave Analysis at Massachusetts Institute of Technology) is used to numerically estimate the horizontal hydrodynamic forces and motions induced by waves on four different geometries, including a hemispherical and different semi-ellipsoid shaped designs. The software is based on linear and potential wave theory and is limited to first-order and mean drift forces. This means that second-order low and difference frequency effects are neglected throughout the analysis, but included when qualitatively discussing their possible consequences. In addition, uniform current has been treated from one direction using Morison's equation.

As the WAMIT software is limited to linear theory and potential wave theory, the dynamic analysis yields RAO's in the frequency domain. To account for irregular wave effects, the RAO's are used in combination with a Pierson Moskowitz wave spectrum to obtain a Response spectrum that is used to find the most probable horizontal offset of the system. The PM spectrum is also used in combination with transfer functions obtained for the mean drift forces to find the total drift force affecting the system.

The mooring system is represented in the dynamic analysis as horizontal stiffness, modeled in the user-specified stiffness matrix in WAMIT. The horizontal stiffness is assumed to origin from the geometrical stiffness provided by the bottom chain of the mooring system and elastic stiffness from the different rope components. Here, different mooring systems providing various stiffness to the different designs have been tested. In the WAMIT simulation, the stiffness is modeled as a linear coefficient, which is prone to deviations from real-time results due to the nonlinear nature of the geometric stiffness provided by the bottom chain.

In addition, damping effects outside potential theory is modeled in the user-specified damping matrix, using a Decay test performed in the SJØFLO project by SINTEF Ocean [8]. The decay test is used to evaluate a reasonable percentage of critical damping added to the linear damping matrix. This is mainly to account for viscous effects from vortex shedding and friction in the wave-body interaction problem.

All designs are treated as rigid, neglecting the possibility of elastic behavior concerning flexible and semi-flexible cages. This means that the rigid body motions dominate the dynamic behavior of the structure and the RAO's resulting from the numerical analysis in WAMIT. When modeling the structures, MATLAB has been used to create panels representing the geometry of the structure, using the low order panel method in WAMIT. Here, only the underwater part of the structure has been considered, while the top side affected by wind and waves has been neglected.

Wave and current conditions have been chosen according to NS9415‘s cite classification, limited to high exposure for waves and substantial exposure for current. The classifications have been chosen according to common exposure for net-based structures. In addition, substantial exposure for waves has been considered when evaluating if it is beneficial to lower the wave exposure, concerning operational limits for the mooring system. The thesis is a continuation of a pilot study named *Forces and motions of a flexible closed containment system and its influence on present mooring system integrity in aquaculture. A prestudy*.

1.3 Fish farming in Norway

First attempts of aquaculture in Norway dates back to 1850 when the first brown trout *Salmo trutta trutta* hatched with help of human intervention. After the Second World War, the interest for fish farming increased. This led to the first successful transfer of rainbow trout to seawater and the first successful attempt of ongrowing Atlantic salmon in the 1960s. In the 1970s the cage culture was introduced through a technological leap when land based structures were replaced by sea-based cage‘s. In the following years, the Norwegian coastline proved to be an excellent breeding ground for aquaculture intensive fish farming [5].

The CFFC concept was already known to the aquaculture industry in the late 80s. One of the first structures was tested at a trial station in Matre, a small town in Masfjorden in Norway in 1988. In the 1990s a similar facility was established at Støytland Fisk in Flekkefjord to avoid poisonous algae, threatening the smolt production in the area. Later the technology was adopted to a larger scale in Arendal in 1992, but failed due to large ruptures in the fabric leading to total capsize of the structure. Since then, the use of closed flexible technology has been limited, but in recent times different designs have gotten more attention due to rising environmental concerns and loss of revenue during production [37].

1.3.1 Environmental conditions and Bathymetry

This thesis takes a general approach concerning closed containment systems and their locations. This means that no particular fish farm location including data from the said location has been evaluated. The general approach means that test conditions have been chosen according to NS9415, classifying fish farm locations according to wave and current conditions as illustrated in table 1 and 2.

Site classification	Significant wave height (H_S) [m]	Peak wave period (T_p) [s]	Site exposure level
$\boldsymbol{A}$	0.0 - 0.5	0.0 - 2.0	Low
$\boldsymbol{B}$	0.5 - 1.0	1.6 - 3.2	Moderate
$\boldsymbol{C}$	1.0 - 2.0	2.5 - 5.1	Substantial
$\boldsymbol{D}$	2.0 - 3.0	4.0 - 6.7	High
$\boldsymbol{E}$	3.0 <	6.7 - 18.0	Extreme

Table 1: Wave exposure classification according to NS9415

Site classification	Current speed (V_c) [m/s]	Site exposure level
$\boldsymbol{A}$	0.0 - 0.3	Low
$\boldsymbol{B}$	0.3 - 0.5	Moderate
$\boldsymbol{C}$	0.5 - 1.0	Substantial
$\boldsymbol{D}$	1.0 - 2.5	High
$\boldsymbol{E}$	1.5 <	Extreme

Table 2: Current exposure classification according to NS9415

As CFFC solutions can be used to close already existing net-based structures, the solutions must be able to maintain its integrity in harsh conditions. According to [15], traditionally used HDPE cages are certified and designed for significant wave height (H_s) of 3 meters and current strength (V_c) of 1.5 m/s. However, it is important to remember that the largely increased mass of CFFC structures could limit the operational conditions due to enhanced loads and motions. This means that the test conditions in this paper have been limited to high wave exposure and substantial current conditions, with the addition of investigating the possibility of lowering the wave exposure to substantial if found necessary when analyzing the mooring system [43].

By examining typical fish farm locations along the Norwegian coastline using maps made by *The Norwegian Directorate of fisheries* the bathymetry for many locations seems to roughly vary between $50-250$ meters. Based on this information a mean water depth of 100 meters has been chosen when evaluating the fish farm system.

1.3.2 Wave properties and characteristics

The water depth has significant effect on the mooring system layout, but also regarding the validity of different criteria used in linear wave theory. This parameter is especially important for wave propagation and behavior, deciding if it is reasonable to assume deep water waves when using and estimating the velocity potentials. To check if deep water wave approximation is valid the wavelength can be calculated using the correlation between wave period (T) and wavelength (λ) through an iterative process, setting a large value for the wavelength included in the expression for wavenumber (k) seen in equation 1. By several steps, this iterative process gives an accurate estimate of the wavelength [12] (Chapter 2).

When performing this process for high exposure $H_s \in [2, 3]$ meters and $T_p \in = [4.0, 6.7]$ seconds for relevant wave periods (T) using the PM-spectrum in figure 4, and the chosen water depth of h = 100 meters, $\lambda < 2h$ which means that deep water waves can be assumed.

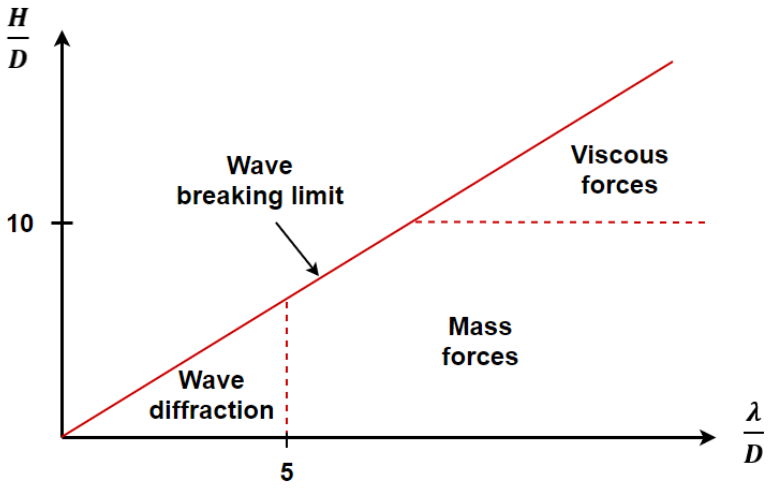

Figure 3: Relative importance of wave forces on a cylindrical bottom based marine structure

By using the graph showing the relative importance of wave forces on a cylindrical bottom based marine structure from [12] (Chapter 1) illustrated in figure 3, it is possible to make a rough estimate of important force contributions affecting a CFFC structure.

$$\lambda = \frac{g}{2\pi} T^2 \tanh{(kh)} \tag{1}$$

With a fish farm diameter of D = 40 meters, long wave approximation cannot be assumed (λ/D $\leq$ 5), due to the large significance of diffraction forces as illustrated in figure 3. This estimate gives a valuable initial picture of the different force contributions affecting the structure ahead of the simulation, but is prone to deviations due to the floating characteristics and different geometrical shapes between the CFFC structure and a bottom based cylindrical facility [12] (Chapter 1).

Figure 4 highlights the PM-spectrum relevant for high wave exposure according to NS9415. From the spectrum it can be seen that relevant wave periods include approximately $T \in$ [2,10] seconds. The spectrum is according to [46].

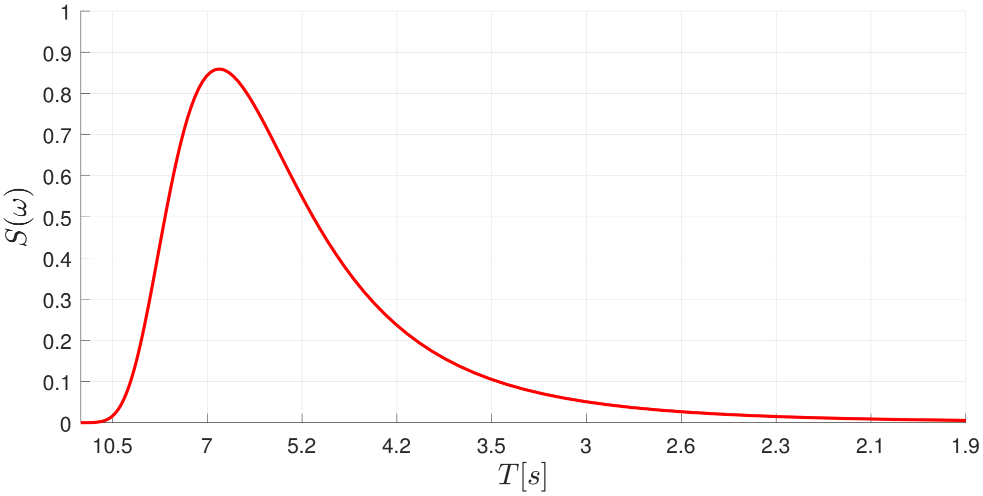

Figure 4: PM-spectrum for T_p = 6.7 seconds and H_s = 3.0 meters

2 Theoretical Background

This paper aims to analyze the mooring system of a CFFC fish farm structure through computational simulation of the facility. The following section will describe the methods and principles used to find the hydrodynamic forces resulting in static and dynamic offset experienced by the structure when suspected to sea loads. The dynamic motion is found by solving the Equation of motion (EQM) in WAMIT accounting for first-order forces, used to find Response Amplitude Operators (RAO's) for different wave amplitudes and frequencies. Free surface effects will be accounted for as WAMIT has the ability to estimate the effect of internal water mass, important for closed fish farm facilities. The static displacement is found from using the nondimensional mean wave drift forces coefficients obtained from WAMIT and drag force from current, using Morison's equation. A short description of the different force contributions, including numerical methods and their physical origin will be presented. Further, equations applicable when combining the data from WAMIT with irregular sea states will be presented.

Naturally, in addition to the hydrodynamic theory underlying the WAMIT software, equations and literature utilized in the evaluation of the integrity of the mooring system will be emphasized. Before discussing the hydrodynamic force contributions and mooring line properties, the translatory and angular motions used in WAMIT together with a presentation of the rigid body motions will be presented.

2.1 Rigid body motions

When analyzing marine structures affected by forces from waves and current, and before further theory can be presented, the rigid body motions have to be defined. The three dimensional translation and angular rotation experienced by the body when suspected to forces are well defined and standardized within the marine industry, widely known as the Six degrees of freedom.

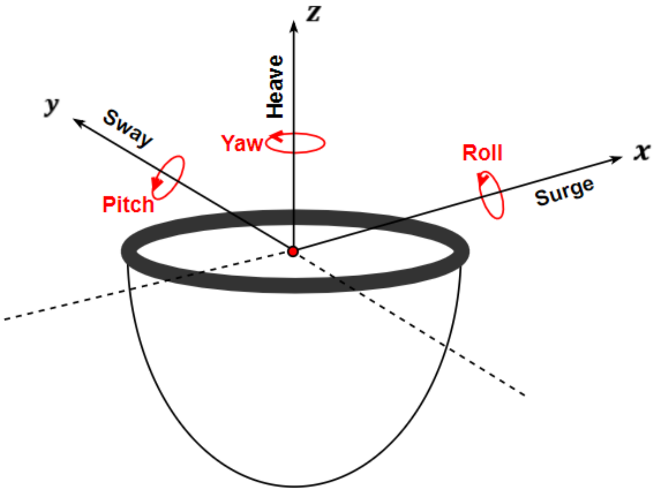

Figure 5: Definition of the the Six degree's of freedom (6 DOF) relative to the body coordinate system

The oscillatory translatory motions are referred to as Surge, Sway and heave, denoted η_1, η_2 and η_3 respectively. The oscillatory angular motions are referred to as Roll, Pitch and Yaw denoted η_4, η_5 and η_6 respectively. All six degree's of freedom can be seen in figure 5. For wave frequency motion, a fixed coordinate system defined in the mean position of the body can be used. This can be justified by the relatively small motions in the wave frequency regime [16] (Chapter 2).

With the translatory and angular motions relative to each respective axis denoted in figure 5 the motion of an arbitrary point on the body can be expressed by equation 2.

$$\boldsymbol{s} = \eta_1 i + \eta_2 j + \eta_3 k + \boldsymbol{\alpha} \times \boldsymbol{r} \tag{2}$$

Here, $\boldsymbol{\alpha}$ denotes the angular motions and $\boldsymbol{r}$ denotes the distance from the coordinate system in the mean free surface to the point of interest on the body.

Expressions for $\boldsymbol{\alpha}$ and $\boldsymbol{r}$ are defined in equation 3 and 4 respectively.

$$\boldsymbol{\alpha} = \eta_4 i + \eta_5 j + \eta_6 k \tag{3}$$

$$\boldsymbol{r} = xi + yj + zk \tag{4}$$

Taking the cross product between the angular motions ($\boldsymbol{\alpha}$) and the distance from the body coordinate system to the point of interest on the body ($\boldsymbol{r}$) yields the expression seen in equation 5.

$$\boldsymbol{\alpha} \times \boldsymbol{r} = \begin{bmatrix} i & j & k \\ \eta_4 & \eta_5 & \eta_6 \\ x & y & z \end{bmatrix} = (z\eta_5 - y\eta_6)i + (x\eta_6 - z\eta_4)j + (y\eta_4 - x\eta_5)k \tag{5}$$

Adding the cross product of the angular motion and the distance vector yields the contribution from angular motion to translatory motion as seen in equation 6.

$$\boldsymbol{S} = \underbrace{(\eta_1 + z\eta_5 - y\eta_6)i}_{\boldsymbol{S_1}} + \underbrace{(\eta_2 + x\eta_6 - z\eta_4)j}_{\boldsymbol{S_2}} + \underbrace{(\eta_3 + y\eta_4 - x\eta_5)k}_{\boldsymbol{S_3}} \tag{6}$$

Here, $\boldsymbol{S_1}$, $\boldsymbol{S_2}$ and $\boldsymbol{S_3}$ are the motion in x, y and z-direction respectively. This means that the translatory motion at any point on the rigid body is dependent on the translatory motion itself, and the product between the angular motion the coordinates of the point of interest. The origin of the system is where the structure experiences angular motions, which means that angular motions will have a larger effect on the translatory motion further from the coordinate system [12] (Chapter 3).

Through the paper, the subscripts j = 1,...,6 will denote the direction of the motion, whilst i = 1,...,6 will denote the direction of the force, moment, different coefficients and so on, arising due to the body motion.

2.2 Sea loads from waves and current

The following sections target to present a theoretical overview, including methods to estimate forces and motions important for the static and dynamic analysis. The equation of motion used in the dynamic analysis to estimate the 6 DOF system will be presented, focusing on the first-order response in the horizontal plane due to its importance for mooring system integrity. As the dynamic analysis is based on linear theory, first-order forces from waves including excitation and radiation forces will be emphasized, neglecting second-order forces from sum and difference frequency effects.

The static analysis will account for mean wave drift and forces from current, which is treated as uniform through the water column. table 3 illustrates an overview of the sea loads including the excitation regimes evaluated in the static and dynamic analysis.

Excitation source	Static (mean effects)	Dynamic (wave frequency effects)
Waves	Mean wave drift loads	First-order wave loads
Current	Mean current loads	-

Table 3: Force contributions to the Static and dynamic analysis

Figure 6 represents an overview of how wave loads contribute to a static offset due to mean drift forces and dynamic motion due to excitation and radiation loads. In addition, it shows how current can be treated as uniform through the water column contributing to the static offset of the system. Here, displacement in the x-direction, and motion in surge (η_1) is used as an example.

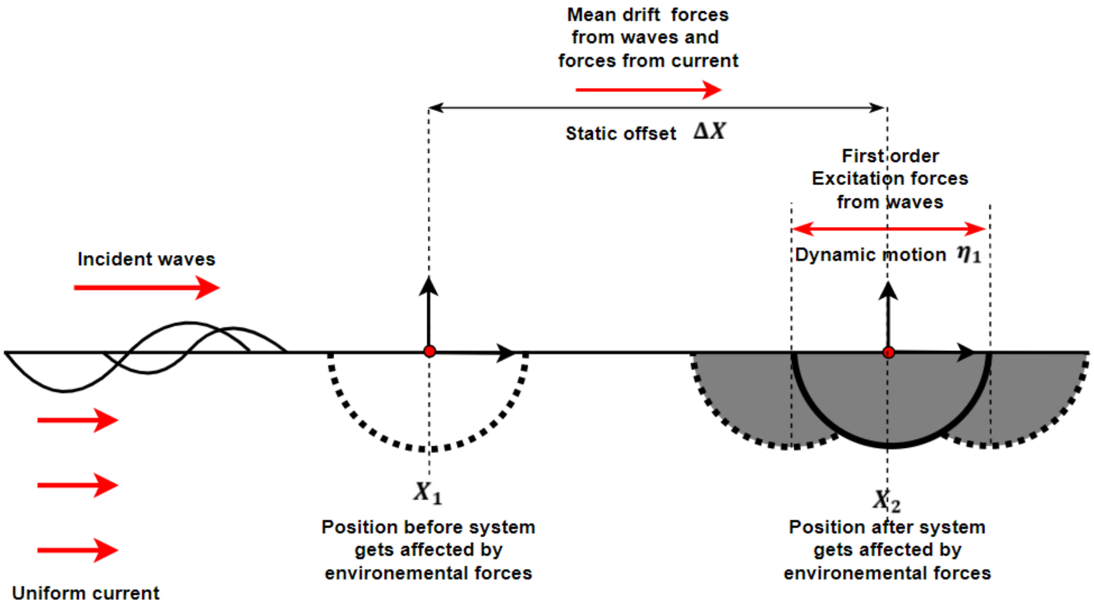

Figure 6: Wave and current forces contributing to static offset (ΔX) and dynamic motion (η_1)

From figure 6, and the limitation of the problem to the wave frequency regime including mean drift forces and forces from current, figure 7 shows the principle of a static and dynamic offset with the notation used throughout the analysis of the mooring system. The forces and offset in x-direction will be emphasized due to the significance of horizontal displacement when evaluating mooring system integrity.

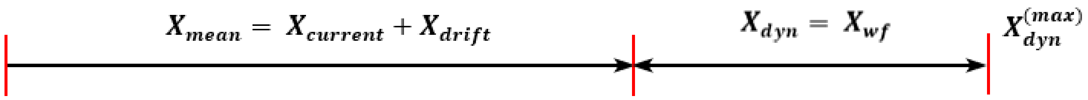

Figure 7: Contributions to the horizontal offset of the system when suspected to forces

Throughout the analysis, X_{dyn}^{max} will be denoted as X_{dyn} to simplify the notation. It is important to mention that the mooring system analysis conducted in section 5.3 is force driven, as the static force is found directly from the mean wave drift and current effects. This means that X_{dyn} is used to find the equivalent maximum dynamic force (F_{dyn}) by using the linear mooring line stiffness modeled in WAMIT. The dynamic force is then used in combination with the mean force when evaluating the top side tension of the mooring lines.

The numerical software WAMIT is used for the dynamic wave analysis, and to estimate the mean wave drift forces. The software is a radiation/diffraction panel program developed for the linear analysis of the interaction between plane progressive surface waves and various types of floating and submerged structures. It uses the fluid pressure on the body surface from the linearized Bernoulli equation to find different contributions to the wave-body interaction problem [25] (Chapter 1). In addition to accounting for external waves affecting the structure, WAMIT has the ability to account for free surface effects from the internal water mass affecting the dynamic motion of the system.

2.2.1 The linearized Bernoulli Equation

When working with wave-body interaction in a marine environment, the Bernoulli equation expressed in equation 7 is essential to be able to describe loads and motions. The equation is prone to the assumption of Potential flow and linear theory, closely connected to the first-order wave velocity potential (ϕ_1), further described in section 2.3.

$$P = -\rho g z - \rho \frac{\partial \phi_1}{\partial t} - \frac{1}{2}\rho \nabla \phi_1 \cdot \nabla \phi_1 \tag{7}$$

The equation describes the total pressure in the fluid domain. Here, the first term (equation 8) on the right-hand side is the hydrostatic pressure, which contributes to restoring forces ($C_{ij}\eta_j$). The second term (equation 9) is the linear dynamic pressure, used to find the excitation forces ($F_{i(exc)}$). Both the first and second linear term is highly important for the first-order wave loads in the dynamic analysis. The third term (equation 10) is the quadratic pressure, which can be used to find the second-order mean wave drift loads from direct pressure integration on the wetted surface, using linear potential theory [24] (Chapter 2).

The hydrostatic pressure term

$$P_{stat} = -\rho g z \tag{8}$$

The linearized dynamic pressure term

$$P_{dyn} = -\rho \frac{\partial \phi_1}{\partial t} \tag{9}$$

The quadratic pressure term

$$P_{quad} = -\frac{1}{2}\rho \nabla \phi_1 \cdot \nabla \phi_1 \tag{10}$$

2.3 Dynamic analysis

The dynamic analysis accounts for the first-order response from waves in the wave frequency domain using linear theory. This means that the system is assumed to oscillate with the same frequency as the incident regular waves as illustrated in figure 8. It also enables the analysis to be limited to the frequency domain, estimating RAO's when the system is suspected to different incident regular wave periods (ω_j) and amplitudes (ξ_{Aj}) [16].

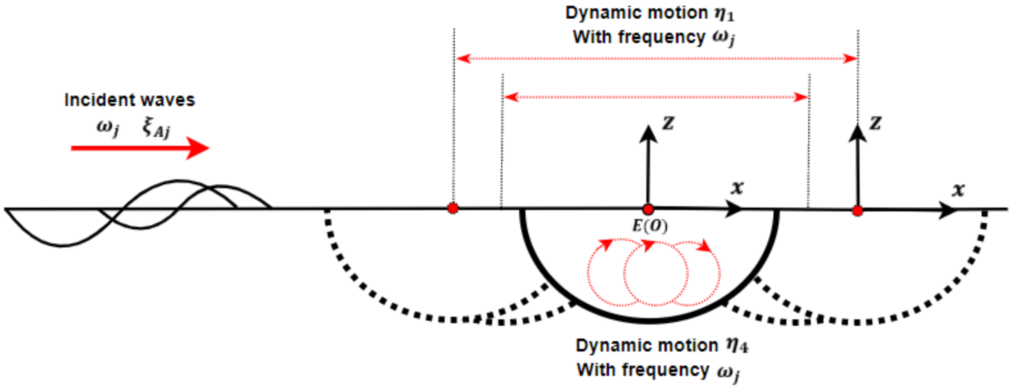

Figure 8: Structure oscillating with wave frequency ω_j in surge and pitch

In addition, the figure shows the definition of the body coordinate system with origin $E(O)$ located on the mean undisturbed free surface, defined in the center of the structure. This coordinate system is used throughout the thesis when defining the geometry. It is also used by WAMIT when defining motions and forces in the dynamic and static analysis. When analyzing the free surface effects, one additional coordinate system denoted as the free surface coordinate system with origin $B(O)$ is used. This system follows the free surface of the internal tank [25] (Chapter 5).

Under the assumption that the system oscillates with the same frequency as the incoming wave frequencies affecting the system, the general motion of the system for any DOF can be expressed as illustrated in equation 11.

$$\eta_j(t) = \eta_{jA} \sin(\omega_j t) \tag{11}$$

Here, $\eta_j\ (t)$ is the motion in j-direction and $\sin(\omega_j t)$ is the sinusoidal motion of the system. For simplicity, the random phase angle (ϵ) has been set to zero to simplify the term when presenting the theory.

The next subsection highlights assumptions and simplifications used in linear theory to derive equations and velocity potentials necessary to solve for the forces and motions of the system in the first-order wave-body interaction problem.

2.3.1 Linear wave theory and basic assumptions

First-order wave forces result in oscillating motions in the 6 DOF as illustrated in figure 8. Using linear theory, the wave-induced motions (η_j) and amplitudes (η_{jA}) are linearly proportional to the amplitude of the oscillating wave affecting the structure. In addition, the body is assumed to oscillate with the same frequency as the incoming waves.

The first-order forces connected to the body motions are calculated by studying the interaction between water particles and the structure in the wave-body interaction problem. This is done by evaluating the first-order wave Velocity potential, which can be used to derive expressions for the horizontal and vertical velocities, accelerations and dynamic pressure on the body surface [12] (Chapter 3).

Since it is possible to obtain results in irregular sea by superimposing results from regular waves, it is sufficient to analyze the structure in regular incident waves i.e the wave is of the sinusoidal type with parameters illustrated in figure 9. The figure also illustrates the boundaries that must be accounted for when deriving the first-order incident wave velocity potential used in linear wave theory to describe the motion of the incident regular waves.

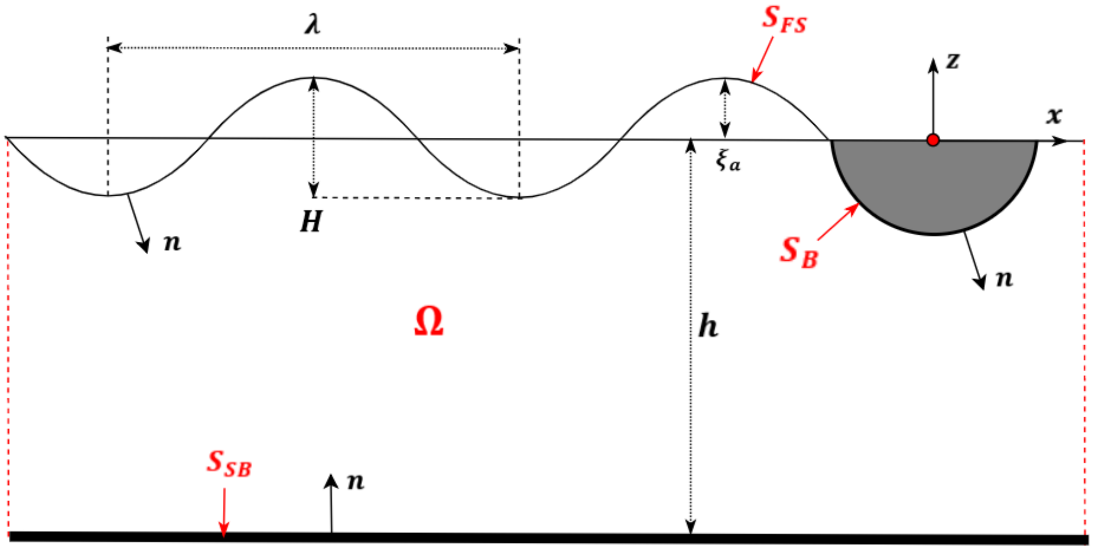

Figure 9: Wave parameters and boundary conditions used to find the velocity potential

To apply linear wave theory, the potential flow has to be assumed i.e the flow is incompressible ($\nabla \cdot \boldsymbol{V} = 0$), irrotational ($\nabla \times \boldsymbol{V} = 0$) and inviscid, which means that the water has constant density, zero local rotation and zero viscosity respectively. The consequences of assuming that the fluid is irrotational is that $\boldsymbol{V}$ can be written as the gradient (∇) of the velocity potential (ϕ) as expressed in equation 12 [16] (Chapter 2).

$$\boldsymbol{V} = \nabla\phi = \frac{\partial\phi}{\partial x}i + \frac{\partial\phi}{\partial y}j + \frac{\partial\phi}{\partial z}k \tag{12}$$

Further, as the water is assumed to be incompressible, the velocity potential has to satisfy the Laplace equation, expressed in equation 13.

$$\boldsymbol{\nabla}^2\phi = \frac{\partial^2\phi}{\partial x^2}i + \frac{\partial^2\phi}{\partial y^2}j + \frac{\partial^2\phi}{\partial z^2}k \tag{13}$$

The Boundary conditions for the sea bottom (S_{SB}), the free surface (S_{FS}) and the body surface (S_B) are listed in equation [14, 15, 16]. The impermeability condition means that the fluid is prohibited from piercing the boundaries.

Bottom surface impermeability condition on S_{SB}:

$$\frac{\partial\phi}{\partial n} = n \cdot \boldsymbol{\nabla}\phi = 0 \tag{14}$$

Free surface impermeability condition valid on z = 0, including the kinematic and dynamic solution on S_{SF}:

$$\frac{\partial^2\phi}{\partial t^2} + g\frac{\partial\phi}{\partial z} = 0 \tag{15}$$

Body surface impermeability condition on S_B. Here, V_B is the body velocity:

$$\frac{\partial\phi}{\partial n} = n \cdot \boldsymbol{V_B} \tag{16}$$

Solving the Laplace equation with respect to the boundary conditions in figure 9, the first-order velocity potential for incident deep water waves (ϕ_{01}) expressed in equation 17 can be found. The procedure is mathematically complex and is not included in this paper [12] (Chapter 2).

$$\phi_{01}(x,y,z,t) = \frac{g\xi_A}{\omega}e^{kz}\cos\left(\omega t - kx\cos\beta - ky\sin\beta\right) \tag{17}$$

Here, g is the acceleration of gravity, k is the wave number and β is the heading angle. For simplicity, the phase angle (ϵ) has been set to zero. The 0 subscript means that there are incident waves and the 1 subscript means that the velocity potential only contains first-order terms, neglecting terms of a higher order. Throughout this paper, ϕ_{01} will be denoted ϕ_0 [16] (Chapter 6).

The incident wave potential expressed in equation 17 is both time and space dependent. Under the assumption of linearity and steady-state conditions, the potential can be separated into two different components, representing the space and time variable respectively. This is expressed in equation 18.

$$\phi_0(x,y,z,t) = \Re[\underbrace{\varphi_0(x,y,z)}_{space}\underbrace{e^{i\omega t}}_{time}] \tag{18}$$

The complex notation allows the problem to be solved in the frequency domain neglecting the time dependence, using the complex velocity potential (φ_0) [16] (Chapter 2).

The velocity potential limited to the frequency domain, utilized by WAMIT for incident deep water waves can be written on the form expressed in equation 19.

$$\varphi_0(x,y,z) = i\frac{g\xi_A}{\omega}e^{Kz}e^{-iKx\cos\beta - iKy\sin\beta} \tag{19}$$

Here k is the wave number from the dispersion relation expressed in equation 20, relating the wave frequency to the wavelength [24] (Chapter 2).

$$\frac{\omega^2}{g} = k\tanh(kh) \tag{20}$$

For deep water waves, $\tanh kh$ = 1, which means that k simplifies to equation 21.

$$k = K = \frac{\omega^2}{g} \tag{21}$$

Before further theory regarding forces and motions in the wave-body interaction problem is presented, the next subsection will introduce the Equation of motion, which is used to equate the motions induced by first-order hydrodynamic radiation and diffraction loads on the body surface.

2.3.2 Equations of motion

Based on Newton's second law, the equation of motion can be used to describe the dynamic motion of an arbitrary point of a physical system. To do this, the equation has to be solved for the six degrees of freedom, listed in section 2.1. For a marine system suspected to waves, the equation has to be solved with respect to loads affecting the system as well as physical parameters of the system itself. By finding the forces and physical parameters, the equation can be solved with respect to the dynamic motion for the translational or angular motion of interest [12] (Chapter 3).

$$F_{i\ (exc)}\ (t) = \sum_{j=1}^{6}[(M_{ij} + A_{ij})\ \ddot{\eta}_j(t) + B_{ij(lin)}\ \dot{\eta}_j(t) + B_{ij(qd)}\ \dot{\eta}_j(t)\ |\dot{\eta}_j(t)| + C_{ij}\ \eta_j(t)] \tag{22}$$

Equation 22 expresses the EQM with the physical parameters evaluated in this paper. The notation represents hydrodynamic coefficients, motions and forces related to the system. $F_{i\ (exc)}$ is the excitation force in i-direction, M_{ij} is the mass matrix, A_{ij} is the frequency dependent added mass matrix, $B_{ij(l)}$ is the frequency dependent linear damping matrix, $B_{ij(qd)}$ is the quadratic damping matrix, and C_{ij} is the stiffness matrix in i-direction due to motion in j-direction. η_j, $\dot{\eta_j}$ and $\ddot{\eta_j}$ is the motion, velocity and acceleration in j-direction respectively. The coupling terms arise if the body is unsymmetrical about the body coordinate system planes, resulting in coefficients where $i \neq j$. This leads to multiple EQM's with multiple unknown dynamic motions, that has to be solved to find the motion of the system in any arbitrary direction.

Under the same assumptions as the velocity potential, the motion of the system $\eta_j(t)$ in equation 23 can be expressed in terms of the complex notation used for the velocity potential.

$$\eta_j(t) = \Re[\eta_{jA} e^{i\omega t}] \tag{23}$$

This yields the modified Equation of motion expressed in equation 24.

$$F_{i\ (exc)} = \sum_{j=1}^{6} [-\omega^2(M_{ij} + M_{ij}^{(e)} + A_{ij}) + i\omega(B_{ij} + B_{ij}^{(e)}) + (C_{ij} + C_{ij}^{(e)})]\eta_{jA} \tag{24}$$

The right-hand side represents the radiation forces, found by solving the radiation problem, while the left-hand side represents the excitation forces, found by solving the diffraction problem.

In Equation 24 it is important to mention that η_{jA} and $F_{i\ (exc)}$ represent complex quantities of the motion in j-direction and the excitation force in i-direction respectively, given by equation 25 and 26.

$$\eta_{jA} = |\eta_{jA}| e^{i\omega t} \tag{25}$$

$$F_{i\ (exc)} = |F_{i\ (exc)}| e^{i\omega t} \tag{26}$$

Here, $|\eta_{jA}|$ and $|F_{i\ (exc)}|$ is the complex amplitudes of the motion and the exciting force respectively [12] (Chapter 3).

The equation is solved in the frequency domain in WAMIT by dividing by the factor $e^{i\omega t}$, neglecting the time dependence. Solving for the real part, the complex amplitudes of the motions $|\eta_{jA}|$ can be found for any DOF and wave amplitude affecting the body. Solving for the imaginary part yields the relative phases of the motions. In the EQM expressed in equation 24, all terms are linearized. The $M^{(e)}$ term is included by the user to account for the mass and inertia of the system excluding the internal water mass which is accounted for by the WAMIT software. The $B^{(e)}$ term is included to account for damping effects from linear sources other than potential damping, and damping from viscous effects. To include the viscous effects, it is important to emphasize that the quadratic term in equation 22 has to be linearized before added to the $B^{(e)}$ matrix [25] (Chapter 4). This is more thoroughly discussed in section 2.3.6. The $C^{(e)}$ term is included to account for horizontal stiffness from mooring line effects. Throughout the paper, the $M^{(e)}$, $B^{(e)}$ and $C^{(e)}$ term will be referred to as the user specified mass, damping and stiffness matrix respectively [12] (Chapter 3).

In WAMIT, solving the EQM in the wave frequency regime yields RAO's, which is a nondimensional definition of the body motions, describing the motion of the body relative to the incoming wave amplitude expressed in equation 27.

$$RAO_i = \frac{\eta_{jA}}{\zeta_A} \tag{27}$$

The RAO's are used in combination with a wave spectrum to obtain results from the wave frequency analysis, which is further discussed in section 2.5.

The following subsection will discuss the radiation and diffraction velocity potential, used to estimate the different force contributions in the left and right-hand side of the EQM. The methods to establish the velocity potentials, used by WAMIT for the radiation and diffraction problem will be presented under the same assumptions as the incident wave velocity potential.

2.3.3 Velocity potential for the Radiation and Diffraction Problem

To find the radiation and diffraction velocity potentials (φ_R and φ_D), this section will explain the use of the Panel method also known as the boundary integral equation method (BIEM) utilized by WAMIT to numerically estimate wave forces on the body surface [24] (Chapter 1).

Under the same assumptions of linearity and steady-state conditions as the incident wave potential, the radiation and diffraction velocity potentials can be expressed with the complex notation in equation 28.

$$\phi_{R/D} = \Re[\varphi_{R/D}(z, y, z)e^{i\omega t}] \tag{28}$$

This allows the problems to be solved in the frequency domain, by the use of the complex potentials $\varphi_{R/D}\ (z, y, z)$. The governing equation for the diffraction and radiation potential is the Laplace equation (13) and on the free surface (S_{FS}) the free surface condition (equation 15) applies. To assure that the waves propagate away from the body a condition known as the radiation condition applies for the scattering (φ_S) and the unit amplitude radiation potentials (φ_j). It is also important to mention that the body boundary condition is different for the diffraction and radiation potential [16] (Chapter 3).

The unit amplitude radiation potentials in the j-th mode, connected to the radiation potential must satisfy the boundary condition expressed in equation 29 on the body surface (S_B).

$$\frac{\partial \varphi_j}{\partial n} = n_j \tag{29}$$

The diffraction velocity potential must satisfy the boundary condition expressed in equation 30 to assure impermeability on the body surface (S_B).

$$\frac{\partial(\varphi_0 + \varphi_S)}{\partial n} = \frac{\partial \varphi_D}{\partial n} = 0 \tag{30}$$

After defining the boundary conditions for the diffraction and radiation velocity potential, Green's Theorem is used to derive integral equations for the radiation and diffraction velocity potentials on the body boundary

(S_B), expressed in Equation [31, 33, 35]. The theorem transforms a large volume integral into a much easier to handle surface integral [25] (Chapter 12).

Integral Equation for the unit-amplitude radiation potentials in the j-th mode (φ_j) *and the total Radiation velocity potential* (φ_R):

$$2\pi\varphi_j(\boldsymbol{x}) + \iint_{S_b} \varphi_j(\boldsymbol{\xi})\, \frac{\partial G(\boldsymbol{\xi}\,;\boldsymbol{x})}{\partial n_\xi}\, d\boldsymbol{\xi} = \iint_{S_b} n_j G(\boldsymbol{\xi}\,;\boldsymbol{x})\, d\boldsymbol{\xi} \tag{31}$$

$$\varphi_R = i\omega \sum_{j=1}^{6} \eta_{jA}\varphi_j \tag{32}$$

Integral equation for the Diffraction Velocity potential (φ_D):

$$2\pi\varphi_D(\boldsymbol{x}) + \iint_{S_b} \varphi_D(\boldsymbol{\xi})\, \frac{\partial G(\boldsymbol{\xi}\,;\boldsymbol{x})}{\partial n_\xi}\, d\boldsymbol{\xi} = 4\pi\varphi_0(\boldsymbol{x}) \tag{33}$$

The diffraction potential can also be obtained by finding the scattering potential individually, using the same principle as for the radiation potential. In this case, the diffraction potential is expressed in terms of both the scattering and incident wave velocity potential, illustrated by equation [34, 35]. The origin of the scattering phenomenon is essential regarding the physical meaning of the diffraction problem and is further discussed in section 2.3.4 [25] (Chapter 12).

Integral equation for the Scattering velocity potential (φ_S) :

$$2\pi\varphi_S(\boldsymbol{x}) + \iint_{S_b} \varphi_S(\boldsymbol{x})\, \frac{\partial G(\boldsymbol{\xi}\,;\boldsymbol{x})}{\partial n_\xi}\, d\boldsymbol{\xi} = -\iint_{S_b} \frac{\partial \varphi_0(\xi)}{\partial n}\, G(\boldsymbol{\xi}\,;\boldsymbol{x})\, d\boldsymbol{\xi} \tag{34}$$

$$\varphi_D = \varphi_0 + \varphi_S \tag{35}$$

Here, n_j is the unit vector pointing out of the fluid domain on the body surface. For j = 1, 2, 3, $\boldsymbol{n} = (n_1, n_2, n_3)$ and for j = 4, 5, 6, $\boldsymbol{r} \times \boldsymbol{n} = (n_4, n_5, n_6)$. $\boldsymbol{r}$ is the position vector on the body surface relative to the body coordinate system. The η_ξ notation represents the unit vector relative to an individual point coordinate system defined in the point source ($\boldsymbol{\xi}$) itself.

It is important to mention that the 2π factor indicates that we obtain potentials on the body surface. If we are in the fluid domain outside the body boundary this factor has to be replaced by 4π, which means the integral equations obtain velocity potentials outside the body boundary [24] (Chapter 2).

In both integrals the green function, $G(\boldsymbol{\xi}\,;\boldsymbol{x})$, is of major importance. It physically represents the potential of an oscillating source that is creating outgoing waves, known as wave Source Potential. This is illustrated in figure 10, where point $\boldsymbol{x}$ is located at an arbitrary point on the body surface. The figure treats the oscillating body as the wave source potential, creating outgoing waves connected to the radiation and scattering velocity potential.

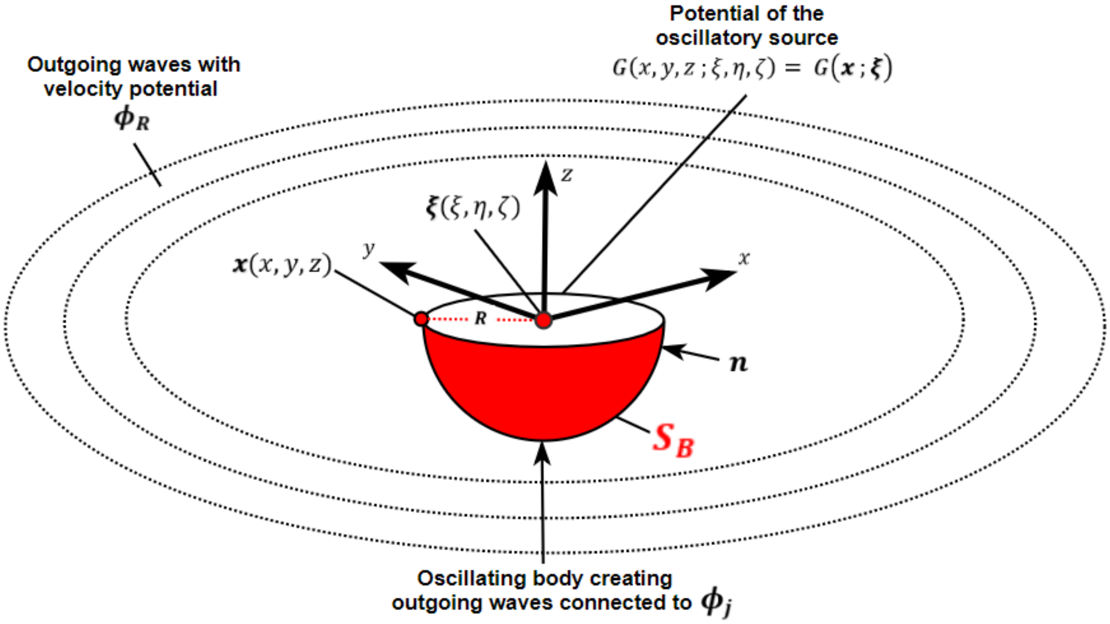

Figure 10: Illustrating the body acting as a Wave source creating outgoing waves

Mathematically, the Green function expressed in equation 36 is used to find the velocity potential at a point $\boldsymbol{x}$ due to a point source at location $\boldsymbol{\xi}$ in the fluid domain as illustrated in figure 10. The function applies for infinite water depth. The mathematical derivation of the function is beyond the scope of this thesis, but can be found in [32] by J.N.Newman.

$$G(\boldsymbol{\xi}\,;\boldsymbol{x}) = \frac{1}{r} + \frac{1}{r'} + \frac{2k}{\pi}\int_0^\infty dk\, \frac{e^{k(z+\zeta)}}{k-K}\, J_0(kR) \tag{36}$$

$$\boldsymbol{r} = [(x-\xi)^2 + (y-\eta)^2 + (z-\zeta)^2]^{\frac{1}{2}} \tag{37}$$

$$\boldsymbol{r'} = [(x-\xi)^2 + (y-\eta)^2 + (z-\zeta)^2]^{\frac{1}{2}} \tag{38}$$

Here, $R = (x-\xi, y-\eta)$ is the horizontal distance vector between $\boldsymbol{\xi}$ and $\boldsymbol{x}$, J_0 is the Bessel function of zero order and K is the wave number found from the dispersion relation, expressed in equation 21. the integral is solved using Fourier integration with respect to k. As for φ, the green function is subject to the free surface, bottom surface and radiation boundary condition [25] (Chapter 12).

The low order panel method and discretization of the integral equations

The panel method utilized in this thesis is the Low order panel method. In this method, the body is divided into N quadratic panels over the body surface. Each panel (k) contributing to the geometry of the body is represented by four vertices. Figure 11 illustrates how the coordinates of the vertices are defined in WAMIT.

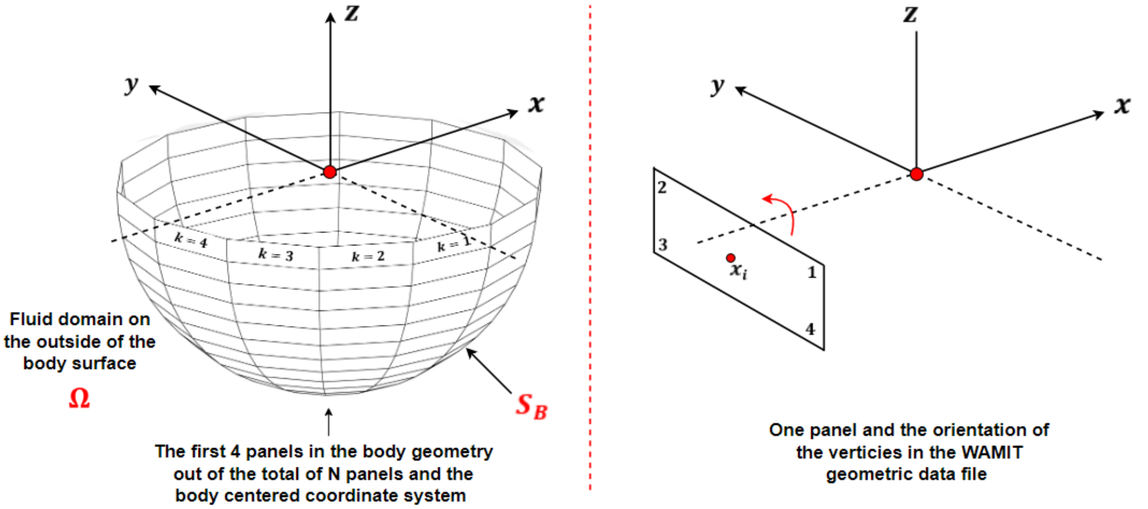

Figure 11: Method for defining the body geometry in the low order panel method

In figure 11, the fluid domain is on the outside of the body surface, and the orientation of the coordinates is counterclockwise. When accounting for the internal water mass, a similar geometric layout for the tank (S_T) has to be defined on the inside of the body surface. In this case, the fluid domain is on the inside of the structure, which means that the coordinate system is reversed, changing the orientation of the corner coordinates [25] (Chapter 5).

Using the low order panel method, the integral Equations for the diffraction and radiation potential in section 2.3.3 can be solved using a numerical approach, where $\boldsymbol{x}$ is equal to the center of each panel $(\boldsymbol{x_i})$ on S_B as illustrated in figure 11. To do this the velocity potential has to be assumed constant over the surface (S_k) of each panel. This results in N linearized equations both for the radiation and diffraction potential, allowing the total potentials to be written on the form expressed in equation 12 and 40. Here the integrals including the green functions are carried out over the surface of each panel.

The unit amplitude radiation potentials by low order panel method

$$2\pi\varphi_j(\boldsymbol{x_i}) + \sum_{k=1}^{N}\left[\iint_{S_k}\varphi_{j(k)}\frac{\partial G(\boldsymbol{\xi}\,;\boldsymbol{x_i})}{\partial n_\xi}\,d\boldsymbol{\xi}\right] = \sum_{k=1}^{N}\left[\iint_{S_k} n_{j(k)}G(\boldsymbol{\xi}\,;\boldsymbol{x_i})d\boldsymbol{\xi}\right] \tag{39}$$

Diffraction potential by low order panel method

$$2\pi\varphi_D(\boldsymbol{x_i}) + \sum_{k=1}^{N}\left[\iint_{S_k}\frac{\partial G(\boldsymbol{\xi}\,;\boldsymbol{x_i})}{\partial n_\xi}\,d\boldsymbol{\xi}\varphi_{D(k)}\right] = 4\pi\varphi_0(\boldsymbol{x_i}) \tag{40}$$

Here, S_k is the surface and $\varphi_{(k)}$ is the velocity potential over the k-th panel. i = 1,...,N is the index for the centroid of each respective panel. Two different solvers are included in the WAMIT software. One based on iteration and one based on solving the equations directly using standard Gauss elimination. The direct solver can be used when the iterative solver fails to converge, or to save computational time when the number of equations is relatively small [25] (Chapter 12).

2.3.4 Diffraction problem

In the diffraction problem, the body affected by the incident regular waves is restrained from moving, as illustrated in figure 12. The force arises due to the wave-body interaction and the unsteady fluid pressure along the body surface. The total excitation force can be divided into a Froude Kriloff and scattering contribution, also widely known as the diffraction contribution.

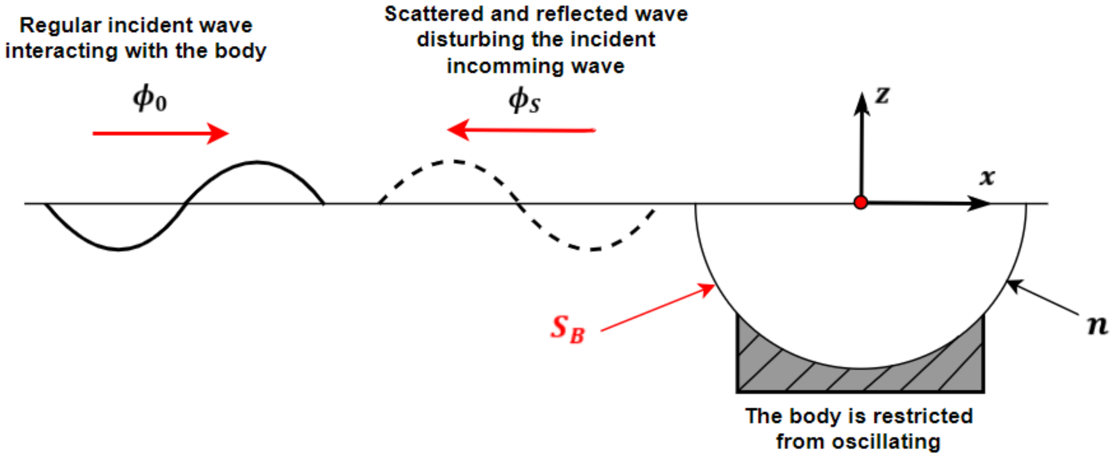

Figure 12: Illustrating the principle behind the diffraction problem

The Froude Kriloff load arises due to the hydrodynamic force induced on the body by the undisturbed incident wave, creating a corresponding undisturbed pressure field. This makes the Froude Kriloff load dependent on the incident regular wave velocity potential interacting with the body as if it was not there.

The scattering contribution to the excitation load appears due to the body interacting with, and disturbing the incoming incident wave to recover the body impermeability. As the wave interacts with the body it gets reflected off and bent around the structure, thus changing the pressure field around the body creating outgoing waves. This makes the scattering contribution tied to the outgoing wave velocity potential.

Using the numerical approach in section 2.3.3 the velocity potential connected to the diffraction problem can be found ($\phi_D = \phi_0 + \phi_S$). From this, the excitation load can be found by integrating the linear dynamic pressure from the incident and scattered wave along the wetted body surface as expressed in equation 41.

$$F_{i\,(exc)}\,(t) = -\rho \iint_{S_B} \left(\frac{\partial \phi_0}{\partial t} + \frac{\partial \phi_S}{\partial t} \right) n_i \, dS = \Re \left\{ \iint_{S_B} -\rho i \omega e^{i\omega t} (\varphi_0 + \varphi_S) n_i dS \right\} \tag{41}$$

Here, the same rules apply for the normal vector n_i as for the normal vector n_j defined in section 2.3.3. This means that the normal vector is pointing out of the fluid domain towards the surface of the body as illustrated in figure 12 [16] (Chapter 5).

Further, limiting the excitation load to the frequency domain, it is possible to find the complex amplitude of the excitation load from the expression in equation 42 [25] (Chapter 4).

$$|F_{i\,(exc)}| = -i\omega\rho \iint_{S_B} \varphi_D n_i \, dS \tag{42}$$

In the low order panel method used by WAMIT, the diffraction potential expressed in equation 40 is used to find the complex amplitude of the excitation load expressed in equation 42. This is done in a numerical approach similar to that of the velocity potential, evaluating the dynamic pressure over each respective panel (k), and summing the total contribution from the number of N panels [24] (Chapter 3).

2.3.5 Radiation problem

In the radiation problem the body is forced to oscillate with the same frequency as the incoming waves. This leads to outgoing radiated waves when the body interacts with the surrounding water mass connected to the radiation velocity potential. Even though the body is forced to oscillate in the wave frequency regime, the incoming waves are neglected. This limits the problem exclusively to the waves created by the oscillating body as illustrated in figure 13.

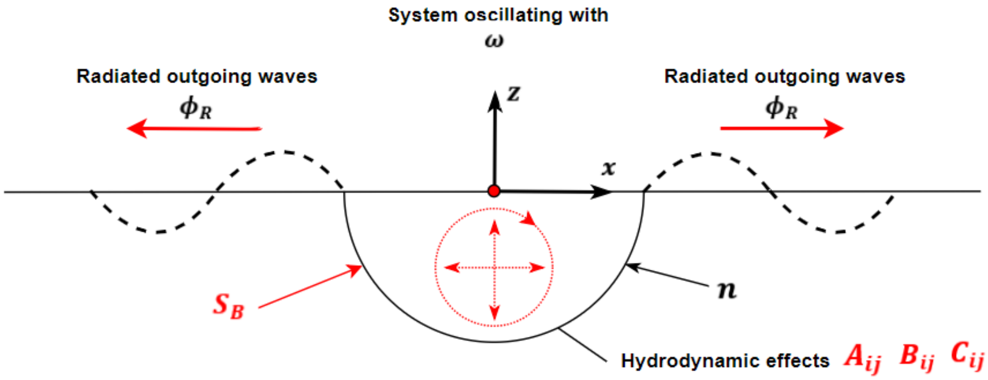

Figure 13: Illustrating the principle behind the Radiation problem

As the body moves in the 6 DOF it is subjected to hydrodynamic loads from the surrounding water mass. These loads are connected to three different physical phenomenons known as restoring (C_{ij}), damping (B_{ij}) and added mass (A_{ij}). They are represented in the equation of motion as three different terms connected to the motion (η_j), velocity ($\dot{\eta}_j$) and acceleration ($\ddot{\eta}_j$) of the oscillating system respectively. The total radiation potential is found from the summation of the unit amplitude radiation potentials from motion in the 6 DOF, as illustrated in equation 32. This makes it possible to find the radiation force by integrating the radiation dynamic pressure over the body surface, or from the summation of the added mass and damping contributions, expressed in equation 43 [16] (Chapter 3).

$$\begin{aligned} F_{i\,(rad)}(t) &= \iint_{S_B} \rho \frac{\partial \phi_R}{\partial t} n_i \, dS = \sum_{j=1}^{6} \{-A_{ij}\ddot{\eta}_j - B_{ij}\dot{\eta}_j\} \\ &= \Re\left\{ \iint_{S_B} -\rho i \omega e^{i\omega t} \left[\sum_{j=1}^{6} \eta_{jA}\varphi_j \right] n_i dS \right\} \end{aligned} \tag{43}$$

If the body is unsymmetrical we will have terms where $i \neq j$, e.g the pitch angular acceleration ($\ddot{\eta}_j$) can lead to an added mass coefficient in surge (A_{15}) and so on. Consequently, this gives a contribution to the radiation force in surge ($F_{1\,(rad)}$) from the pitch motion ($A_{15}\ddot{\eta}_5$). Limiting the radiation problem to the frequency domain, it is possible to obtain the complex amplitude of the radiation force as expressed in equation 44.

$$|F_{i\,(rad)}| = -i\omega\rho \iint_{S_B} \left[\sum_{j=1}^{6} \eta_{jA}\varphi_j\right] n_i dS \tag{44}$$

The added mass and potential damping coefficients can be estimated separately from equation [45,46], and used to solve the EQM expressed in equation 24. Here the added mass and damping are connected to the real and imaginary part of the integral respectively.

Added mass (A_{ij})

$$A_{ij} = \Re\left\{\rho \iint_{S_B} \varphi_j n_i \, dS\right\} \tag{45}$$

Potential Damping (B_{ij})

$$B_{ij} = \Im\left\{-\omega\rho \iint_{S_B} \varphi_j n_i \, dS\right\} \tag{46}$$

Due to the similarity of the right-hand side, and the fact that the added mass and damping can be is connected to the real and imaginary part of the integral respectively, equation 45 and 46 can be combined to equation 47.

$$A_{ij} - \frac{i}{\omega} B_{ij} = \rho \iint_{S_B} \varphi_j n_i \, dS \tag{47}$$

In WAMIT, The integral in equation 47 are carried out over the surface of each panel (S_k) using the velocity potentials in equation 39. This allows the total linear coefficients to be found by summation over the total number of N panels [25] (Chapter 4) [24] (Chapter 3). The output file in WAMIT displays the nondimensional quantity of the added mass and damping coefficient expressed in equation 48, where k = 3 for i, j = 1,2,3.

$$\overline{A}_{ij} = \frac{A_{ij}}{\rho L^k} \qquad \overline{B}_{ij} = \frac{B_{ij}}{\rho L^k \omega} \tag{48}$$

The hydrodynamic forces and coefficients arise due to different physical phenomenons. The added mass terms ($A_{ij} \cdot \ddot{\eta}$) arise due to the dynamic pressure effects from accelerated water around the body surface as it moves. The potential Damping terms ($B_{ij} \cdot \dot{\eta}$) is connected to the dynamic pressure and wave making, where energy is transferred from the body to the surroundings as the body oscillates. The hydrodynamic restoring terms ($C_{ij} \cdot \eta$) arise due to the hydrostatic pressure over the wetted surface and change in buoyancy when the body oscillates vertically [36]. Due to the sheer nature of the restoring terms, and their close connection to change in buoyancy, the hydrodynamic restoring in the horizontal plane is zero. Further, this means that hydrodynamic restoring is closely connected to vertical motion and that the hydrodynamic terms in equation 24 will be connected to heave, roll and pitch. This also means that to provide horizontal restoring, assuring that marine systems are able to stay stationary, restoring is introduced through the stiffness of mooring systems (K_{ij}) [12] (Chapter 8). In WAMIT, the contribution to the horizontal stiffness is added through the user specified stiffness matrix, which is further discussed in section 2.3.7. As the radiation problem only accounts for linear effects from potential damping, Viscous and other damping effects have to be accounted for in the user-specified damping matrix.

2.3.6 Viscous and critical damping

Every marine structure is prone to different damping effects when oscillating in the wave frequency regime interacting with the surrounding water mass. One of the most important effects which are not accounted for in potential theory is viscous effects [23]. This phenomenon can be divided into two different origins, which are associated with skin friction and pressure effects.

Skin friction effects are connected to friction between water particles and the submerged body surface. The pressure effects are associated with the so-called Eddy making, which occurs when the pressure field surrounding the body is different on either side. Both effects are relevant for viscous damping effects, but have highly different contributions dependent on the body geometry and roughness of the surface [31]. In the case of CFFC structures, the major contribution to the viscous damping is assumed to be due to eddy making effects, known as Eddy making damping. This is due to the smooth surface of the structure, where skin friction is minimal [12] (Chapter 3). The Eddy making damping is referred to as quadratic damping ($B_{ij\ (qd)}$) in the Equation of motion expressed in 22.

The eddies that form due to the difference in pressure on the front and back side of the structure, causes a drag force (F_D). This is illustrated in figure 14.

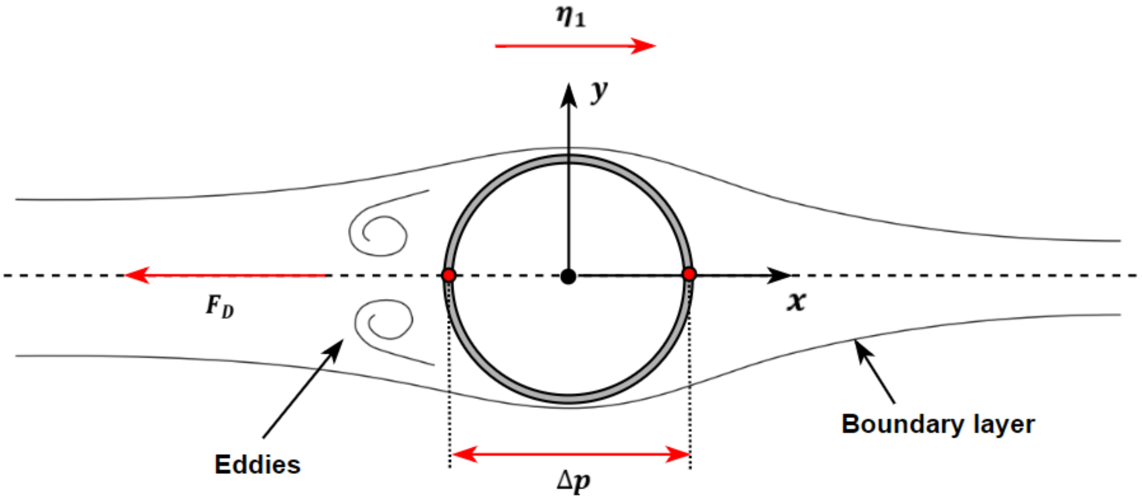

Figure 14: Flow past a circular circumference in the 2D xy-plane

In potential theory, the body is forced to oscillate with the same frequency as the incoming waves, which means that the flow around the structure is prone to constant change. Figure 15 illustrates how the formation of vortexes during oscillation in surge causes eddy making damping effects connected to the drag force.

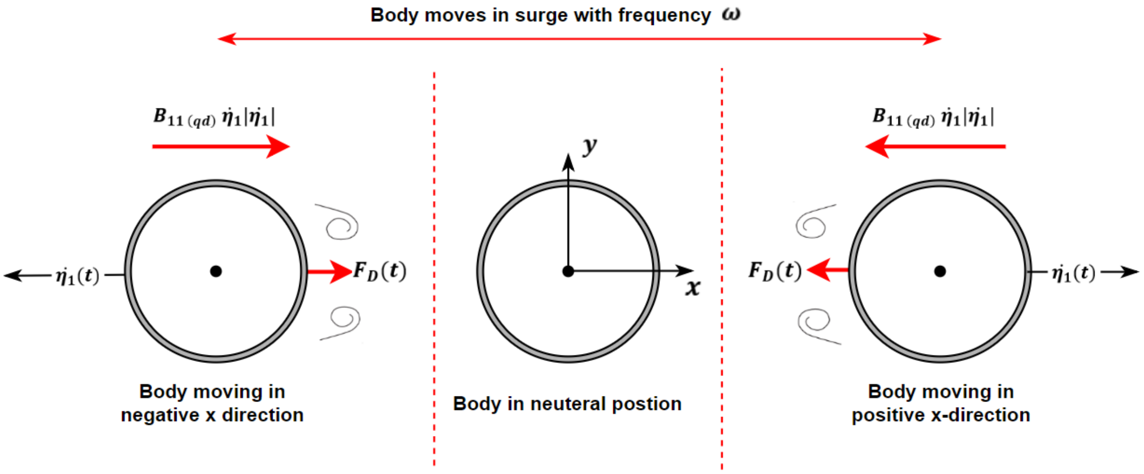

Figure 15: Eddy making viscous damping effects

An important parameter to classify the amount and pattern of eddy making around the structure in a non-steady state is the Keulegan Carpenter number defined in equation 49.

$$KC = \frac{\dot{\eta}_A T}{D} \tag{49}$$

Here, $\dot{\eta}_A$ is the amplitude of the velocity of the oscillating body, T is the period of oscillation and D is the diameter of the body.

For high frequency motion ($KC < 4$) the system is prone to constant change in direction. This can hinder vortexes to form, and the eddy making damping is close to zero. For lower frequency motion ($KC > 4$) eddies have time to develop before the flow around the structure changes direction [44].

As this paper investigates mooring system integrity, the horizontal motion in surge and sway is highly important. For horizontal motion, the potential damping is small compared to vertical motion. This is due to the close connection between potential damping and wave making, which amplifies the importance of damping from other than radiation effects such as viscous damping. In WAMIT this additional damping is modeled through the user-specified damping matrix, which means that any additional damping must be linearized before it is added to the EQM expressed in equation 24 [23].

The free decay test

By performing a free decay test, it is possible to estimate the damping by evaluating the logarithmic decrement as the body oscillates freely in calm water as illustrated in figure 16.

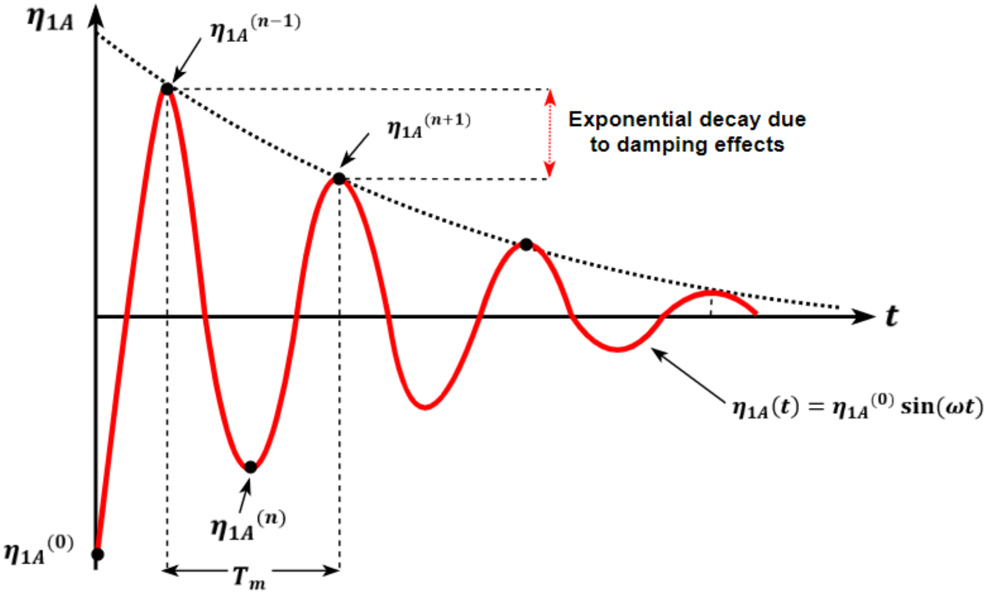

Figure 16: Decay test and the logarithmic decrement

The logarithmic decrement between two successive peaks in the decay test can be found from equation 50.

$$\delta = \ln\left(\frac{\eta_{1A}{}^{(n-1)}}{\eta_{1A}{}^{(n+1)}}\right) \tag{50}$$

Here, T_m is the mean period between each oscillation and $\eta_{1A}{}^{(0)}$ is the first amplitude when the decay test is initiated. Expressions for the amplitudes related to the time domain in figure 16 can be written on the form expressed by equation [51, 52].

$$\eta_{1A}{}^{(n-1)} = \eta_{1A}(t^{(n-1)}) \tag{51}$$

$$\eta_{1A}{}^{(n+1)} = \eta_{1A}(t^{(n-1)} + T_m) \tag{52}$$

By using the logarithmic decrement from the free decay test, the next section will describe a method adapted from [12] (Chapter 7) By O.M.Faltinsen, which can be used to estimate the linear and quadratic damping coefficient for a freely oscillating marine system. In the free decay test, there are no external forces acting on the body, which gives the EQM in surge expressed in equation 53.

$$\ddot{\eta}_1 + p_1\,\dot{\eta}_1 + p_2\,|\dot{\eta}_1|\,\dot{\eta}_1 + p_3\,\eta_1 = 0 \tag{53}$$

Here, p_1 and p_2 represent the linear and quadratic damping coefficient in the decay test respectively where $p_1 = B_{lin}/(M_{11} + A_{11})$ and $p_2 = B_{qd}/(M_{11} + A_{11})$, and the right-hand side is zero due to the undisturbed freely oscillating motion. p_3 is the stiffness affecting the horizontal motion of the system.

By assuming that the damping is constant throughout the decay test when in reality it changes as the amplitude og oscillation decays, it is possible to find the linear and quadratic damping coefficients from the relation expressed in equation 54.

$$\frac{2}{T_m}\log\left(\frac{{\eta_{1A}}^{(n-1)}}{{\eta_{1A}}^{(n+1)}}\right) = p_1 + \frac{16}{3}\frac{{\eta_{1A}}^{(n)}}{T_m}p_2 \tag{54}$$

Here it is important to note that there is $T_m/2$ oscillation period between ${\eta_{1A}}^{(n-1)}$ and ${\eta_{1A}}^{(n)}$ as illustrated in figure 16. p_1 and p_2 are found from plotting the left-hand side of equation 54 against the right-hand side as illustrated in figure 17, fitting the points to a straight line using the least square method.

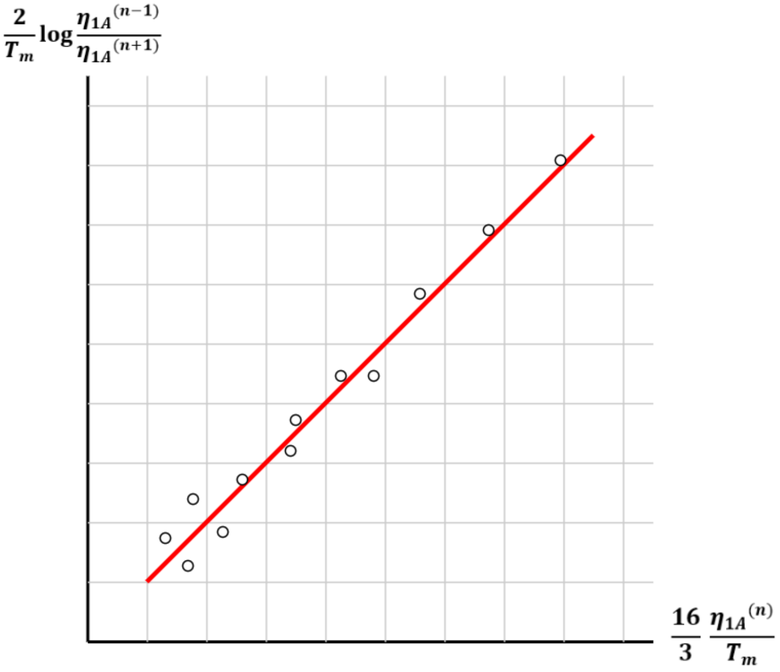

Figure 17: The least square method

As discussed previously, if the velocity of the oscillation changes drastically during the tests, both the KC number and the Reynolds number will change significantly, which leads to a highly changing flow pattern around the structure. This makes it impossible to find a linear and quadratic damping coefficient that can be assumed constant over the entire decay period [12] (Chapter 7).

Linear and linearized damping

When implementing the linear damping found from the decay test, it is important to remember that potential damping in surge (B_{11}) is already accounted for in the numerical calculations by the WAMIT software. The total linear damping can be estimated from the decay test using the p_1 damping coefficient expressed in equation 55.

$$B_{11\,lin} = p_1 \cdot (M_{11} + A_{11}) \tag{55}$$

From equation 55 and the potential damping estimated by WAMIT, the first contribution (${B_{11}}^{(1)}$) to the user specified damping matrix in WAMIT, which accounts for linear effects outside potential damping can be found from equation 56.

$${B_{11}}^{(1)} = B_{11\,lin} - B_{11} \tag{56}$$

Before adding the quadratic damping to the damping matrix, the term needs to be linearized. The general form of the linear and quadratic damping force is expressed in equation 57 and 58 respectively.

$$F_{lin}(t) = -B_{lin}\,\dot{\eta}(t) \tag{57}$$

$$F_{qd}(t) = -B_{qd}\,\dot{\eta}(t)\,|\dot{\eta}(t)| \tag{58}$$

By assuming that the quadratic damping force does the same amount of work, $P(t) = F(t) \cdot \dot{\eta}(t)$, during one oscillation as the linear damping force, $P_{lin}(t) = P_{qd}(t)$, we get the following energy relation between the linear and quadratic damping force, expressed in equation 59.

$$\int_0^{T_m} F_{lin}(t) \cdot \dot{\eta}(t) dt = \int_0^{T_m} F_{qd}(t) \cdot \dot{\eta}(t) dt \tag{59}$$

By assuming that the motion of the system can be expressed by the harmonic sinusoidal excitation expressed in equation 11, the velocity can be written as the derivative of the motion expressed in equation 60.

$$\dot{\eta}(t) = \omega\,\eta_A \cos{(\omega t)} \tag{60}$$

Inserting the velocity into the right and left-hand side of Equation 59, we get the integral expressed in equation 61.

$${\eta_A}^2\,\omega^2 \int_0^{T_m} B_{lin} \cos^2{(\omega t)} dt \; = \; {\eta_A}^3\,\omega^3 \int_0^{T_m} B_{qd} \cos^3{(\omega t)} dt \tag{61}$$

Solving the integral gives the following ratio between the linear and quadratic damping coefficient expressed in equation 62.

$$\frac{B_{lin}}{B_{qd}} = \frac{8}{3\pi}\omega\eta_A \tag{62}$$

Inserting the ratio between the linear and quadratic damping coefficient, we obtain the linearized quadratic damping force in expressed in equation 63.

$$F_{qd}{}^{(l)}(t) = -\frac{8}{3\pi}\omega\eta_A B_{qd}\,\dot{\eta}(t) \tag{63}$$

From the linearized damping force, the linearized damping coefficient can easily be found. This is expressed in equation 64.

$$B_{11}{}^{(2)} = \frac{8}{3\pi}\omega\,\eta_{1A}\,B_{11\,qd} \tag{64}$$

As for the total linear damping coefficient, the quadratic damping coefficient can be expressed in terms of the system mass and the p_2 coefficient from the decay test in equation 65.

$$B_{11\,qd} = p_2 \cdot (M_{11} + A_{11}) \tag{65}$$

Equation 66 relates the decay test including the p_2 coefficient found from the least square method to the linearized quadratic damping coefficient. Here, ω_m is the mean frequency of oscillation which is close to the eigenfrequency ω_n of the structure [33] (Chapter 6).

$$B_{(11)}{}^{(2)} = \frac{8}{3\pi}\omega_m\,\eta_{1A}{}^{(n)}\;p_2 \cdot (M_{11} + A_{11}) \tag{66}$$

It is important to emphasize that the linearized quadratic damping term ($B_{(11)}{}^{(2)}$) is dependent on the amplitude of oscillation and frequency dependent mass, which means that it changes as the body oscillate in the 6 DOF. This means that the linearized quadratic damping contribution to the damping matrix in WAMIT changes as the body oscillates with different frequency and amplitude [20].

By summation of equation 56 and 64 accounting for linear damping outside the radiation problem and linearized quadratic damping from viscous effects respectively, the total linearized damping coefficient can be found from equation 67.

$$B_{(11)}{}^{(e)} = B_{(11)}{}^{(1)} + B_{(11)}{}^{(2)} \tag{67}$$

Critical damping

To assure that the user specified damping matrix in WAMIT represents a realistic value for the damping provided by linear effects outside potential theory and viscous effects, the critical damping can be used to asses the percentage of damping in the system. Further, it can be used when modeling the user-specified damping matrix by using a percentage of critical damping when accounting for other than potential effects. The critical damping in surge of an oscillating system is expressed in equation 68.

$$B_{11}{}^{(cr)} = 2\sqrt{K_{11}(M_{11} + A_{11})} \tag{68}$$

Here, it is important to emphasize that the added mass varies with the oscillating frequency of the system. The damping ratio makes it is possible to evaluate the amount of damping in the system. The ratio is defined as the actual damping (B) relative to the critical damping ($B^{(cr)}$), and to the logarithmic decrement as expressed in equation 69.

$$\zeta = \frac{B}{B^{(cr)}} = \frac{\delta}{\sqrt{4\pi^2 + \delta^2}} \tag{69}$$

This ratio tells if the system is undamped ($\zeta = 0$), underdamped ($\zeta < 1$), critically damped ($\zeta = 1$) or overdamped ($\zeta > 1$).

2.3.7 Horizontal stiffness

The horizontal stiffness of nearly all marine structures is primarily provided by the mooring system and is crucial for the station keeping ability. In the equation of motion expressed in equation 22, the mooring line stiffness grants horizontal restoring to the system (F_R), making sure that the system is unable to move unhindered when the facility is affected by environmental forces. It also assures that the system returns to its pre-tensioned state when external forces seize to affect the system. The system reaches an equilibrium position when ($F_R = T_H$) where the horizontal top side tension (T_H) is dependent on the horizontal offset and the stiffness (K) of the system as expressed in equation 70.

$$T_H = K \cdot X \tag{70}$$

The system stiffness is influenced by different parameters where the main deciding factor is the design material and the geometry of the system layout. In the aquaculture industry, mooring lines composed of chains and polyester ropes are combined to provide the necessary strength and integrity to the system as a whole. The combined solution provides stiffness through two different principles known as elastic (k_e) and geometric stiffness (k_g). Figure 18 shows an overall sketch of a single mooring line component containing different stiffness characteristics [6].

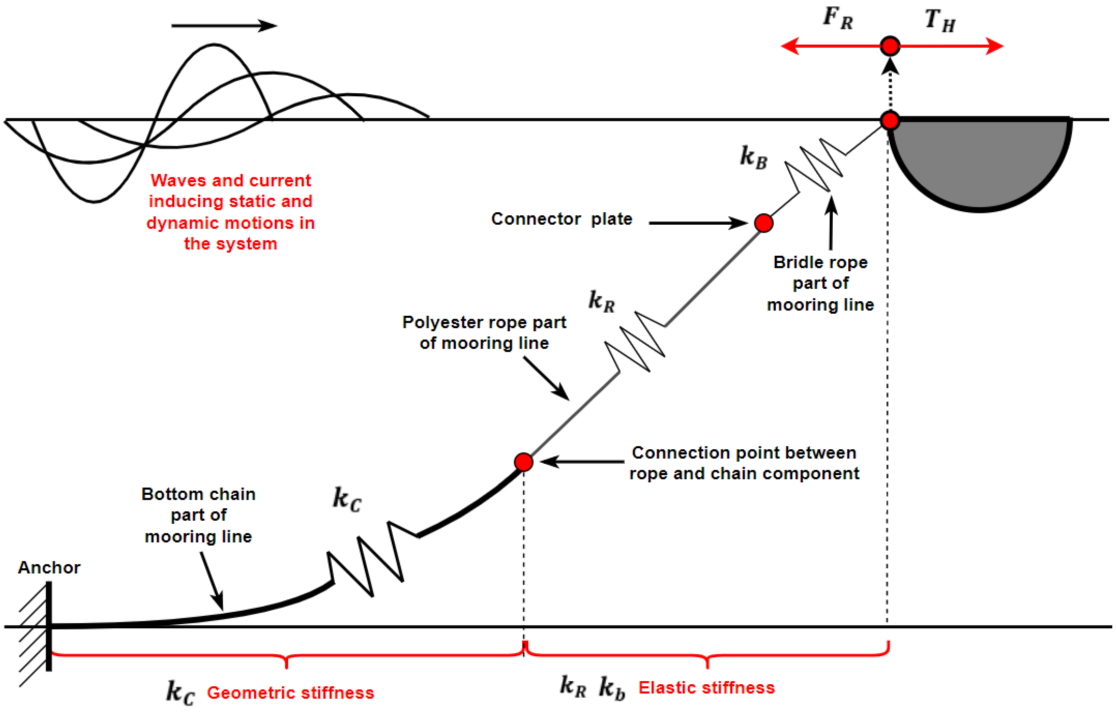

Figure 18: Several components of the mooring line providing stiffness to the system

The quote by quote chain and polyester rope part of the mooring system acts as springs when the system gets affected by external forces and can be modeled as individual members in a series when estimating the total stiffness of the system as expressed in equation 71 .

$$\frac{1}{k_{tot}} = \frac{1}{k_e} + \frac{1}{k_g} \tag{71}$$

In the case of the mooring system illustrated in figure 18, consisting of one bottom chain, a polyester rope stretching through the water column, as well as the bridles connecting the mooring line to the top side of the structure, the total stiffness can be found by adding each respective component as expressed in equation 72 [23].

$$\frac{1}{k_M} = \frac{1}{k_C} + \frac{1}{k_R} + \frac{1}{k_B} \tag{72}$$

Elastic stiffness

Elastic stiffness is closely connected to the material properties and its ability to elongate. Mooring line components containing elastic stiffness creates restoring force through its ability to stretch, working as a spring when pulled out of their equilibrium position, e.g the rubber band effect. This means that the rope components of the mooring system contribute to restoring force through elastic stiffness and elongation (dL) as illustrated in figure 19, where the system stops in a new equilibrium position ($X_1 + \Delta X$) when suspected to environmental forces. When the environmental forces seize, the system will be restored back to its earlier tension (T_{H1}) and the mooring line will return to its normal length (L). This gives a linear correlation between the restoring force and the horizontal displacement of the system (ΔX) [33] (Chapter 5).

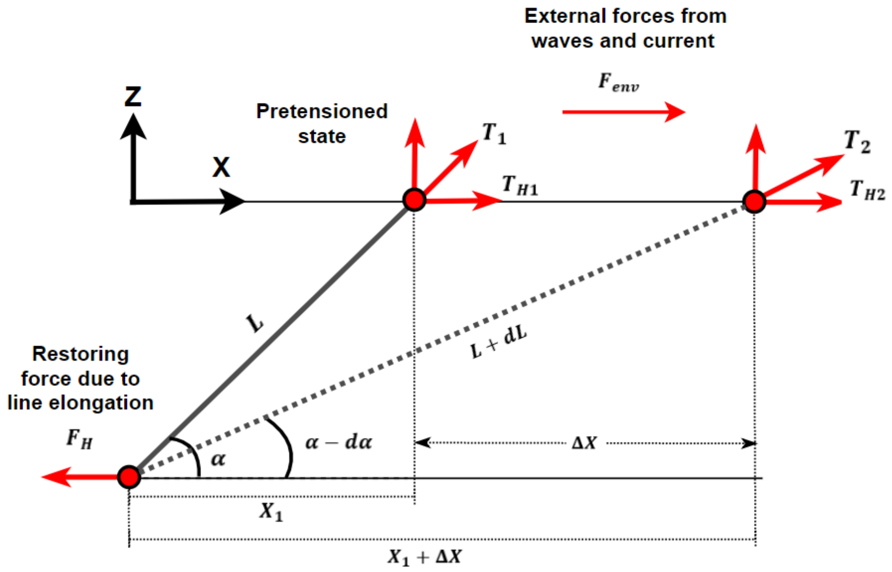

Figure 19: Elastic stiffness through elongation of the mooring line (dL)

Further, As the stiffness coefficient of polyester ropes commonly used in the aquaculture industry is heavily dominated by elastic stiffness, having little to zero geometric stiffness, it can be found from the correlation between length, E-modulus and cross section area of the rope diameter, expressed in equation 73 [6].

$$k_e = \frac{EA}{L} \tag{73}$$

Figure 20 illustrates the geometrical relation between the in-line elongation (dL) and the horizontal offset (dX), and equation 74 through 76 is the derivation of the horizontal stiffness in surge direction.

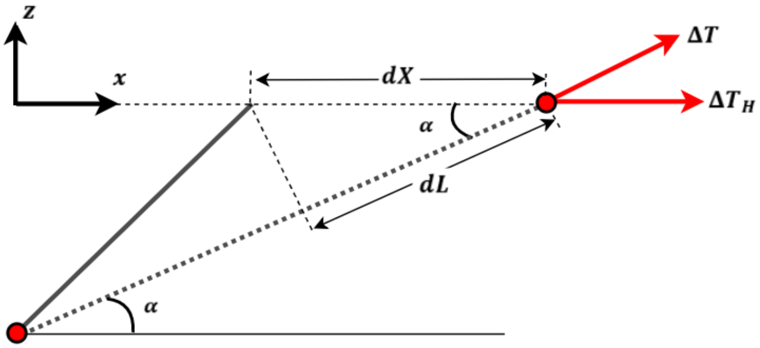

Figure 20: Geometrical relation between (dL) and (dX)

$$dL = \cos\alpha \cdot dX \tag{74}$$

$$\Delta T = \frac{EA}{L} \cdot dL \tag{75}$$

$$\Delta T_H = \frac{EA}{L} \cdot \cos\alpha^2 dX \tag{76}$$

Here it is important to note that the angle in the xy-plane (θ) between the mooring line and the horizontal axis (x) is assumed to be zero, and that the angle between the sea bottom and the mooring line is assumed to be constant ($d\alpha = 0$). Under these assumptions, the horizontal stiffness in surge direction ($k_{11\ elastic}$) can be expressed as seen in equation 77.

$$k_{(11)\ e} = \frac{\Delta T_H}{dX} = \frac{EA}{L} \cdot \cos\alpha^2 \tag{77}$$

On the other hand, if the angle in the xy-plane (θ) between the mooring line and the horizontal axis is nonzero as illustrated in figure 21, the geometric principle for the elongation illustrated in figure 20 applies in both planes [23].

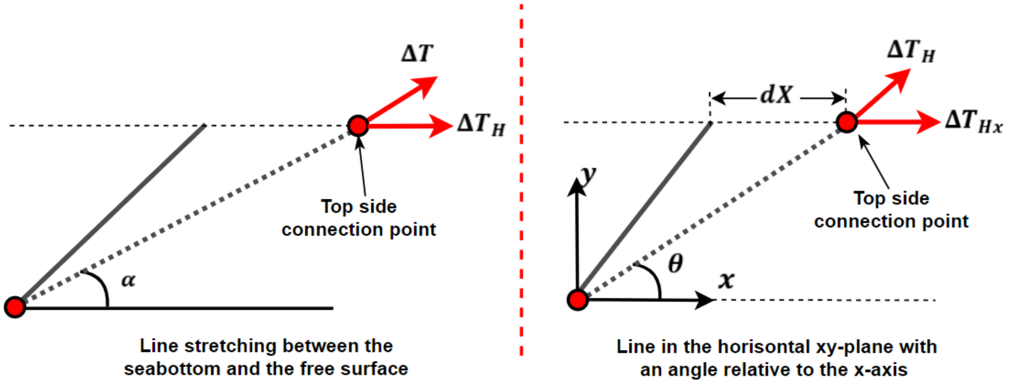

Figure 21: Geometrical relation between the horizontal xy-plane and vertical xz-plane

This means that the elastic stiffness in surge direction depends on both the elongation in the vertical (xz-plane) and the horizontal (xy-plane), which gives the expanded expression for the elastic stiffness in surge direction in equation 78.

$$k_{(11)\ e} = \frac{T_{Hx}}{dX} = \frac{EA}{L} \cdot \cos\alpha^2 \cos\theta^2 \tag{78}$$

Geometric stiffness

Geometric stiffness is highly dependent on weight, line length and pretension of the system. Mooring system components governed by geometric stiffness provide restoring through a change in catenary shape when the system moves. This makes chains or steel wires heavily dominated by geometric stiffness. In a pretensioned equilibrium, position normally a large part of the mooring line lays passive on the seabed. When the system gets affected by environmental forces, it shifts horizontally, which leads to a larger portion of the mooring line getting lifted off the seabed, making it active in the water column. This has two effects i.e the total tension in the mooring line and top side force increases ($T_{H1} < T_{H2}$), as well as an increase in horizontal moment arm (a). This leads to a restoring force, making the system inherit a new equilibrium position when the weight of the line creates a large enough force to match the environmental forces affecting the system.

When the external force seizes, the restoring will assure that the system returns to the earlier tension state (T_1). The effect of geometric stiffness is illustrated in figure 22, where the system shifts horizontally due to environmental forces affecting the system. It also illustrates that the restoring force (F_R) occurs due to the increased weight of the line hanging freely in the water column provided by geometric stiffness through the change in catenary shape [6].

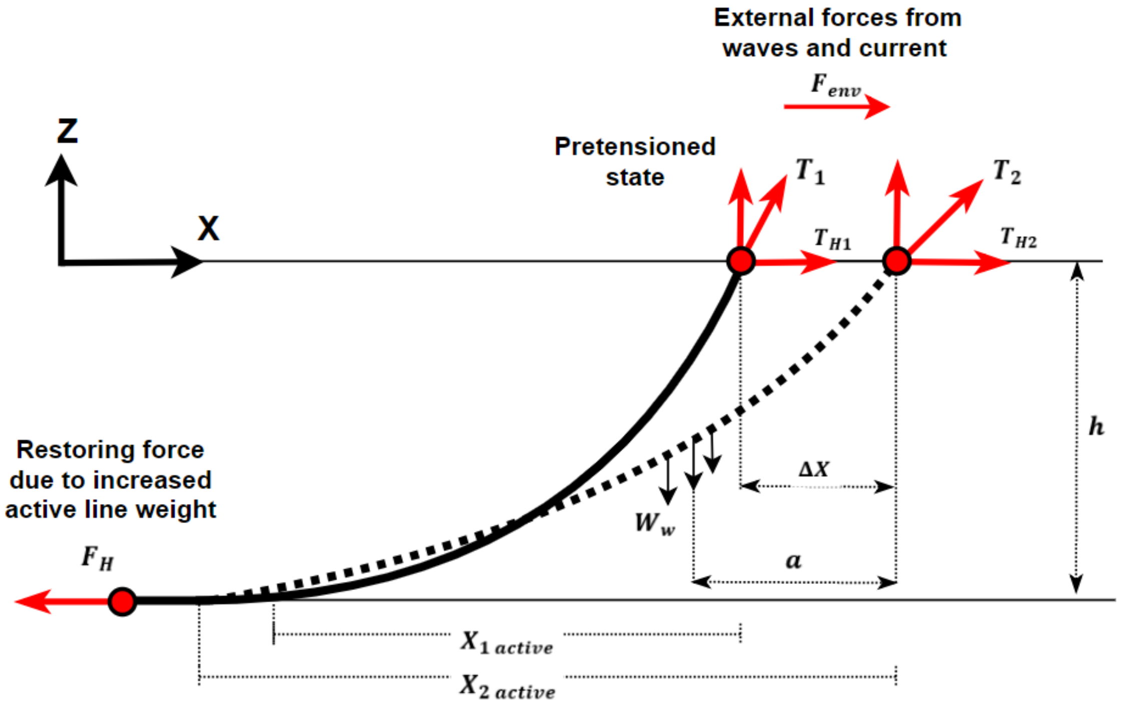

Figure 22: Geometric stiffness due to increased active line length when the system shifts horizontally (ΔX)

Steel is also suspect to some degree of elasticity, but for moderate water depth this effect can be neglected, due to minimal elongation. Both the weight and the moment arm increase as the horizontal offset increase, leading to a nonlinear correlation between the restoring force and the horizontal offset [12] (Chapter 8).

In order to find the stiffness of a catenary system, such as the chain part of a mooring line, the line characteristic has to be identified. To do this, the catenary equations can be used, which uses the relation between the horizontal offset (X) and the top side tension (T) in the mooring line.

The catenary equations can be found from analyzing a single element of the mooring line hanging active in the water column as illustrated in figure 23. Here D and F are mean hydrodynamic forces per unit length affecting the mooring line in the normal and tangential direction respectively. W_w is the weight of the mooring line in water per unit length, A is the cross-sectional area of the line itself, E is the modulus of elasticity, T is the tension at the top side connection point and ds is the length of the single line element. $-\rho g A z$ and $-\rho g A z - \rho g A$ are correction forces due to W_w representing the weight of of the line in water, inducing hydrostatic forces on the element.

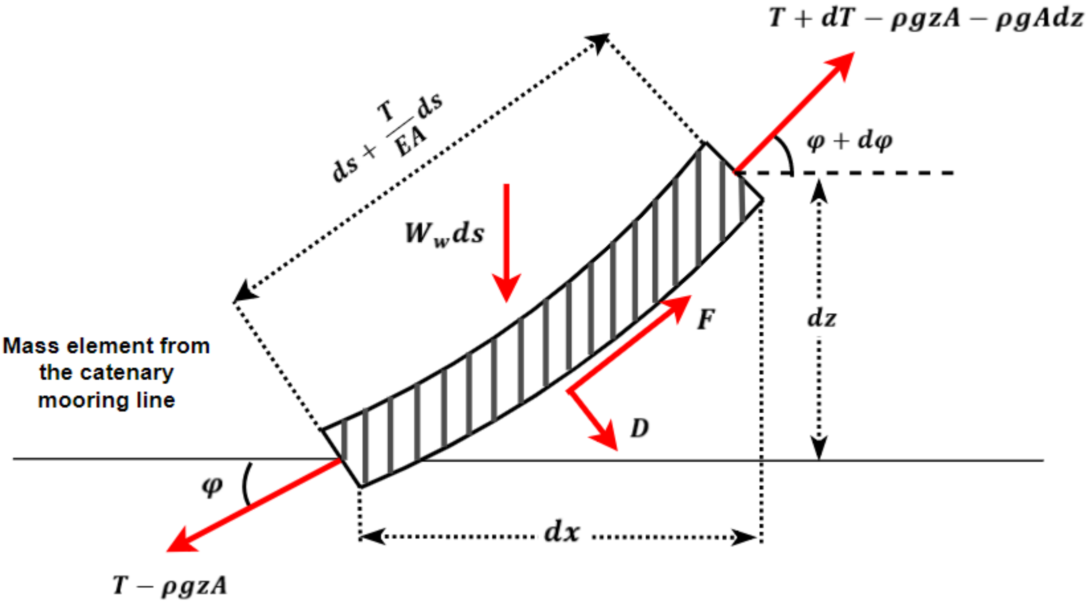

Figure 23: Single catenary mooring line element

From figure 23 the catenary equations 79 and 80 including effects from hydrodynamic, hydrostatic and elasticity can be found.

$$dT - \rho gAdz = [W_w \sin\varphi - F(1 + T/(AE))]ds \tag{79}$$

$$Td\phi - \rho gAzd\phi = [W_w \cos\varphi + D(1 + T/(AE))]ds \tag{80}$$

However, these equations are highly nonlinear and it is practically not possible to find an explicit solution. This means that the problem needs to be simplified, and in many cases it is a good approximation to neglect the effect from current forces (F and D). For typical elements dominated by geometric stiffness such as steel chains and wires the Elastic modulus is extremely high ($T/EA << 1$), which means that the elasticity also can be neglected [12] (Chapter 8).

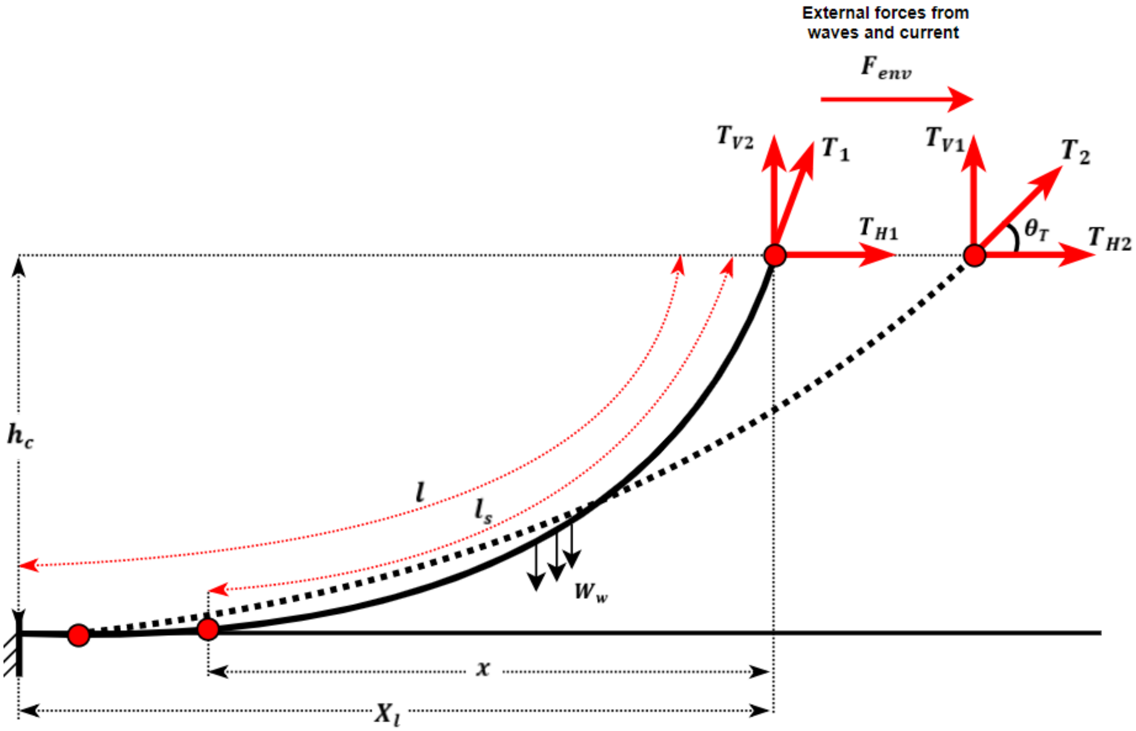

Figure 24: Catenary mooring line parameters and notation

Manipulating equation 79 and 80 and using the notation and mooring line parameters illustrated in figure 24, the simplified catenary equation describing the relation between the horizontal offset (X_l) and the horizontal tension in the mooring line can be written on the form expressed in equation 81. Here, l_s also is the active line length, l is the total line length, x is the horizontal active line length and X_l is the horizontal distance from the anchor to the top side connection point. The full derivation of the catenary equations can be found in [12] (Chapter 8) by O.M.Faltinsen.

$$X_l = l + \frac{T_H}{W_w} \cdot \cos^{-1}(1 + \frac{W_w \cdot h_c}{T_H}) - \sqrt{h_c \cdot (h_c + \frac{2 \cdot T_H}{W_w})} \tag{81}$$

In addition to the correlation between the horizontal displacement and the horizontal tension, equation 82 and 83 can be used to find the active line length (l_s) and the vertical line tension (T_v).

$$l_s = \sqrt{h^2 + 2h\frac{T_H}{W_w}} \tag{82}$$

$$T_V = T_H + l_s W_w \tag{83}$$

When the horizontal and vertical component of the mooring line tension is known, the angle between the in-line tension and the horizontal plane θ_T can be found from expression 84.

$$\theta_T = \tan^{-1}\left(\frac{T_V}{T_H}\right) \tag{84}$$

Using equation 81 the line characteristic can be established, and the geometric stiffness of the chain can be found. As the line characteristics for a catenary chain is nonlinear, the stiffness will vary based on the horizontal distance between the anchor and the attachment point at the top side of the structure. As most mooring systems are designed to assure that the supporting structure is unable to experience large horizontal motions, it is reasonable to use the lower end of the line characteristic to find the stiffness, which means close to the pretensioned state of the system. If the characteristic is highly nonlinear, the stiffness may be evaluated in a higher tension state [36].

Figure 25 shows the shape of a typical line characteristic, and the stiffness as the gradient of the slope around the pretensioned state for a catenary mooring line. It also shows how the top side tension gets affected by environmental forces and horizontal displacement.

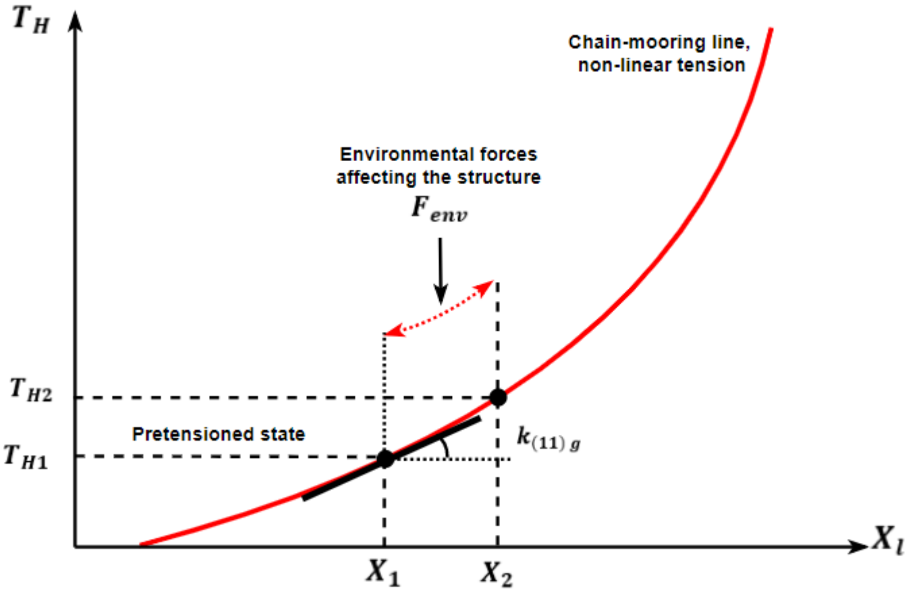

Figure 25: Line characteristic for one single mooring line showing the stiffness as the gradient around the pretensioned state of the system

As the stiffness in surge direction can be estimated by taking the derivative of T_H with respect to X, it is possible to find a general expression for the stiffness coefficient by manipulating equation 81. The expression for the geometric stiffness in surge for one single mooring line is expressed in equation 85 taken from [12] By O.M.Faltinsen.

$$k_{(11)\ g} = \frac{dT_H}{dX} = W_w \left[\frac{-2}{\sqrt{1+2(a/h_c)}} + \cos^{-1}(1+\frac{h_c}{a}) \right]^{-1} \tag{85}$$

In this expression, $a = T_{(H)mean} \ / \ W_w$, where $T_{(H)mean}$ is the average horizontal force on the anchor line, which in this example is the pretension of the system. The weight of the steel chain when submerged in seawater which can be found from equation 86.

$$W_w = W_A \left(\frac{\rho_{steel} - \rho_{sea}}{\rho_{steel}} \right) \tag{86}$$

Here, ρ_{sea} is the density of seawater, ρ_{steel} is the density of the steel chain and W_A is the weight of the steel chain in air.

Restoring force and mooring system stiffness

After calculating the total stiffness (k_M) for a single mooring line component, combining the principles of geometric and elastic stiffness in section 2.3.7, the total stiffness and restoring force of the mooring system can be estimated. Figure 26 shows the notation and definitions of the system consisting of several mooring lines in the transverse and longitude directions. here ψ_i is the angle between the body coordinate system x-axis, and each respective mooring line with orientation as illustrated in the figure. β is the heading angle of incoming waves. x_i and y_i is the distance from the center of the body to each respective mooring line attachment point. i is the number of mooring lines counted counterclockwise.

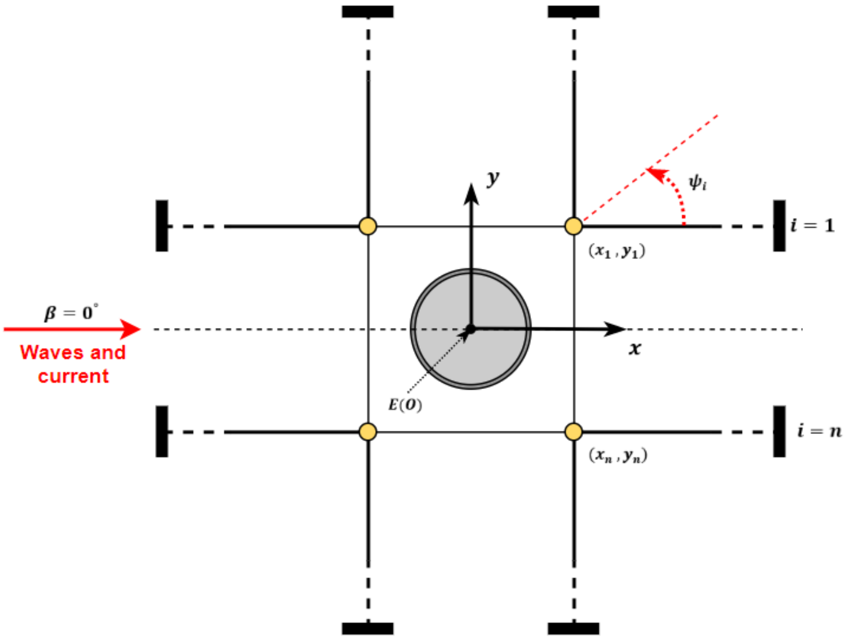

Figure 26: Notation used when defining angle between mooring lines and the body coordinate system $E(0)$

As the heading changes, so do the contribution from the different lines to the combined horizontal stiffness of the system. Figure 27 illustrates how the heading affects the system, leading to a contribution from every mooring line in the mooring system to the directional horizontal stiffness in surge and sway.

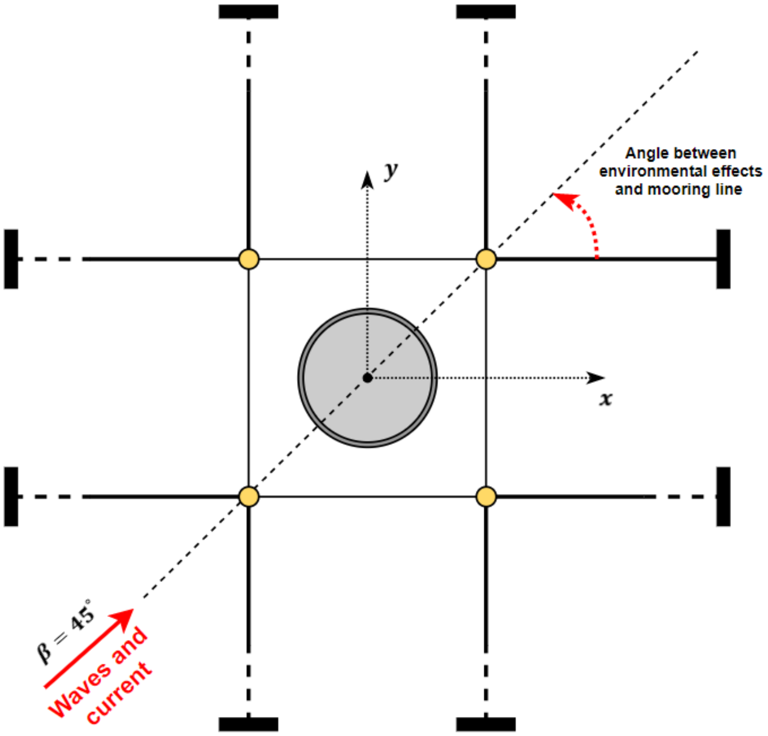

Figure 27: Illustration of how the horizontal stiffness gets affected by the heading angle β

Figure 27 has the sole purpose of highlighting the importance of how the stiffness in surge and sway changes when the heading of incoming environmental conditions changes relative to the body coordinate system.

Based on the notation, illustrations and orientations in figure 26 it is possible to find standardized Equations for the directional stiffness in the horizontal plane. These equations include surge, sway and yaw motion expressed in equation [87, 88, 89] respectively. Here, it is important to emphasize that the definition of the angle ψ_i is the definition highlighted in figure 26, between the body coordinate system x-axis in surge direction and the mooring lines, with heading angle $\beta = 0$.

$$K_{11} = C_{11} = \sum_{i=1}^{n} k_i \cdot \cos{\psi_i}^2 \tag{87}$$

$$K_{22} = C_{22} = \sum_{i=1}^{n} k_i \cdot \sin{\psi_i}^2 \tag{88}$$

$$K_{66} = C_{66} = \sum_{i=1}^{n} k_i (x_i \cdot \sin\psi_i - y_i \cdot \cos\psi_i)^2 \tag{89}$$

When modeling the horizontal stiffness in WAMIT, the coefficients are plotted for $\beta = 0$. When changing the heading, WAMIT uses the same equations listed above, where the stiffness coefficients are adapted according to the orientation between the mooring lines, the body coordinate system and the heading angle. as illustrated in figure 27.

From the same relation, the total restoring force can be estimated for the surge, sway and yaw direction as expressed in equation [90, 91, 92] respectively. As mentioned earlier, for the moored structure to be in an equilibrium position i.e stationary, the restoring force must balance the forces from waves, wind and current. This means that the sum of horizontal tension in each respective mooring line (T_{Hi}) must equal the total restoring force (F_H).

$$F_{(11)\ H} = F_{11} = \sum_{i=1}^{n} T_{Hi} \cdot \cos\psi_i \tag{90}$$

$$F_{(22)\ H} = F_{22} = \sum_{i=1}^{n} T_{Hi} \cdot \sin\psi_i \tag{91}$$

$$F_{(66)\ H} = F_{66} = \sum_{i=1}^{n} T_{Hi} (x_i \cdot \sin{\psi_i}^2 - y_i \cdot \cos\psi_i) \tag{92}$$

2.3.8 Free surface effects

Structures containing liquid with a free surface is prone to different phenomenons that have the ability to influence its physical behavior. This section will briefly discuss static instability connected to the internal water mass when the structure moves in roll and pitch, as well as the sloshing phenomenon which has the ability to amplify the dynamic motion of the system.

Static stability and displacement of the center of gravity

From a static stability point of view, the internal water mass can destabilize the structure due to the free surface effect. This effect is connected to the displacement of the gravity center due to the uneven distribution of water inside the structure when it moves in roll and/or pitch. It can cause severe amplification of the angular motions until the point where the righting moment caused by the increased displaced volume on the lowered side is insufficient to stabilize the structure [19]. This is illustrated in figure 28.

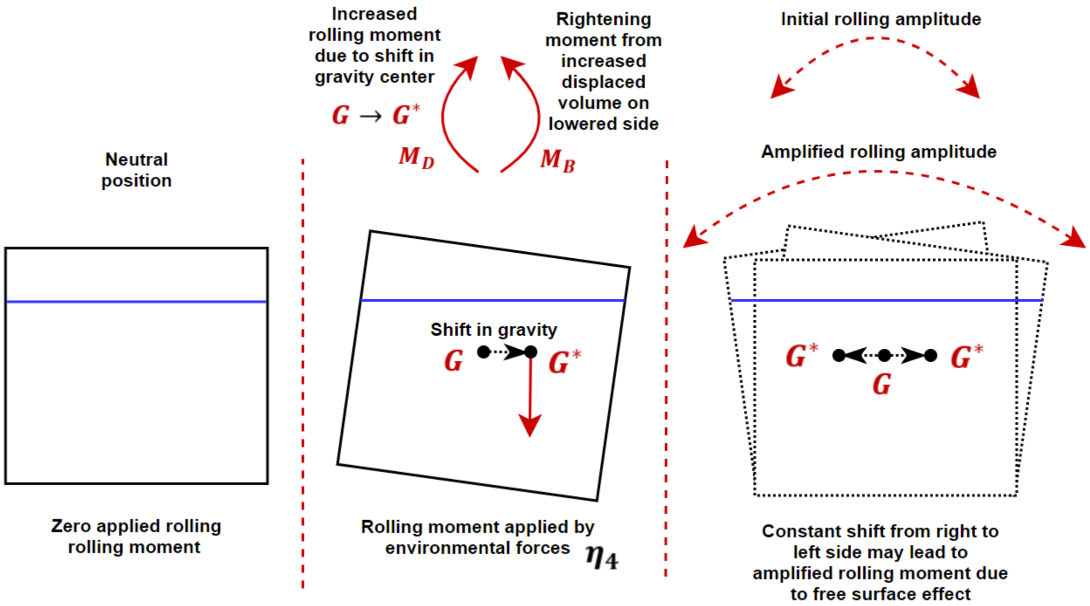

Figure 28: Static instability phenomenon connected to internal water mass effects

This phenomenon is important to consider when designing the floater and membrane of the structure. The significance can be studied from studying the RAO in pitch and heave from the dynamic analysis in WAMIT, and further evaluate if the static stability is threatened by the amplitude of the angular motion. Here it is important to remember that that the physical behavior between a rigid and elastic structure will be significantly different, where the rigid structure is more prone to static instability from free surface effects.

Dynamic stability and sloshing

If the motion induced by the wave excitation forces on the structure is sufficient, a wave connected to internal water mass may develop. The wave depends on the geometry of the structure relative to its motion and the internal water mass. This means that different waves will develop depending on the period of oscillation of the structure and its geometry. The different wave formations are referred to as eigenmodes and are highly interesting with regards to sloshing [35].

The sloshing phenomenon can cause several problems for a structure such as fatigue, material damage and amplification of motions. It is of upmost importance if the system oscillates with the same period as one of the highest natural periods (T_L) of the enclosed water. This can cause violent resonant sloshing behavior were the internal water mass takes the form as a specific eigenmode. According to linear theory, this can happen for lateral (η_1 and η_2) and angular (η_4 and η_5) motions.

The natural periods of the liquid within a structure is highly dependent on geometry and the liquid depth to tank length ratio. In addition, the phenomenon is hard to control and likely to escalate due to low damping of the internal fluid motion. The low damping is due to zero radiated waves, as wave radiation is impossible within a small enclosed volume. In addition, there is low viscous damping in structures composed of smooth fabric membranes such as CFFC‘s [35].

Figure 29 illustrates a typical scenario where sloshing can largely influence a closed fish farm structure, where the structure oscillates in the wave frequency regime with period (T_{1S}) inducing an internal wave with an eigenmode connected to a large natural period (T_{L1}).

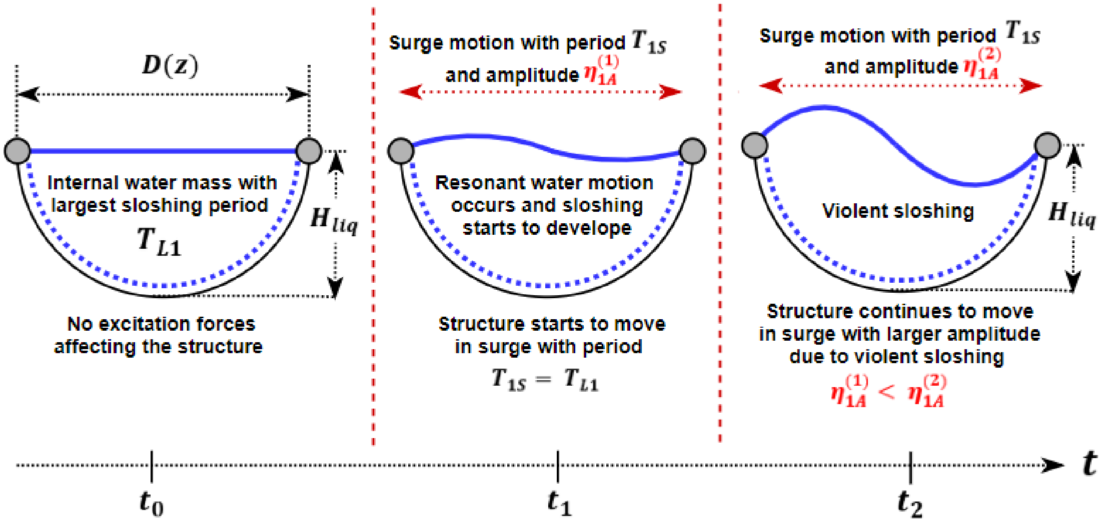

Figure 29: Amplification of amplitude in surge (η_{1A}) due to sloshing

In this paper, the eigenmodes of the designs have been found from [27] By P.McIver. Here the eigenmodes have been found for m = 0, 1, 2, 3, where m is the azimuthal wavenumber, for the four lowest eigenmodes. The table presented in the publication presents the eigenmodes in the form of wavenumbers (k), Where the period of the eigenmode can be found from equation 93.

$$T_{Ln} = \sqrt{\frac{Kg}{R_m}} \tag{93}$$

Here, n = 1, 2, 3, 4 denotes the number of the different eigenmodes and R_m denotes the radius of the structure. In WAMIT, the internal water mass is accounted for by modeling a free surface tank enclosed by the external membrane. The free surface boundary condition on the inside of the tank is linearized in the same manner as the exterior free surface. Since there is no wave diffraction or incident wave connected to the behavior of the internal water mass, the wave velocity potential is governed by the radiation potential and the total velocity potential (ϕ) expressed in equation 94.

$$\varphi = \varphi_R = i\omega \sum_{j=1}^{6} \eta_{jA}\varphi_j \tag{94}$$

Further, the first-order pressure from the internal water column on any given point inside the tank surface can be found from the Bernoulli equation 7, including the hydrostatic and linearized dynamic pressure term. The pressure connected to the internal water mass can then be expressed by equation 95.

$$P = -\rho g[z_m + \underbrace{(\eta_3 + \eta_4 y - \eta_5 x)}_{\boldsymbol{S_3}} - z_t] - \rho\frac{\partial\phi}{\partial t} \tag{95}$$

The first term accounts for the hydrostatic pressure, which changes as the structure moves in the wave frequency regime denoted by the vertical motion $\boldsymbol{S_3}$. The second term accounts for the dynamic pressure connected to the radiated wave inside the tank [25] (Chapter 12).

Figure 30 illustrates how the hydrostatic pressure on an arbitrary point $p(x, y)$, inside a rectangular tank covering the inside of a structure is affected by the vertical motion of the body. This can be seen as the vertical distance from the tank free surface to the point $p(x, y)$ changes as the body is suspected to heave and pitch motion in the wave frequency regime. It also shows how an internal wave with velocity potential ϕ affects the structure.

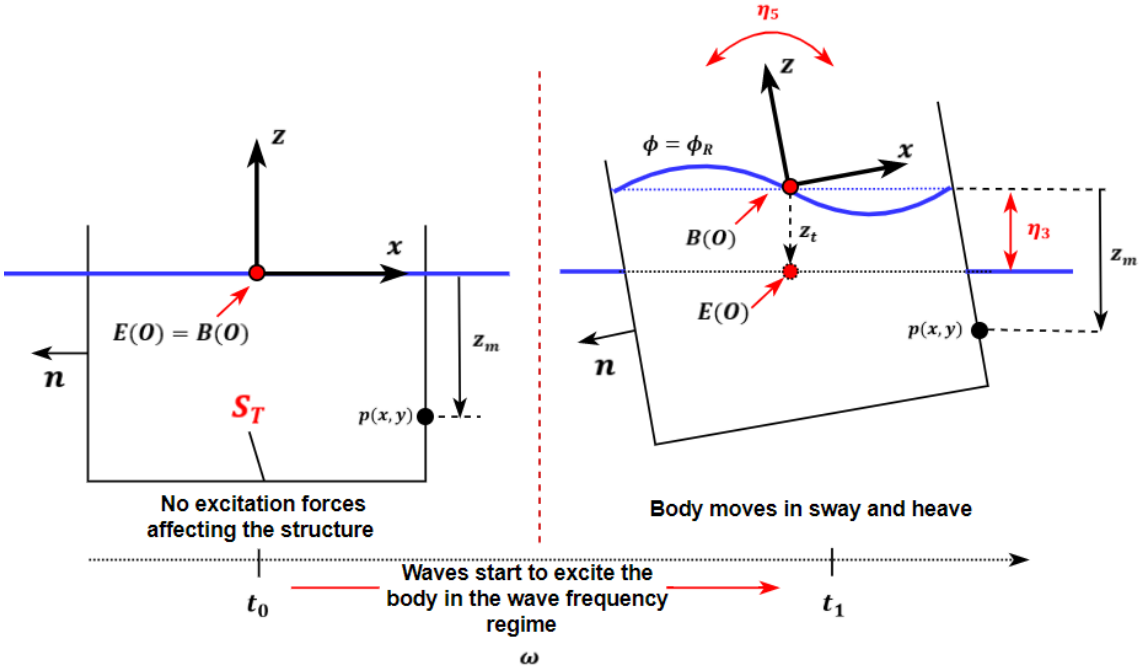

Figure 30: Internal water mass effect and hydrostatic pressure on the internal wall

Here, the free surface of the tank is in the free surface of the surrounding water mass when the structure is unaffected by waves, assuming that the CFFC has a 100% water filling level. $E(O)$ and $B(O)$ denotes the origin of the body fixed and free surface fixed coordinate systems respectively, showing that when there are no excitation forces affecting the system $E(O) = B(O)$. When the system is affected by waves, $B(O)$ follows the undisturbed free surface of the CFFC internal water mass while $E(O)$ is unaffected, making it possible to define the relative motions of the system [25] (Chapter 12).

z_t is the vertical coordinate between the free surface fixed coordinate system in the internal free surface and the origin $E(0)$, and z_m is the vertical distance from the free surface fixed coordinate system to the point of interest $p(x, y)$ defined in figure 5.

The rectangular cross section is used to better understand how the hydrostatic pressure of an arbitrary point is affected by the motion of the structure, but the same principle applies for hemispherical and semi ellipsoid shaped designs. The figure also illustrates how the dynamic pressure is governed by the radiation velocity potential ($\phi = \phi_R$) [25] (Chapter 12).

The radiation potential for the wave fluid motion inside the tank is computed by WAMIT in the same manner as for the external wave radiation potential using the numerical low order panel method. The difference is that the velocity potential is evaluated over the tank surface (S_T) instead of the membrane surface (S_B). From the pressure, the force exerted by the tank fluid on the body is found from integrating the pressure (P) over the wetted surface of the tank as expressed in equation 96.

$$F_{(T)} = \iint_{S_T} P\boldsymbol{N} dS = \iint_{S_T} P(\boldsymbol{n} + \boldsymbol{\alpha} \times \boldsymbol{n}) dS \tag{96}$$

Here, $\boldsymbol{N} = N_1, N_2, N_3$ which can be written on the same form as the rigid body motions in section 2.1. Deriving expressions for the normal vectors ($\boldsymbol{N}$) we get the notation expressed in equation 97.

$$\boldsymbol{N} = n_1 i + n_2 j + n_3 k + \boldsymbol{\alpha} \times \boldsymbol{n} \tag{97}$$

Expanding the expression, the directional normal vectors can be found from equation 98.

$$\boldsymbol{N} = \underbrace{(n_1 + n_3\eta_5 - n_2\eta_6)i}_{N_1} + \underbrace{(n_2 + n_1\eta_6 - n_3\eta_4)j}_{N_2} + \underbrace{(n_3 + n_2\eta_4 - n_1\eta_5)k}_{N_3} \tag{98}$$

From the definition of the normal vector ($\boldsymbol{N}$), the force in surge direction due to the internal water mass can be written on the form expressed in equation 99.

$$F_{1(T)} = \iint_{S_T} P N_1 dS = \iint_{S_T} P(n_1 + n_3\eta_5 - n_2\eta_6) dS \tag{99}$$

The force from the internal water mass is found from evaluating the pressure over the N-panels defining the internal tank, using the panel method in a similar manner as for external waves affecting the body surface (S_B) [25] (Chapter 12).

The moments are derived in a similar manner as the forces. The method can be found in the WAMIT user manual and will not be further discussed in this paper. From the moments and forces, contributions to the hydrodynamic coefficients from the internal water mass can be found [25].

2.3.9 Eigenperiod in surge

The Undamped eigenperiod in surge can be found from reviewing the EQM expressed in Equation 22, ignoring the damping contribution and setting the excitation forces equal to zero.

The excitation force can be set to zero due to the assumption that the system is freely oscillating without any external forces affecting the system. This is illustrated by equation 100 where the damping term and excitation force have been set to zero [36].

$$(M_{11} + A_{11})\ddot{\eta}_1 + K_{11}\eta_1 = 0 \tag{100}$$

Introducing the sinusoidal motion expressed in equation 11, and finding the acceleration ($\ddot{\eta}_1$) as the double derivative of the motion, equation 100 can be manipulated to express the eigenperiod of the system as expressed in equation 101.

$$T_{1n} = 2\pi\sqrt{\frac{(M_{11} + A_{11})}{K_{11}}} \tag{101}$$

The significance of the eigenperiod is especially important when it comes to the resonance phenomenon. Resonance occurs if the eigenperiod of the system is equal to the period of incoming environmental forces, or if the CFFC internal water mass takes the form as an eigenmode close to or equal to the eigenperiod of the system. Reviewing equation 101 it can be seen that the eigenperiod is highly dependent on the mass and stiffness of the system. Due to its dependence on mass and stiffness, the horizontal eigenperiod in surge and sway of large volume structures is often very high. This is due to the relatively small stiffness provided by the mooring system compared to the large mass. It also means that resonance is very unlikely to happen for wave-frequency motion in surge and sway, but that second-order forces in the form of difference frequency effects can be highly influential. This is more carefully investigated in section 5.3.4, making a qualitative estimation of the possible influence of slowly varying effects [16] (Chapter 1).

For vertical translational and angular motion in the form of heave, pitch and roll, the eigenperiods are usually much smaller due to the stiffness being dependent on the hydrostatic pressure on the surface of the body, and change in buoyancy as the body oscillate vertically. This means that for vertical motions, resonance is much more likely to happen in the wave-frequency regime [36].

It is also worth mentioning that the eigenperiod of the system is time and frequency varying depending on the parameters K_{11} and A_{11}. In the case of geometric stiffness often provided by chains in the mooring system, K_{11} is nonlinear as illustrated in figure 25. This means that the system can have more than one eigenperiod depending on the horizontal offset of the system (ΔX). In addition, as the added mass is frequency dependent, the eigenperiod changes for different oscillation periods.

2.4 Static analysis

The static analysis accounts for mean wave drift forces from waves ($F_{i(md)}$) and forces from uniform current ($F_{i(c)}$). The assumption of uniform current means that the current is assumed to have an equal impact on the structure throughout the water column. To find forces from the current, Morison's Equation is utilized. Figure 31 illustrates the body suspected to current and mean drift forces, leading to a horizontal offset in surge direction.

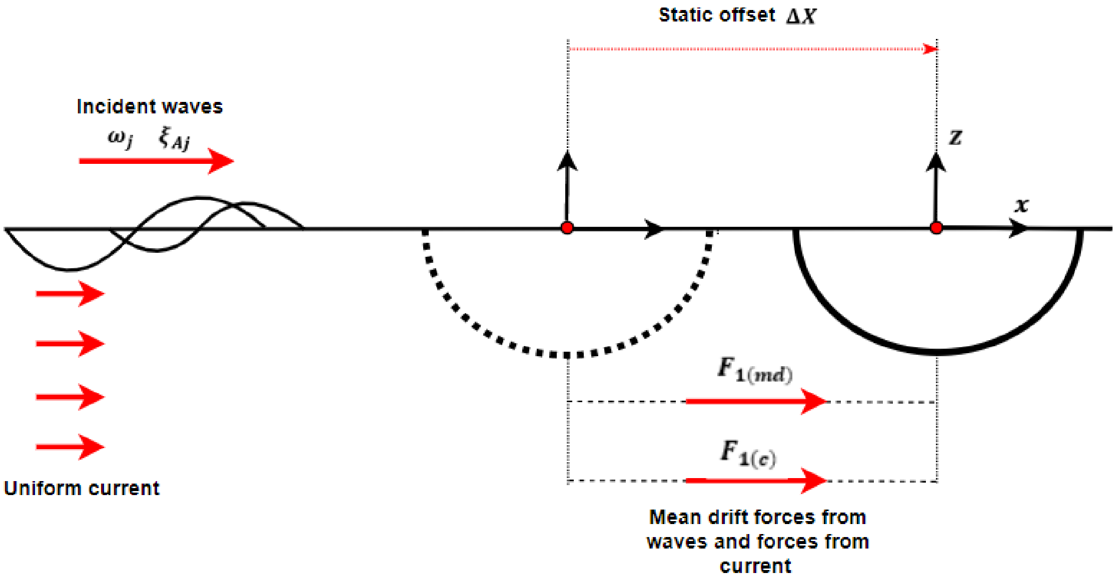

Figure 31: Body suspected to mean drift forces and current

The mean drift force is of second-order in the wave amplitude, but can be evaluated from first-order linear potential. This is due to the fact that the pressure from the second-order velocity potential (ϕ_2) does not contribute to mean loads [12] (Chapter 5). In WAMIT, two methods are available to find the mean drift force on the structure. The first and most general method is direct pressure integration, where the pressure is integrated over the body surface. The second method is based on the principle of momentum conservation. In this paper, the second method based on the conservation of fluid momentum is used [16] (Chapter 1). This is due to its simpler form when evaluating the horizontal drift forces, easing the strain of the numerical solver in WAMIT, in addition to being less prone to numerical errors [24] (Chapter 2).

2.4.1 Mean wave drift forces

The mean wave drift force is the constant force exerted by the wave in the wave-body interaction problem. Each incident regular wave in the sea state has its own contribution to the mean force, as illustrated in figure 31. In potential theory, it is possible to show that the horizontal mean drift forces are closely connected to the body and its capability to generate waves. This means that mean wave drift forces are highly important for large volume structures [16] (Chapter 6).

The horizontal drift force can be found from the principle of Momentum conservation. This method is based on the principle that the amount of momentum in an enclosed volume remains constant if there are no forces acting on the volume. This means that time variations of the fluid momentum is governed by the forces acting on the enclosed volume and its surface, together with the flux of momentum passing the system boundary.

Figure 32 illustrates the boundaries for the conservation of fluid momentum method.

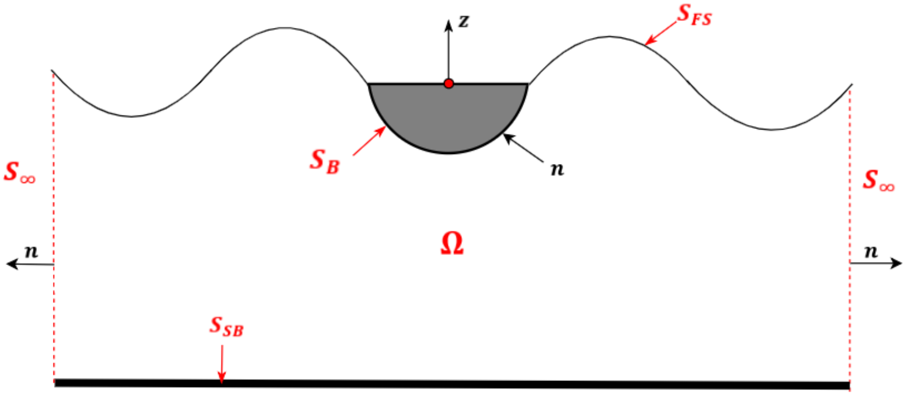

Figure 32: Boundary conditions when defining the conservation of fluid momentum

By using the control surfaces (S_∞) and the solid and free surfaces (S_{FS}, S_B, S_{SB}), the total boundary surface (S) can be expressed by equation 102.

$$S = S_\infty + S_{FS} + S_B + S_{SB} \tag{102}$$

Here, the total fluid domain is denoted Ω and the boundary conditions are defined by the normal component of the velocity of the surface ($\boldsymbol{U_N}$) and the normal component of the fluid velocity at the surface ($\boldsymbol{V_N}$). From the definitions of ($\boldsymbol{U_N}$) and ($\boldsymbol{V_N}$), the boundary conditions for the different surfaces are expressed in equation [103, 104].

Boundary condition for the volume control surface (S_∞)

$$\boldsymbol{U_N} = 0 \tag{103}$$

Boundary condition for the free and solid surfaces ($S_{FS} + S_B + S_{SB}$)

$$\boldsymbol{U_N} = \boldsymbol{V_N} \tag{104}$$

Equation 105 expresses how the fluid momentum can change when forces act on the volume (Ω) and/or the free surface, or by net flux of momentum passing through the enclosing surface [16] (Chapter 6).

$$\underbrace{\frac{d}{dt}\left(\int_{\Omega}\rho V d\Omega\right)}_{=\boldsymbol{M}} = F_S + F_V - \underbrace{\int_S \rho V(V_N - U_N) dS}_{>0=\boldsymbol{flux\,leaves}} \tag{105}$$

Here, the left-hand side represents the time variation of the fluid momentum ($\boldsymbol{M}$), F_S and F_V represent the forces acting on the volume and surface respectively, whilst the last integral to the right represents momentum flux leaving the volume. $\boldsymbol{V}$ is the fluid velocity defined in equation 12.

Further, by manipulating equation 105 using Reynolds transport theorem as well as the Bernoulli Equation in 7, the mean drift force in surge can be written as the integral over a far-field control surface (S_∞) as expressed in equation 106 [26].

$$F_{1(md)} = -\overline{\iint_{S_\infty} (\rho n_1 + \rho V_1 V_N) dS} \tag{106}$$

Here, V_1 is the fluid velocity in surge direction, and the overline represent that we have a time average quantity. In WAMIT, the Kochin function in equation 107, makes it possible to calculate the complex amplitudes of the velocity potential at an infinite distance from the body, using a body surface integral [24] (Chapter 2).

$$H(\theta) = \iint_{S_B} \left[\frac{\partial \varphi_B}{\partial n}\varphi - \varphi_B \frac{\partial \varphi}{\partial n}\right] dS \tag{107}$$

Here, φ_B = φ_S + φ_R, is the sum of the radiated and scattered wave velocity potential traveling away from the body and φ is expressed in equation 108.

$$\varphi = e^{Kz} e^{iKx\cos\beta - iKy\sin\beta} \tag{108}$$

This far-field approach is illustrated in figure 33, where the velocity potentials for the scattered and radiated wave is defined at an infinite distance from the body. Here θ_1 and θ_2 illustrate how the Kochin function is evaluated at different azimuth angles, and R_∞ illustrates that we are at an infinite distance away from the body at S_∞.

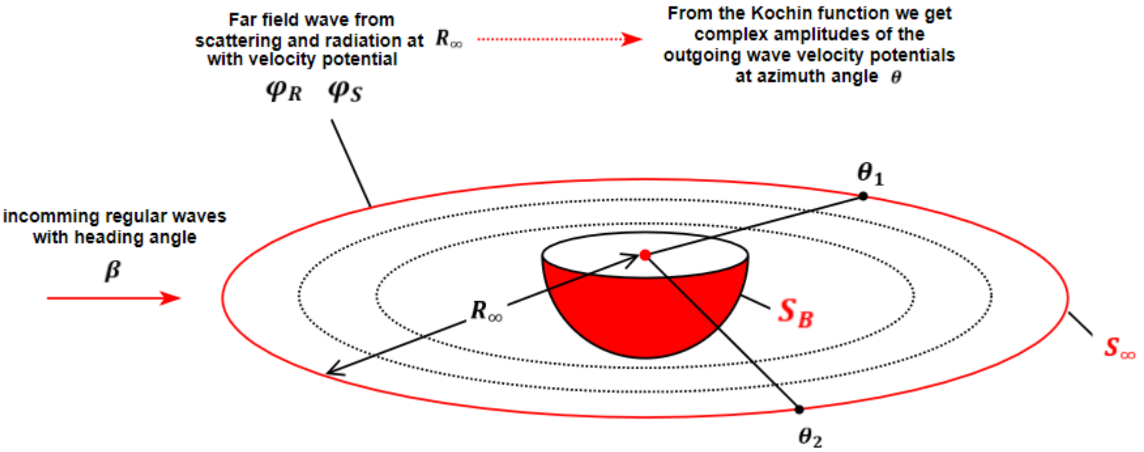

Figure 33: The far-field approach used in conservation of fluid momentum

By employing the Kochin function in Marous formula, the mean drift force can be found as a body integral instead of an integral over the control surface (S_∞). This is done through expressing V_N and V_1 in equation 106, as functions of the far field velocity potentials obtained by the Kochin function. The mean drift force can then be written on the form in equation 109 for the surge and sway direction for deep water waves [1].

$$\begin{pmatrix} F_{1(md)} \\ F_{2(md)} \end{pmatrix} = \frac{\rho K^2}{8\pi} \int_0^{2\pi} |H(\theta)|^2 \begin{pmatrix} \cos\theta \\ \sin\theta \end{pmatrix} d\theta - \frac{\rho\omega\xi_A}{2K} \begin{pmatrix} \cos\beta \\ \sin\beta \end{pmatrix} \Im\left\{H'(\pi+\beta)\right\} \tag{109}$$

Here, both the radiated and scattered wave velocity potential is included through the Kochin function due to the close connection between mean drift forces and the body capability to generate waves.

In WAMIT, the total mean drift force from using the low order panel method, is found from using the same integration technique as in the radiation problem, summing the integral contributions from each panel (k) over the number of N panels. Here, the Kochin function is the part of the mean drift equation that is evaluated over each individual panel [24] (Chapter 2).

When running tests in WAMIT the mean drift force is output on the nondimensional form expressed in equation 110 for the different wave periods specified in the potential file.

$$\overline{F}_{i(md)} = \frac{F_{i(md)}}{\rho g\, {\zeta_A}^2\, L^k} \tag{110}$$

Where k = 1 for motion in surge, sway and heave and L is the length scale defined by the characteristic length ULEN when specifying the geometry file in WAMIT. When the geometry is defined in its full-scale L = 1. To get the total mean drift force when the structure is affected by irregular seas, the different contributions to the drift force from the different wave periods have to be combined by using equation 111. The equation illustrates the method for finding the total mean drift force when there is N number of regular waves affecting the structure for unidirectional waves. Unidirectional waves mean that the structure is affected by waves from the same heading angle [25] (Chapter 4).

$$F_{i(md\,tot)} = \rho g \sum_{n=1}^{N} = ({\zeta_{An}}^2 \cdot \overline{F}_{i(md)n}) \tag{111}$$

here ζ_{An} is the amplitude of the n'th regular wave in the irregular sea state affecting the structure, found from superimposing the irregular sea state into regular sinusoidal waves from equation 121. The irregular sea-state used throughout this paper is more closely defined in section 2.5.

2.4.2 Forces from current

Drag forces from current will be evaluated by the use of Morison's equation 112. The equation normally consists of two parts, connected to a drag and mass force. As the mass force is connected to the fluid acceleration, it will not be considered in this paper due to the assumption of steady uniform flow [12] (Chapter 7).

$$F_{i(c)} = \frac{1}{2}\rho C_d A {V_c}^2 \qquad\qquad i = 1,2 \tag{112}$$

As explained in section 2.3.6 concerning Eddy making damping effects, the drag force from current originates from water particles interacting with the surface of the structure. Due to the relatively smooth surface of a CFFC body, the drag force is assumed to be dominated by Eddy making, where vortexes shed off the structure in the separation point in the Boundary layer surrounding the surface [36]. This is illustrated in figure 34.

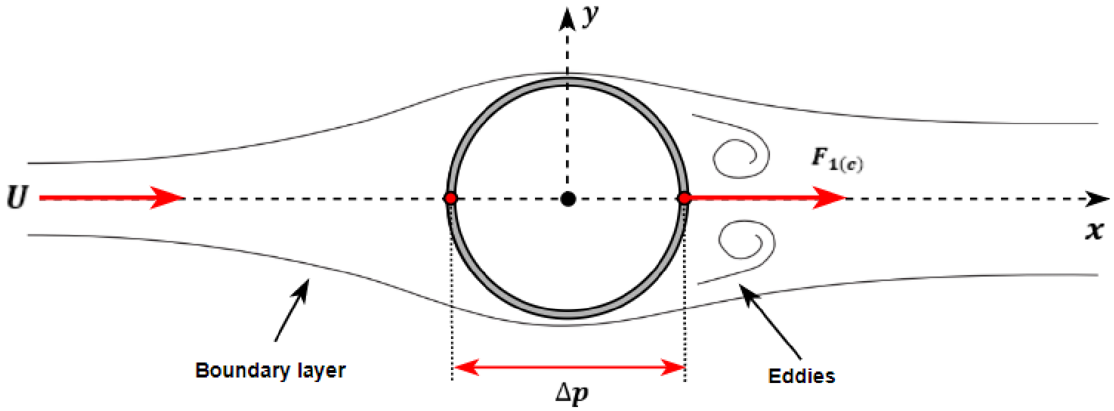

Figure 34: Drag force from current on a 2D circular circumference

In Morison's equation, C_d is the drag coefficient, A is the projected area affected by the flow, and V_c is the current velocity. Figure 35 illustrates the definition of the area affected by the flow.

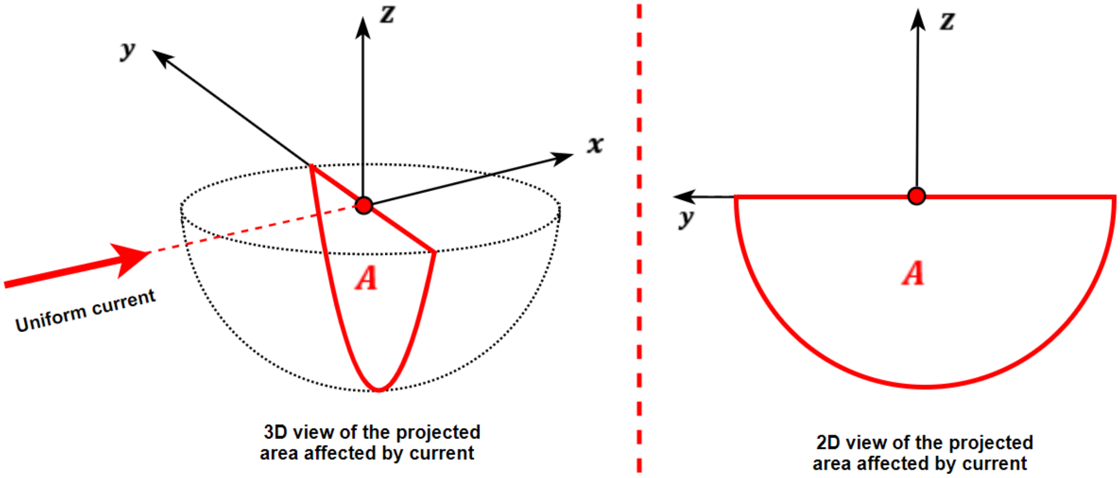

3D view of the projected area affected by current

2D view of the projected area affected by current

Figure 35: The definition of the projected area A for a hemispherical design

The drag coefficient (C_d) is dependent on the Reynolds number (Re) expressed in equation 113, which indicates if the flow is turbulent or laminar.

$$Re = \frac{V_c\, D}{\nu} \tag{113}$$

This dimensionless quantity varies for any given geometry, depending on the characteristic linear dimension (D), the velocity of the flow and the kinematic viscosity of the fluid (ν). This means that the drag force varies with the drag coefficient, which again changes with the Reynolds number for any given geometry.

Figure 36 shows the drag coefficient as a function of Reynolds number for a smooth sphere and a smooth cylinder affected by current. Results can be found in [38] by Schlichting, Hermann and Gersten. The figure can be used to approximate an acceptable drag coefficient for the hemispherical and semi ellipsoid shaped designs evaluated in this paper.

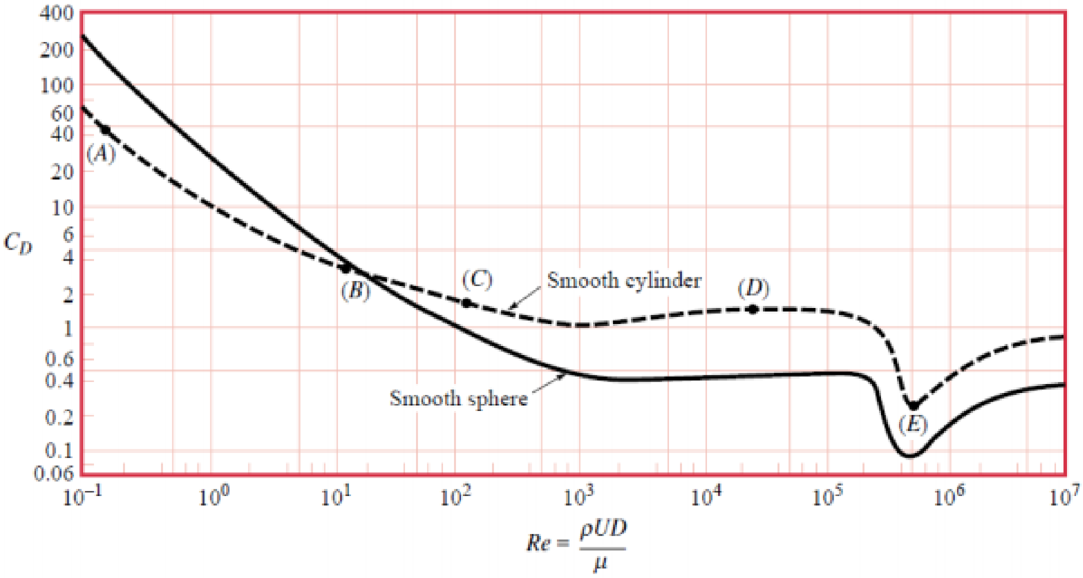

Figure 36: Drag coefficient as a function of Reynolds number

From the figure, it can be seen that for high Reynolds numbers, the spherical geometry is subject to lower values for the drag coefficient than the cylindrical geometry. This is due to the presence of sharp edges on the cylindrical geometry, which leads to more vortex shedding and drag [36].

2.5 Irregular sea state

This section describes how the results from the WAMIT simulation including RAO's from the wave frequency analysis and the nondimensional mean drift coefficients from the static analysis, are used in combination with irregular sea states to obtain forces and motions used in the mooring system analysis.

The wave conditions for the dynamic analysis investigated in this paper are limited to high and substantial exposure with T_p and H_s defined in table 1. To obtain results from the RAO's found from the wave-frequency analysis in WAMIT, a common spectrum of the Pierson-Moskowitz type is used. The spectrum describes the energy distribution for a fully developed sea state with deep water waves and no swell, where the wind has blown steadily over a large area for a long time. The typical form of the PM-spectrum can be seen in figure 37, identified by its steep front and more gradual decline for high frequencies.

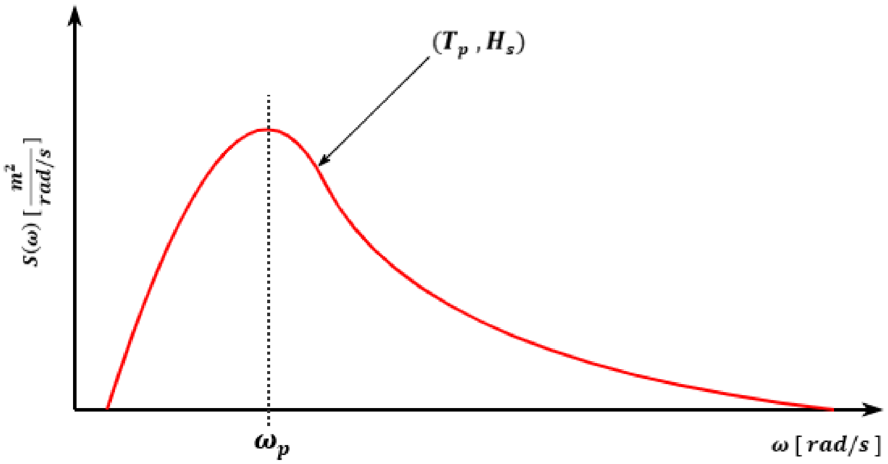

Figure 37: PM Wave spectrum with peak-period (T_p) and significant wave height (H_s)

The spectral values connected to the energy in the sea state is expressed in equation 114 taken from DNV-RP-H103 [46] (Chapter 2). Here, the spectral energy is given by the significant wave height and the peak period for different frequencies within the sea state.

$$S(\omega)' = \frac{5}{16} {H_s}^2 {\omega_p}^4 \omega^{-5} exp\Big(-\frac{5}{4}(\frac{\omega}{\omega_p})^{-4}\Big) \tag{114}$$

To be able to use PM-spectrum defined by DNV-GL in equation 114, the spectrum needs to be fitted to the sea states evaluated in this paper. This is done by scaling the spectrum, using the ratio of the spectral moment of the DNV defined spectrum, to the actual moment defined by the significant wave height investigated in this paper. The spectral moment defined by the spectrum and significant wave height is expressed in equation 115.

$$m_0 = \frac{{H_s}^2}{16} \quad , \quad m_0 = \int_0^\infty S(\omega)' d\omega \tag{115}$$

From the moments, The modified PM-spectrum used in this paper is expressed in equation 116.

$$S(\omega) = \frac{{H_s}^2}{16} \cdot \left(\int_0^\infty S(\omega)' d\omega \right)^{-1} \cdot S(\omega)' \tag{116}$$

$S(\omega)$ is the spectrum used throughout this thesis and ${H_s}^2/16$ is the spectral moment of zero order. Further, by multiplying the frequency dependent spectral energy with the frequency dependent RAO to the second power, the energy spectrum representing the surge motion of the system can be found ($S_x(\omega)$) [46] (Chapter 2). This is expressed in equation 117.

$$S_x(\omega) = RAO^2 \cdot S(\omega) \tag{117}$$

The spectrum representing the surge motion is illustrated in figure 38. This spectrum can be used to find the most probable maximum surge excitation (X_{dyn}) over a certain time frame, based on the sea state in question. [7].

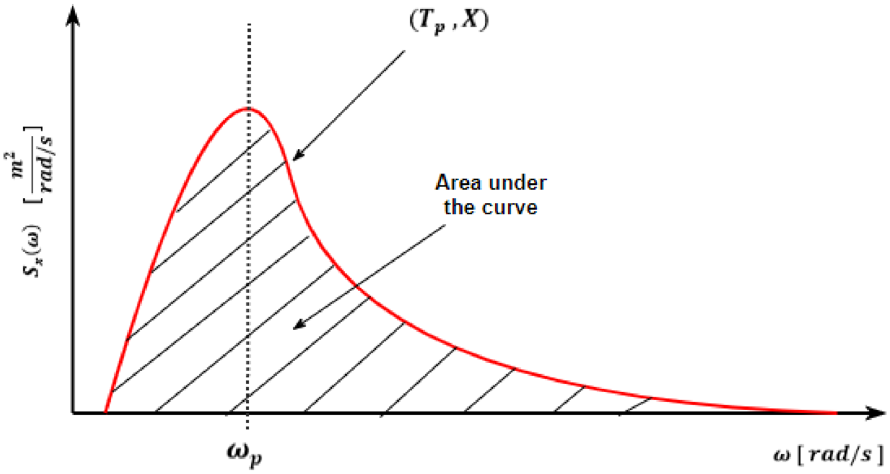

Figure 38: Response spectrum obtained from RAO and wave-spectrum

The standard deviation of the surge motion (σ_x) can be found from the area under the graph as expressed in equation 118.

$$\sigma_x = \sqrt{\int_0^\infty S_x(\omega) d\omega} \tag{118}$$

Assuming Rayleigh distributed waves, the standard deviation of the surge motion spectrum can be used to find the most probable maximum surge excitation for the sea state, as expressed in equation 119.

$$X_{dyn} = \sigma_x \cdot \sqrt{2ln(N_w)} \tag{119}$$

Here N_w is found as the average number of waves over the measurement period, where the sea state is measured over a 3 hour time window which is common practice in the aquaculture industry according to NS9415 [43]. This means that N can be found from equation 120.

$$N_w = \frac{3 \cdot 60 \cdot 60}{T_z} \tag{120}$$

Here T_z is the mean zero crossing period which can be found from $T_p = 1.4049\,T_z$, assuming that we have a PM-spectrum with $\gamma = 1.0$. This is according to [46] (Chapter 2). When evaluating the mean drift forces from the sea state, the amplitude of any given wave within the spectrum can be expressed on the form in equation 121.

$$\zeta_A = \sqrt{2S(\omega_j)\Delta\omega} \tag{121}$$

Here $S(\omega_j)$ is the spectral value for a given frequency within the spectrum. Using different amplitudes with spacing $\Delta\omega$ in combination with equation 110, summing all the mean drift contributions from the different wave periods the total mean drift force can be obtained using equation 111. The wave elevation for any given sea state represented by a spectrum over a certain time period t can be found from equation 122.

$$\zeta_A(t) = \sum_{j=1}^{N} \sqrt{2S(\omega_j)\Delta\omega} \cdot \cos(\omega_j t + \epsilon_j) \tag{122}$$

Here ϵ_j is a random phase angle in the range between 0 and 2π. The time-varying wave elevation makes it possible to find the maximum and minimum wave elevation within the sea state, as well as evaluate the sea state more analytically [36].

2.6 Froude scaling

Throughout the analysis, results from model scale experiments conducted by SINTEF Ocean in the SJØFLO investigation is used to compare the results from the WAMIT simulation [8]. In addition, the results have been used directly when finding a reasonable percentage of critical damping when accounting for viscous damping effects in the user-specified damping matrix in WAMIT.

The Froude scaling factor can be set as the ratio between the full scale and model scale diameter as expressed in equation 123.

$$\lambda_f = \frac{D_{(full\,scale)}}{D_{(model\,scale)}} \tag{123}$$

The general scaling laws apply to length, mass, force and time as highlighted below.

Length scaling - $\lambda_f \;\; [m]$

Mass scaling - $\lambda_f^{(3)} \;\; [kg]$

Force scaling - $\lambda_f^{(3)} \;\; [N]$

By using the scaling laws, the following paragraph illustrates how the linear damping can be scaled from model to full scale using Froude scaling. In the equation of motion, the linear damping force (F_{Blin}) is given by the damping coefficient multiplied with the harmonic velocity of the oscillating body. This gives the following relation between the velocity and damping coefficient given in equation 124.

$$F_{B\,lin}\,[N] = B_{lin}\,\dot{\eta}\left[\frac{kg}{s}\right]\left[\frac{m}{s}\right] \tag{124}$$

From the unit associated with the damping coefficient, knowing that mass scales with $(\lambda_f)^3$ and time scales with $(\lambda_f)^{0.5}$, the damping coefficient scales with the factor given in equation 125.

$$\frac{(\lambda_f)^3}{(\lambda_f)^{0.5}} = (\lambda_f)^{2.5} \tag{125}$$

3 System description and properties

In this section, parameters, characteristics and properties of the different structures and mooring systems analyzed throughout the thesis will be presented. The physical parameters are included in the user-specified mass, stiffness and damping matrix in the FRC file in WAMIT, denoted as $M^{(e)}$, $C^{(e)}$ and $B^{(e)}$ in the equation of motion 24. The structures are inspired by the Botngard CFFC design highlighted in the following section. The mooring system has been chosen based on commonly used systems in the industry, limited to the orthogonal mooring layout illustrated in figure 48.

3.1 The CFFC system

The geometries investigated in this paper is inspired by Botngard‘s closed technology designs illustrated in figure 39 and 40. The tarp based design are manufactured for closing already existing cages at sea, which makes it optimal for evaluating current mooring systems. The geometries include both a hemispherical and semi elliptical design, where the shape and size can be adapted.

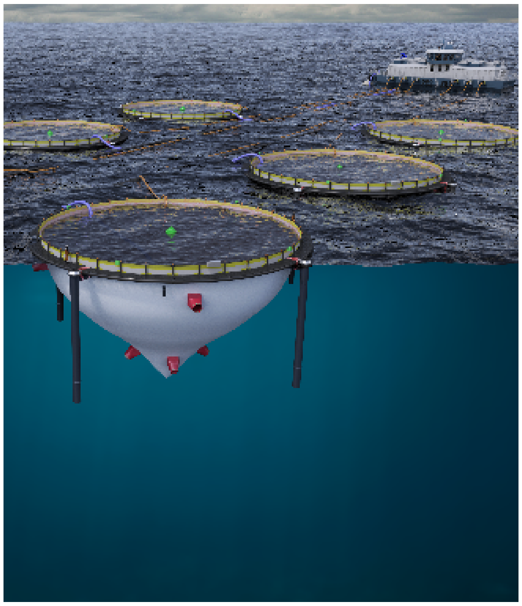

Figure 39: spherical design by Botngaard [2]

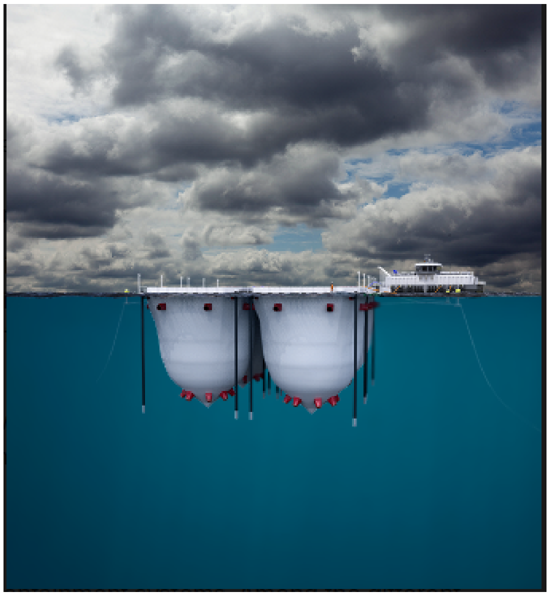

Figure 40: semi ellipsoid design by Botngaard [2]

The membrane consists of fabric, but is treated as rigid when estimating the hydrodynamic forces affecting the system. Neglecting the elasticity makes the hydrodynamic response decoupled from deformation of the bag and the structural response, simplifying the problem significantly [29].

The design has different components such as water inlets and outlets connected to the outside of the bag. These components will be neglected for simplicity in the geometric model, causing some uncertainty in the numerical analysis. Even though the Botngard design illustrated in figure 39 deviate to some extent from a perfect semi ellipsoid geometry, the tarp solution can be adapted to many different designs, making the chosen geometry highly relevant. The following paragraphs give a short description of the main CFFC components included in the physical model for the numerical analysis.

3.1.1 CFFC components

The main components important for the hydrodynamic analysis of the CFFC facility is the membrane, floating collar and internal water mass represented in WAMIT by an internal tank. As the CFFC technology investigated in this paper is based on implementation in already existing cages, the floating collar has been chosen according to already existing technology used by the fish farming industry.

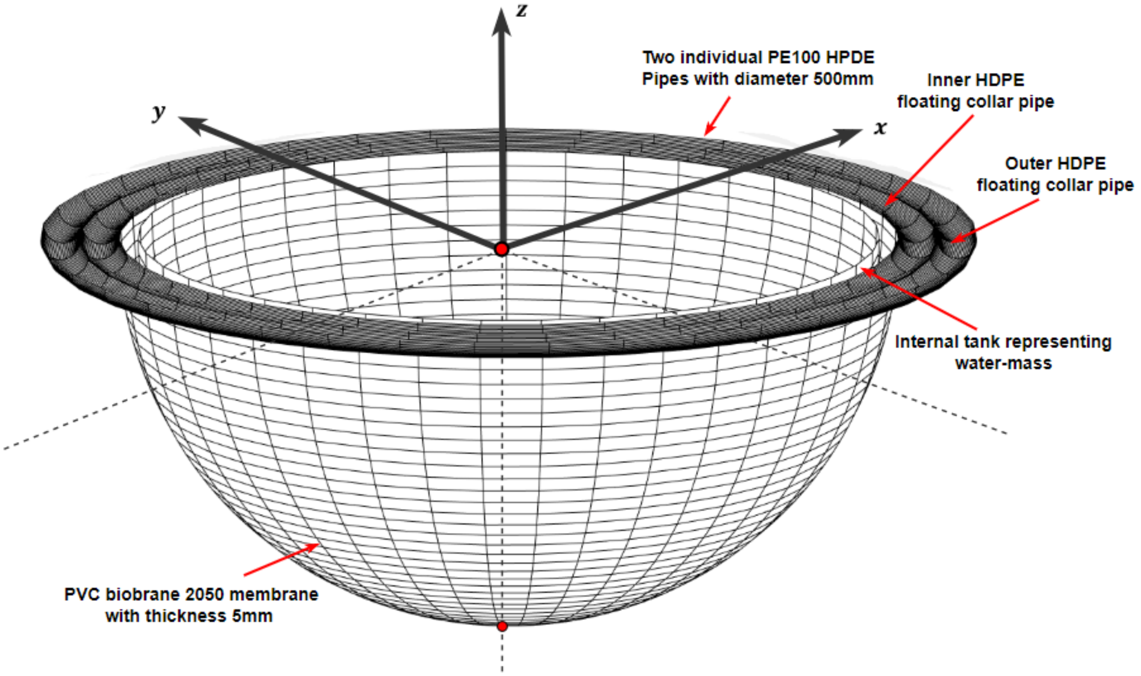

Figure 41: Hemispherical design plotted in MATLAB with body coordinate system

The geometry for the hydrodynamic analysis in WAMIT is plotted in MATLAB using spherical and torodial coordinates as illustrated in figure 41. The spherical coordinates are adapted to account for the semi elliptical shaped geometries in the MATLAB code. The figure shows the submerged part of the hemispherical design including the membrane, the internal tank representing the water mass and two pipes simulating the floating collar. The MATLAB code used to plot the geometry is included in Appendix B.

Membrane

The membrane is used to separate the isolated environment on the inside of the fish pen from outside threats such as fish lice and disease. In addition to protect the inside of the fish pen from outside threats, it protects outside habitats from fish farming residue. The membrane is made out of PVC Polyvinyl chloride designed by Serge Ferrari and goes by the name Biobrane 2050. It has great abrasion characteristics, including an expected life cycle of 5-10 years depending on exposure [13]. Figure 42 shows the Biobrane membrane used in a flexible fish cage in Horsvågen Norway by Cermaq.

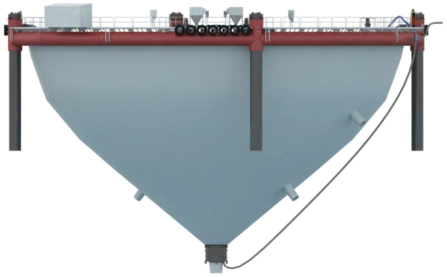

Figure 42: Membrane designed by Serge Ferrari [14]

The membrane gives the structure great absorption characteristics compared to rigid structures made of metal or concrete. It also has a nontoxic characteristic which is essential for use in the aquaculture industry. The E-modulus of the material is very high, which makes it less prone to elongation when suspected to high internal or external tension.

Floating collar

The floating collar forms the outer part of the CFFC facility. For floating cages, the pipes are commonly made of HDPE, which is an excellent material for cage construction. This is due to the characteristics of the material being durable, flexible, shockproof and resistant to UV radiation. It also requires little to no maintenance if installed correctly. Figure 43 shows HDPE pipes used in the floating collar of a fish farm structure.

Figure 43: HDPE pipes used in the floating collar [18]

The main purpose of the floating collar is to provide stiffness and buoyancy to the system. This is archived by filling the interior of the pipes with polystyrene. There are several different materials used for the HDPE pipes, but most common are the PE80 and PE100. These codes refer to the strength of the material, where the PE100 pipe will rupture at a pressure $\geq$ 10.0 N/m over a 50 year service period. Classification of the piping is done with the Standard dimension ratio (SDR) which is the ratio between the outer pipe diameter ($\varnothing$) and thickness (t). In addition the pipes have a Nominal pressure (PN) rating, which is the pressure resistance rating [5] (Chapter 4).

3.1.2 CFFC properties and characteristics

The model designed by the user in WAMIT is divided into the three main components of the CFFC structure including the Membrane, the floating collar and the internal tank. The system parameters are only calculated for the membrane and floating collar and combined into one complete system. Important parameters include mass, moment of inertia and radius of gyration. The moment of inertia and system mass is included in the user-specified mass matrix in the WAMIT FRC file. The properties of the internal water mass are accounted for by the software and is not included in the user-specified mass matrix.

Four different designs with different drought will be evaluated as illustrated in figure 44. The first design with drought H_{m1} is a perfect hemisphere, while design 2, 3 and 4 is semi ellipsoid shaped.

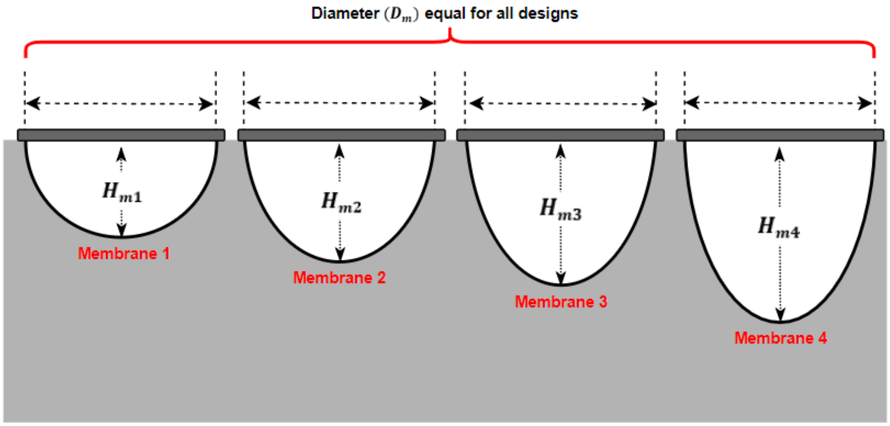

Figure 44: Four different CFFC designs with varying drought

The geometry of the structure represented through the GDF file in WAMIT, account for all components including the floating collar, the membrane and internal tank. Even though the floating collar is represented as two individual pipes when calculating the physical parameters for the FRC file, the collar is modeled as one continuous half torus with diameter $2D_p$ in the GDF file. This was done to decrease the simulation time, and ease the stress on the direct solver in WAMIT. The solver is based on standard Gauss reduction with partial pivoting, solving the large number of equations for the radiation and diffraction problem discussed in section 2.3. This solver was chosen due to problems with the alternative iterative solver, not converging when solving the velocity potentials for the diffraction and radiation problem [25] (Chapter 12).

The half torus representing the collar in the GDF file is also prone to the assumption that the submerged part of the floating collar is constantly 50% of the pipe diameter. The above assumptions can be justified by the fact that the floating collar is far smaller than the surface of the membrane in the wave-body interaction problem. The method used when plotting the GDF file is highlighted in section 2.3.3 for the internal tank and the membrane.

The membrane is modeled as a hemisphere or semi ellipsoid depending on the drought of the system. The internal tank is modeled with the same shape, on the inside of the floating collar, with a thickness equal to t = 1cm. Figure 45 and 46 illustrate one of the geometries with notation used for the membrane and floating collar, highlighting the submerged part of the system. In addition to the geometrical shape of the structure, the figures show the body coordinate system with axes used when estimating the moment of inertia and radii of gyration.

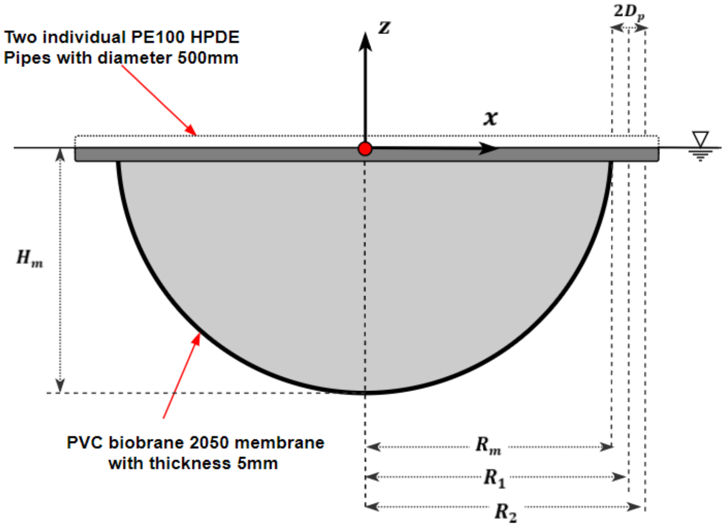

Figure 45: Notation used when defining the CFFC parameters, vertical plane

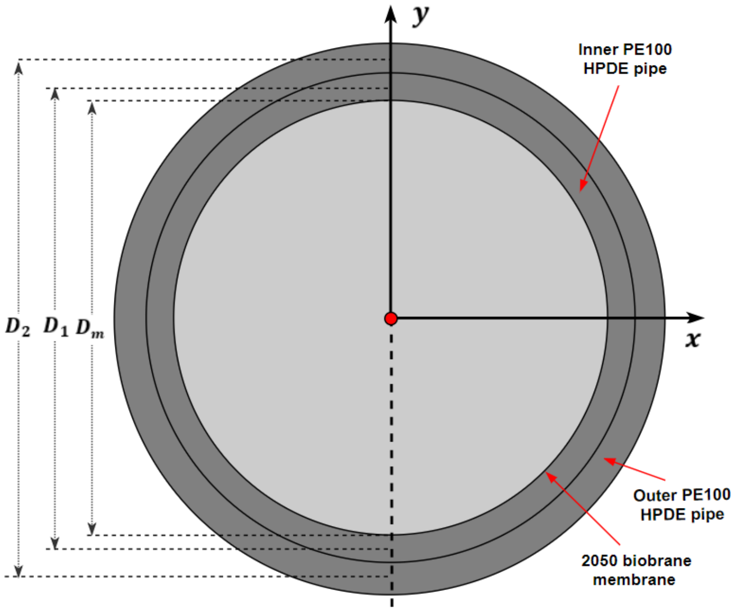

Figure 46: Notation used when defining the CFFC parameters, horizontal plane

Here, R_m is the radius of the membrane, R_1 and R_2 is the radius from the center of the body coordinate system to the center of the inner and outer ring in the floating collar respectively. D_1 and D_2 is the corresponding distance from center to center of the torus-shaped outer and inner pipes in the floating collar.

Table 4 shows the properties of the four different PVC biobrane 2050 membrane designs illustrated in figure 44. The mass is calculated based on Archimedes law ($\nabla = M_m \cdot \rho$) where the membrane is completely submerged. The diameter of the membrane is D_m = 40 meters for all designs and the thickness of the shell is t = 10mm. The breaking strength (MBL) for the material is 14500 N/5cm and the tearing strength T_t = 1500 N [5] (Chapter 4).

Membrane parameters and physical properties					
Membrane number		Membrane 1	Membrane 2	Membrane 3	Membrane 4
Draught (H_m)		20m	24m	26m	28m
Mass (M_m)	$[kg]$	2.57 $\cdot 10^4$	2.92 $\cdot 10^4$	3.09 $\cdot 10^4$	2.26 $\cdot 10^4$
Inertia (I_{xy})	$[kgm^2]$	6.87 $\cdot 10^6$	7.78 $\cdot 10^6$	8.24 $\cdot 10^6$	8.70 $\cdot 10^6$
Inertia (I_z)	$[kgm^2]$	6.87 $\cdot 10^6$	7.78 $\cdot 10^6$	8.24 $\cdot 10^6$	8.70 $\cdot 10^6$
Rad. of gyration (r_{xy})	$[m]$	16.33	16.33	16.33	16.33
Rad. of gyration (r_z)	$[m]$	16.33	16.33	16.33	16.33
Area xy-plane (A_m)	$[m^2]$	1256.6	1508.0	1633.6	1759.3
Center of gravity ($\overline{z}$)	$[m]$	-10.0	-12.0	-13.0	-14.0

Table 4: Membrane parameters, mass and physical properties

The moment of inertia is calculated for a hemispherical shell about the x,y and z axis based on standardized equations found in [30] by Jack A. Myers. This is a respectable assumption even for the semi-ellipsoid shaped designs, due to their relatively small deviation from the spherical shape. This is because the drought of the membrane for the semi-ellipsoid shaped designs are fairly close to the radius. Also, the contribution to the mass and moment of inertia from the membrane is relatively small compared to the contribution from the internal water mass estimated by WAMIT, making deviations less important.

The center of gravity ($\overline{z}$) is defined with respect to the body coordinate system taken as H/2 of each respective membrane design. This is also based on the centroid of a hemispherical shell, justified by the same assumptions as mentioned when estimating the moment of inertia for the semi-ellipsoid design.

Table 5 shows the properties of the inner and outer pipe used in the floating collar. The pipe is of the PE100 with rating PN10 and SDR 13.6 having a diameter of D_p = 0.5 meters [5] (Chapter 4). As for the membrane, the mass is calculated based on Archimedes law assuming that the pipes are floating with drought equal to half the diameter of the pipe. The circumference (O_p) is taken in the center of each respective pipe about the membrane at the top side of the structure.

Floating collar parameters and physical properties			
Pipe		Inner pipe	Outer pipe
Circumference (O_p)		127m	131m
Mass (M_p)	$[kg]$	1.28 $\cdot 10^4$	1.31 $\cdot 10^4$
Inertia (I_{xy})	$[kgm^2]$	2.63 $\cdot 10^6$	2.82 $\cdot 10^6$
Inertia (I_z)	$[kgm^2]$	5.25 $\cdot 10^6$	5.65 $\cdot 10^6$
Radii of gyration (r_{xy})	$[m]$	14.32	14.67
Radii of gyration (r_z)	$[m]$	20.25	20.75

Table 5: Floating collar parameters, mass and physical properties

The moment of inertia is calculated for a torus about the x-,y- and z-axis based on standardized equations found in [30] by Jack A. Myers. The center of gravity for the inner and outer torus has the same z-coordinate as the origin of the body coordinate system. Table 6 shows the physical properties for the different designs highlighted in figure 44 including the floating collar. These are the properties included in the mass/inertia matrix in the FRC file in WAMIT.

Structure parameters and physical properties					
Design number		Design (D_1)	Design (D_2)	Design (D_3)	Design (D_4)
Draught (H_m)		20m	24m	26m	28m
Mass (M_T)	$[kg]$	1.32 $\cdot 10^5$	1.35 $\cdot 10^5$	1.37 $\cdot 10^5$	1.39 $\cdot 10^5$
Inertia (I_{xy})	$[kgm^2]$	3.03 $\cdot 10^7$	3.12 $\cdot 10^7$	3.17 $\cdot 10^7$	3.21 $\cdot 10^7$
Inertia (I_z)	$[kgm^2]$	5.38 $\cdot 10^7$	5.47 $\cdot 10^7$	5.51 $\cdot 10^7$	5.56 $\cdot 10^7$
Radii of gyration (r_{xy})	$[m]$	15.16	15.19	15.20	15.22
Radii of gyration (r_z)	$[m]$	20.19	20.10	20.06	20.01
Center of gravity ($\overline{z}$)	$[m]$	-10.0	-12.0	-13.0	-14.0

Table 6: Structural parameters, mass and physical properties

The four different designs are tested with different mooring line setups highlighted in the following section. This is done by modeling different horizontal stiffness coefficients in the FRC file in WAMIT for the complete fish farm facility through the user-specified damping matrix included in the equation of motion Expressed in equation 24.

3.2 The mooring system

This section highlights the Orthogonal mooring system commonly used in Norwegian aquaculture. The orthogonal layout for a single fish farm facility is illustrated in figure 47 and 48 in the vertical and horizontal plane respectively. The orthogonal layout is also used in facilities consisting of several fish farm structures, but is limited to one structure throughout the thesis.

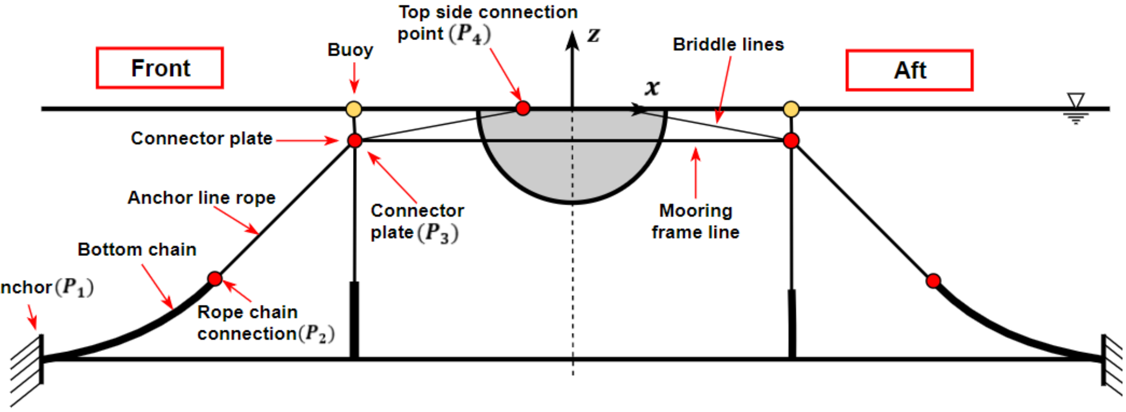

Figure 47: Single closed fish farm facility in the vertical plane

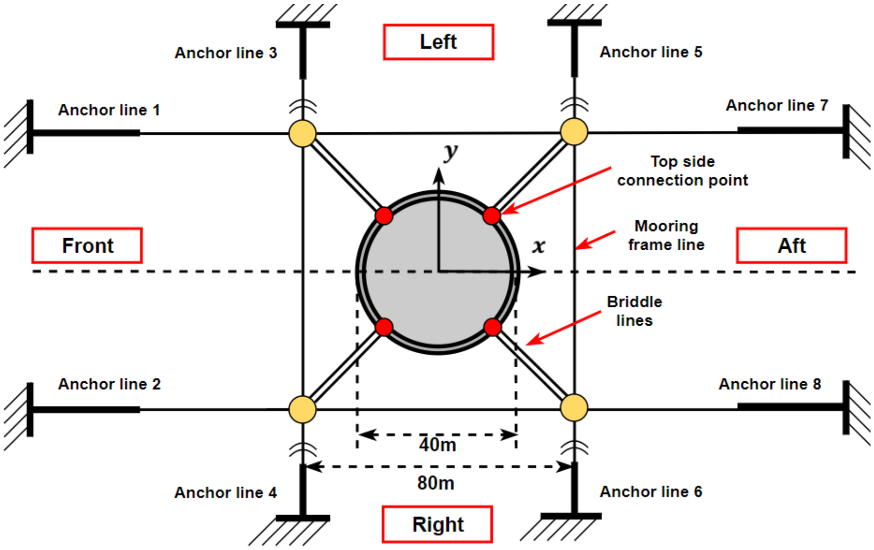

Figure 48: Single closed fish farm facility in the horizontal plane

In the following section, mooring lines with different dimensions will be presented, including their specific characteristics and properties. In addition, the mooring line components together with their intended role in the mooring system layout will be shortly discussed. As all the mooring lines in the mooring system is assumed to have equal length and dimension, a single mooring line will be presented.

3.2.1 Mooring line components

The mooring system components used by the aquaculture industry is very similar to those used by the offshore industry and revolves around the same principles for station keeping. As illustrated in figure 49, the system consists of Bridle lines, Buoys, Ropes, Connector plates, Shackles, Chains and anchors.

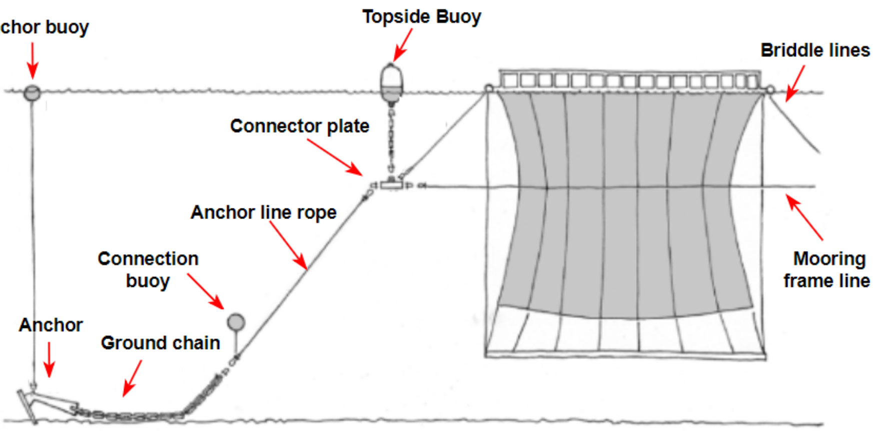

Figure 49: Main mooring system components [5]

Through this section, the main components important for the mooring system‘s stationkeeping abilities will be emphasized. Due to numerous different locations, environmental conditions and implemented systems, different components with different dimensions relevant to the aquaculture industry will be listed [5] (Chapter 3).

The different dimensions and characteristics will be used to establish six different mooring line configurations, this has the sole purpose of representing solutions commonly used by the Norwegian aquaculture industry. Here, the ground chain, the anchor line rope and the bridles will be used to estimate the total stiffness ($k_{11\ M}$) of one single mooring line. The other components of the system will not be accounted for, due to their rather small contribution to system stiffness. All the information about the different components has been found in [5] (Chapter 4) by FAO and the product brochure from Løvold AS, a Norwegian mooring system company.

Chains

This section will focus on the bottom chain part of the mooring line. The main purpose of the bottom chain is to provide restoring through geometric stiffness to the system. There are many types of chain's used by the industry, but the bottom chain is often of the stud chain type illustrated in figure 50. The chain is often tarred to make sure it has the ability to withstand harsh marine environments.

The weight of the chain must be sufficient so that the chain maintains a small angle between the seafloor and the active part of the chain (desired range 9° to 12°), which hangs freely in the water column [5] (Chapter 3). If the weight of the chain is insufficient, clump weights are commonly used. The added weight has the sole purpose to increase the total weight of the bottom chain. This is to ensure that the anchor doesn't get suspected to large vertical forces, leading to instability and an increased probability of mooring system collapse. Normally the stud link is manufactured in continuous 27.5 meter chains, with a varying number of links depending on the chain diameter. Compared to the rope component of the system, the chain also has great abrasion properties. This makes it a robust barrier when the system moves, preventing the rope components scraping along the sea bottom [6].

In addition to the bottom chain, smaller parts of chain are used between the rope components and various connector plates within the system. This is mainly to prevent abrasion and has little to no effect on the total stiffness of the system.

Figure 50: Stud link chain commonly used in the fish farming industry [9]

During the mooring system analysis, different dimensions will be evaluated to find the necessary design to obtain mooring system stability with the implementation of closed containment facilities. This will contribute to indicate the mooring system requirements that must be met at an arbitrary horizontal position to withhold forces from environmental loads.

Ropes

Mooring systems consist of several rope components. The longest rope part in the mooring line is the anchor line rope highlighted in figure 49. The main purpose of the anchor line rope is to decrease the weight of the system, making it easier to handle during maintenance and cheaper to install. The composition between the rope and bottom chain is highly dependent on the water depth at the location.

If the water depth is significant, which may especially be the case for deep Norwegian fjords and exposed fish farm locations, they will also provide restoring through elongation and elastic stiffness when the system is suspected to horizontal displacement. The anchor line rope component often consists of polypropylene or danline, which is made out of polypropylene and extruded polyethylene [6]. Polyester or nylon ropes may be used in some instances where higher elasticity is required, but can cause large problems in the mooring grid if the elasticity is not accounted for in the mooring analysis. Figure 51 illustrates rope made out of danline to the right and polypropylene to the left.

In addition to being an important part of the mooring line, ropes are used to connect different mooring lines into one complete system. This part is known as the mooring frame line and is also used to connect several fish pen‘s into one contiguous system. The bridle lines are used to connect the fish farm facility to the mooring frame line, transferring the forces induced by environmental conditions from the top side connection point to the mooring line itself. The main rope components are illustrated in figure 49.

The system evaluated in this paper uses polypropylene ropes of the Supertec 8 and Supertec 3 types. The mooring line component is made of supertec 8, which consists of 8 smaller diameter ropes braided together, to excel the strength properties of the material. The bridles and mooring frame lines are made of supertec 3, which has the same E-modulus as supertec 8, but is slightly weaker due to 3 braids opposed to its more robust supertec 8 counterpart [3].

Figure 51: Polyester rope to the left and Danline rope to the right [41] [42]

Shackles and connector plates

Shackles are used in many parts of the mooring system, primarily to connect the different components of the system including; mooring ropes, chains and anchors. They can be both omega-shaped of U shaped, where the omega-shaped option can accommodate more connections. The shackles have different strengths and properties according to their intended role, size of the structure and magnitude of the loads, and with regards to which components it connects. Figure 52 shows typical shackles used in marine environments of different shapes, dimension and strength.

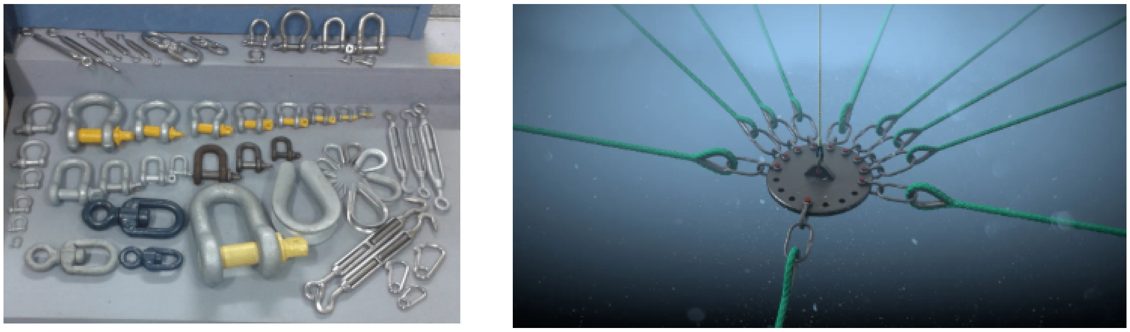

Figure 52: Connector plate and different shackle designs [39] [45]

Connector plates are used to connect the different main components of the mooring system and comes in many different shapes and sizes. As seen from figure 48 they are positioned in each corner of the grid system, connecting the grid mooring line, the mooring line itself and the bridles connecting the fish farm to the mooring line. To enable connection of the different components, the connector plate inhibits holes intended for connecting shackles all along the edge of the plate as illustrated in figure 52. In addition, to hinder abrasion between steel and rope components, every component connected to the plate is linked with either small parts of chain, or thimbles [5] (Chapter 3).

Buoys

There is a wide variety of buoys used in the aquaculture industry. As illustrated in figure 49 there is a small buoy connected to the connection point between the bottom chain and the mooring line rope. The intended role of these deep water buoys is to lift the connection point, hindering abrasion between components and the sea bottom. Abrasion can lead to increased fatigue in components, shorter lifespan and components collapsing before maintenance inspections.

The topside buoy is much larger than the deep water buoys, and has the intended role to create buoyancy to the mooring system. This is to lessen the strain on the topside connection point, by lifting the mooring line through buoyancy force. In addition, they work as markers for bypassing traffic and working vessels indicating the position of the connector plates and bridle connection points.

Their classes are decided by their size and buoyancy characteristics, which is simply decided by their displaced sea water volume minus the weight. The outside layer is often made out of polyethylene and the filling is usually polyurethane foam. Figure 53 shows a deep water and a topside buoy, attached to their different components in the mooring system [5] (Chapter 3).

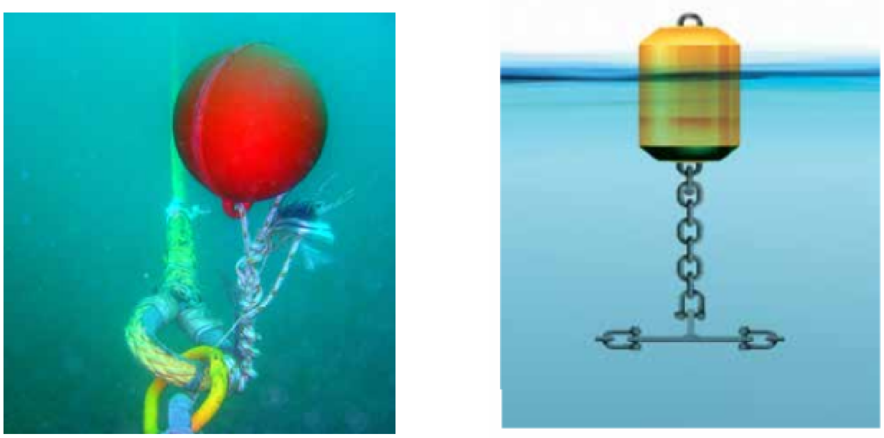

Figure 53: Deepwater buoy to the left and topside buoy to the right [**FAO1**] [17]

Anchors

The choice of anchor depends heavily on seabed conditions. If the seabed is soft in the form of mud or sand, plough anchors may be used. These types of anchors dig into the bottom when dragged along the seafloor and are the most commonly used solution for fish farm facilities. Figure 54 illustrates a typical Plough anchor. If the seabed is made out of rock or if the environment is unsuited for Plough anchors in any other way, dead weight or bolt anchors may be used. The dead weight anchor is solely based on gravity and must be dimensioned according to the forces affecting the system.

Figure 54: Dead weight concrete anchor solution to the left and plough anchor to the right [5] [28]

The bolt anchor is only applicable in locations where the bolt can get sufficient grip in the bottom material. They also have certain advantages, as they can absorb vertical forces when the entirety of the bottom chain is hanging freely in the water column. Figure 54 illustrates a typical dead weight anchor solution made out of concrete and a plow anchor made for the aquaculture industry.

3.2.2 Mooring line Stiffness and characteristics

Based on current fish farm technology, bathymetry and fish cage dimensions commonly used by the Norwegian aquaculture industry, this section describes the mooring line particulars used for the structural analysis. As discussed in section 1.3, the water depth at the CFFC location is assumed to be h = 100 meters, with a muddy/sandy bottom characteristic suited for plow anchors.

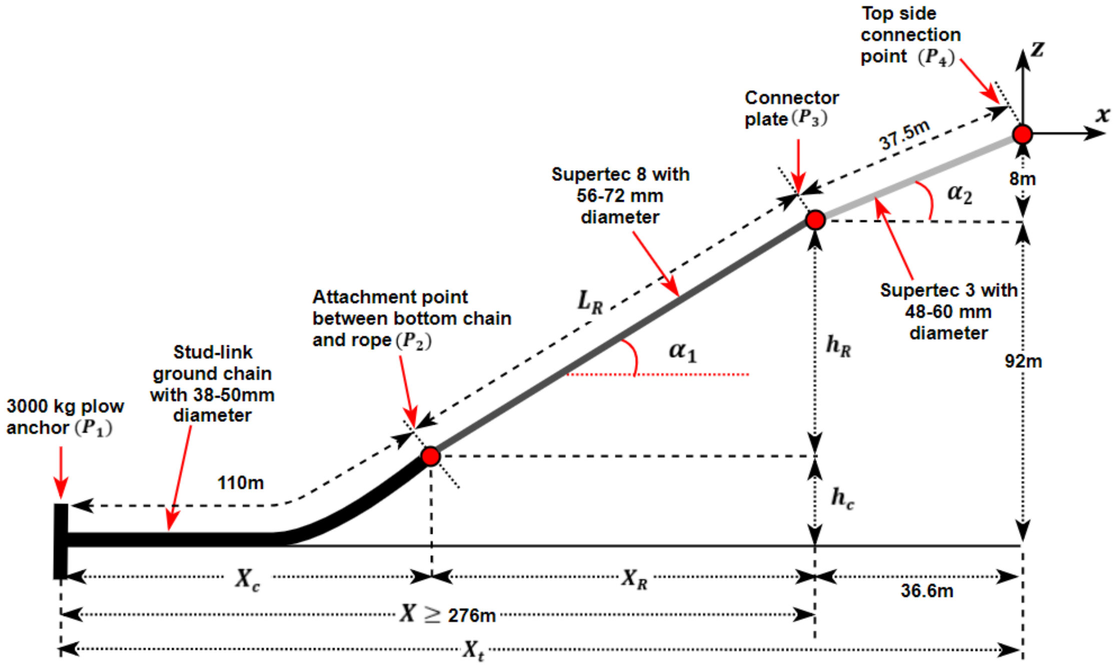

Figure 55: Mooring line particulars and notation used in the vertical plane

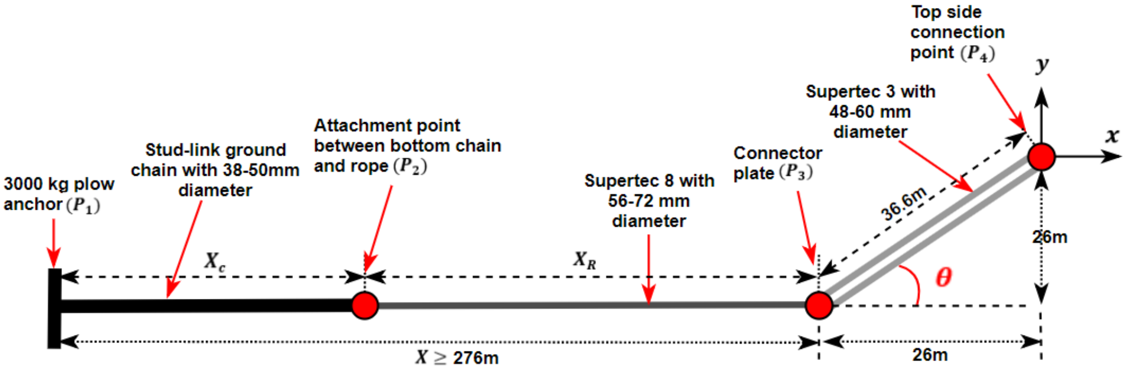

Figure 56: Mooring line particulars and notation used in the horizontal plane

Figure 55 and 56 represent a single mooring line in the vertical and horizontal plane respectively, its geometrical layout and notation used to define the mooring system in its pretensioned state. Throughout the analysis, the pretensioned state in the horizontal direction will be denoted as $T_{Hp}/T_{H\,pre}$, while the higher tension state will be denoted T_{Hh}. The layout and mechanical properties of the mooring lines are based on personal communication with Løvold AS, a company conducting mooring system analysis for the Norwegian aquaculture industry.

The vertical/horizontal ratio from the anchor to the connector plate (point P_1 to P_3) in figure 55 is 1/3 in the pretensioned state, which is a common industry standard [34]. This will be used as a criterion for the different mooring line layouts, meaning that the horizontal extension from the anchor to the connector plate has to be $\geq$ 276 meters assuming that the vertical distance from the connector plate to the sea bottom is 92 meters. In addition to the 1/3 ratio criterion, α_1 has to be the same as the angle (θ_T), formed by the inline tension of the ground chain and the horizontal axis in point P_2 illustrated in figure 24 and figure 55, expressed in equation 84. The relative angle in the horizontal plane $\theta = 45°$ represents the angle between the bridle lines and the x-axis. Based on the layout illustrated in figure 55 and 56.

Table 7 shows the mechanical properties including breaking strength, proof strength and weight properties for stud link chain grade U2 used for the CFFC mooring system. The submerged weight is calculated based on equation 86 and a steel density of ρ_{steel} = 8050 kg/m^3. The vertical/horizontal extension has been found through an iterative process of the vertical distance of the chain (h_c) in MATLAB using the catenary equation for the pretensioned state expressed in equation 81 and the equation for θ_T expressed in 84. This has been done to fulfill the 1/3 ratio criterion when the system is in its pretensioned state. The Table also shows the horizontal stiffness in surge direction (k_{11C}) for one continuous 110 meter stud link chain, linked by 4 industry standard individual links of 27.5 meters. In the Table, C_1, C_2 and C_3 denote the different chain layouts without the addition of clump weights, and C_4, C_5 and C_6 denote the same chain dimensions with the addition of clump weights to each individual link. When weight is added to the chain, 2000 kg is attached to each individual link of 27.5 meters, increasing the weight by 72.7 kg/m [3].

Bottom chain properties and characteristics							
Bottom chain ID		C_1	C_2	C_3	C_4	C_5	C_6
Chain diameter (∅)		38mm	42mm	50mm	38mm	42mm	50mm
Weight in air (W_a)	$[kg/m]$	32.3	39.4	56.2	105.1	112.1	128.9
Weight in water (W_w)	$[kg/m]$	28.2	34.4	49.0	91.7	97.8	112.5
Breaking load (MBL)	$[kN]$	812	981	1370	812	981	1370
Pretension (T_{Hp})	$[kg]$	3500	3500	3500	13000	13000	13000
horizontal layout (X_c)	$[m]$	108.0	108.3	108.8	107.9	108.1	108.4
Vertical layout (h_c)	$[m]$	13.0	11.0	8.0	14.0	13.0	11.0
In-line angle (θ_T)	[°]	25.2	25.5	26.0	24.5	24.4	24.1
Stiffness ($k_{11C\,pre}$)	$[N/m]$	1578	1890	2638	5314	5701	6660
High tension (T_{Hh})	$[kg]$	10000	10000	10000	30000	30000	30000
Stiffness ($k_{11C\,high}$)	$[N/m]$	2900	3480	4860	8646	9273	10832

Table 7: Bottom chain particulars and relative measurements according to Figure 55

The geometric stiffness in surge direction is estimated by using the expression for the surge direction stiffness derived from the catenary equation 85. The breaking load (MBL) is the maximum load before the link fails. The E-modulus is approximately 110 GPa for the steel alloy used in the link.

Figure 57 and 58 show the line characteristic for the different bottom chains.

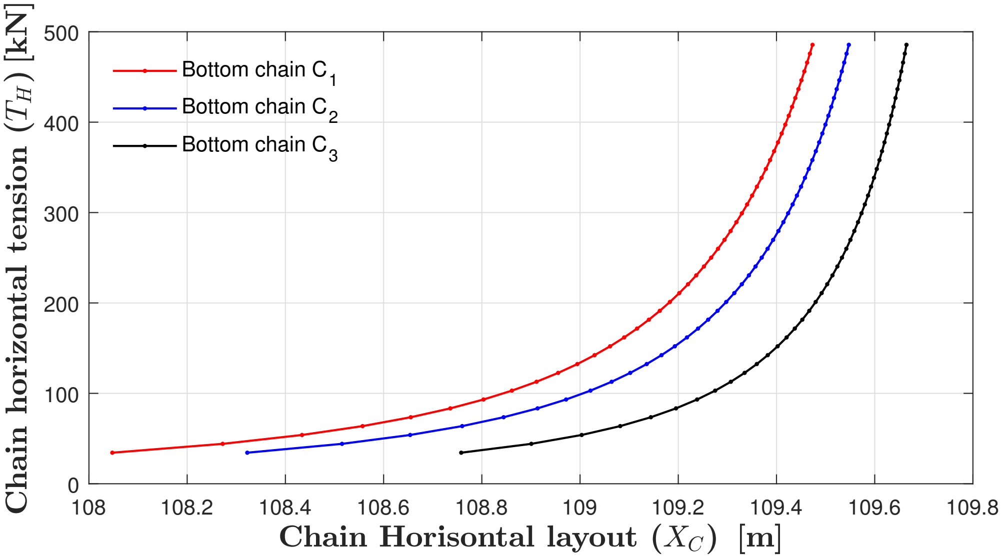

Figure 57: Line characteristic for the bottom chain C_1 C_2 C_3

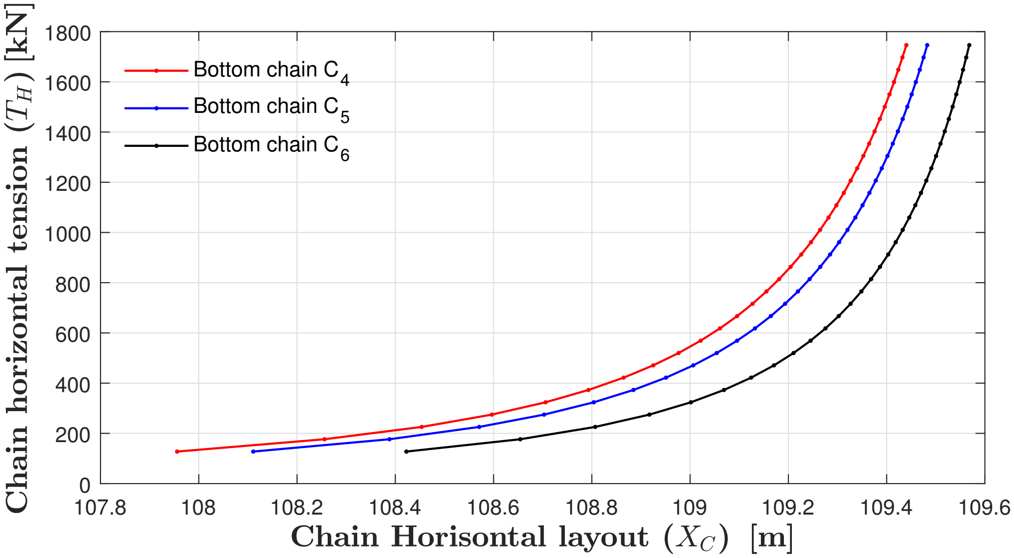

Figure 58: Line characteristic for the bottom chain C_4 C_5 C_6

From the curves, it is clear that the bottom chain stiffness is highly nonlinear. This means that the stiffness provided by the bottom chain varies to a large extent depending on the horizontal motion of the system. It is also worth noting that due to the limited water depth combined with the 1/3 horizontal/vertical criterion, the bottom chain has a rather large horizontal extension in the pretenisoned state. This can prove to be problematic if the horizontal motion from the WAMIT simulation and static analysis proves to be large. This is further discussed in section 5.

Based on the highly nonlinear line characteristic, two different stiffness coefficients have been calculated ($k_{11C\,pre}, k_{11C\,high}$) representing the chain when the system is in a pretensioned and higher tension state respectively. The different stiffness coefficients for the bottom chains are listed in table 7 and further used to evaluate the effect of modeling the bottom chain stiffness differently when running the simulation in WAMIT.

Table 8 shows the breaking strength, the proof strength and the weight properties of the supertec 8 polypropylene rope, for different dimensions used in the anchor line rope part of the mooring line. The angle between the horizontal axis and the mooring line rope (α_1) has been set equal to θ_T in the pretensioned state. Here, the chain configurations with identification C_1,...,C_N has been paired with the R_1,...,R_N anchor ropes respectively. This gives different configurations for the anchor rope component of the mooring line as seen from figure 55, where the vertical (L_R) and horizontal (X_R) layout depends on the bottom chain catenary shape and geometry.

Anchor line rope properties and characteristics							
Anchorline rope ID		R_1	R_2	R_3	R_4	R_5	R_6
Rope diameter (D_R)		56mm	64mm	72mm	56mm	64mm	72mm
Weight in air (W_a)	$[kg/100m]$	156.0	203.6	258.0	156.0	203.6	258.0
Cross section (A_R)	$[cm^2]$	24.63	31.26	40.71	24.63	31.26	40.71
E-modulus (E)	$[GPa]$	2.0	2.0	2.0	2.0	2.0	2.0
Breaking load (MBL)	$[kN]$	637	823	1034	637	823	1034
Pretension (T_{Hp})	$[kg]$	3500	3500	3500	13000	13000	13000
horizontal layout (X_R)	$[m]$	168.3	169.8	172.7	171.3	174.4	181.4
Vertical layout (h_R)	$[m]$	79.0	81.0	84.0	78.0	79.0	81.0
Lenght (L_R)	$[m]$	186.0	188.1	192.0	188.2	191.5	198.7
In-line angle (α_1)	[°]	25.2	25.5	26.0	24.5	24.4	24.1
Stiffness (k_{11R})	$[kN/m]$	21.71	27.86	34.30	21.67	27.88	34.17

Table 8: Anchor-line rope particulars and relative measurements according to figure 55

The elastic stiffness in surge direction is estimated from equation 77. This is under the assumption that the anchor line rope solely provides restoring through elastic stiffness to the system, which is appropriate due to the low weight in water. It is also under the assumption that α_1 is constant relative to the horizontal axis during elongation of the line.

Table 9 shows the properties of a single bridle line made of polypropylene supertec 3, connecting the top side connection point of the structure to the connector plate including 3 different dimensions. This part of the mooring system is outside the 1/3 vertical/horizontal layout criterion of the system and has the geometric layout highlighted in figure 55 and 56.

Bridle line properties and characteristics				
Bridle line ID		B_1	B_2	B_3
Rope diameter (D_B)		48mm	56mm	60mm
Cross section (A_B)	[cm^2]	18.09	24.64	28.27
Weight in air (W_a)	[$kg/100m$]	104.0	142.0	163.0
E-modulus (E)	[GPa]	2.0	2.0	2.0
Breaking load (MBL)	[kN]	416.9	543.5	613.1
Stiffness (k_{11B})	[kN/m]	46.05	62.7	71.20

Table 9: Bridle rope particulars and properties

The elastic stiffness in surge from one bridle line is calculated from equation 78. This is due to the layout of each individual bridle in the pretensioned state, forming an angle relative to the x-axis pointing in surge direction both in the vertical and horizontal plane.

The angle in the horizontal plane is $\theta = 45°$ relative to the x-axis, and the angle in the vertical plane relative to the x-axis is $\alpha_2 = 12.3°$ illustrated in figure 55. Here it is important to mention that the bridle lines are able to form å different angle α_2 compared to the mooring line rope angle α_1 due to the presence of the top side buoy supporting the connector plate (P_3). The bridle lines are suspected to assumptions and simplifications as the anchor line component.

Based on the physical parameters and the properties listed for the bottom chain, anchor line rope and bridle lines, six different mooring line configurations are listed in table 10. As highlighted through the previous paragraphs, the complete mooring lines have been adapted to fulfill the 1/3 ratio between vertical an horizontal layout meaning that $X \geq$ 276 meters in the pretensioned state, and that the angle forming in the top of the bottom chain (θ_T) is the same as the angle for the anchor line rope relative to the horizontal axis (α_1).

Each mooring line consists of one continuous bottom chain and an anchor line rope. In addition, each connector plate has 2 bridle lines connecting the plate to the top side connection point. This means that each pairing of one longitudinal and transverse mooring line shares two bridle lines included in the three different mooring line configurations.

It is important to highlight that the 8 mooring lines in each individual mooring system layout will consist of uniform mooring lines including the same dimensions and geometry. Different tests will be conducted for the six different mooring line configurations. This means that the different structures listed in section 3 will be paired with different mooring systems, depending on their size and mass.

Mooring line properties and characteristics							
Mooring line ID		M_1	M_2	M_3	M_4	M_5	M_6
Bottom chain ID		C_1	C_2	C_3	C_4	C_5	C_6
Anchorline rope ID		R_1	R_2	R_3	R_4	R_5	R_6
Bridle line ID		B_1	B_2	B_3	B_1	B_2	B_3
Pretension (T_{Hp})	$[kg]$	3500	3500	3500	13000	13000	13000
Horizontal layout (X)	$[m]$	276.3	278.1	281.5	279.3	282.5	289.8
Horizontal layout (X_t)	$[m]$	312.9	314.7	318.1	315.9	319.1	326.4
Line Stiffness ($k_{11\,Mp}$)	$[kN/m]$	1.38	1.67	2.30	3.60	4.11	4.82
System Stiffness ($K_{11\,p}$)	$[kN/m]$	5.53	6.70	9.17	14.40	16.45	19.30
High tension (T_{Hh})	$[kg]$	10000	10000	10000	30000	30000	30000
Line Stiffness ($k_{11\,Mh}$)	$[kN/m]$	2.31	2.82	3.81	4.87	5.70	6.70
System Stiffness ($K_{11\,h}$)	$[N/m]$	9.22	11.26	15.23	19.49	22.78	26.78

Table 10: Mooring line particulars and relative measurements according to figure 55

The total stiffness in surge for each mooring line configuration is calculated using equation 72, adding one contribution from the chain (k_{11C}), one contribution from the anchor line rope (k_{11R}) and two contributions from the bridle lines (k_{11B}). This gives the total stiffness for one individual mooring line (k_{11M}). Due to the nonlinear characteristic of the bottom chain, the total stiffness for the mooring line and complete system has been calculated for two different tension states for the bottom chain, as highlighted in table 7.

It is important to emphasize that the pretension and high-tension state of the bottom chain stiffness, $k_{11C\,pre}$ and $k_{11C\,high}$, has been combined with the pretensioned stiffness for the anchor (k_{11R}) and bridle line rope (k_{11B}) in both instances. This is due to very small differences in elastic stiffness as the angle between the mooring line and horizontal axis changes.

The total mooring system stiffness in surge (K_{11}) is calculated from equation 87 and 88 using the orientation illustrated in figure 26. Due to the layout of the orthogonal system, the stiffness in surge is the same as the stiffness in sway, when modeling the stiffness matrix in WAMIT. Modifications with respect to heading angle concerning different lines contributing to the stiffness when the system gets suspected to environmental forces is accounted for by the WAMIT software.

The line characteristics for the six different mooring lines used in WAMIT stiffness matrix is plotted in MATLAB using the constant mooring line stiffness (k_{11M}) listed in table 10. The characteristic shows the correlation between horizontal displacement and top side tension when the system gets affected by environmental forces from waves and current.

In addition to assuming that the bottom chain stiffness can be modeled as a constant in the pretensioned state, the anchor line rope and bridles are also modeled according to the simplification that the angle α_1, α_2 is constant when the system moves.

Figure 59 and 60 shows the linear line characteristic for M_1, M_2 and M_3 when the bottom chain stiffness is taken at T_{Hp} = 3500 kg and T_{Hh} = 100000 kg respectively.

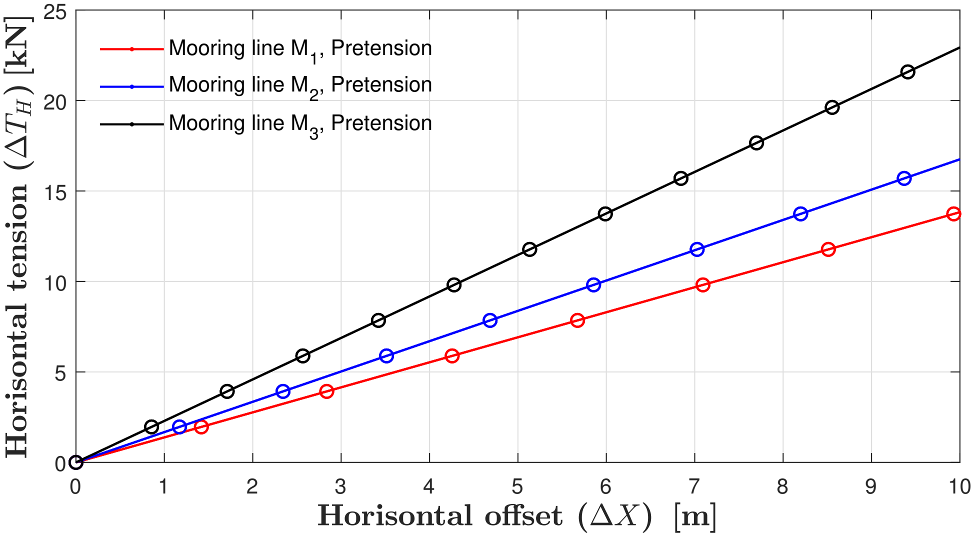

Figure 59: Line characteristic for mooring lines with bottom chain stiffness at T_{Hp} = 3500kg

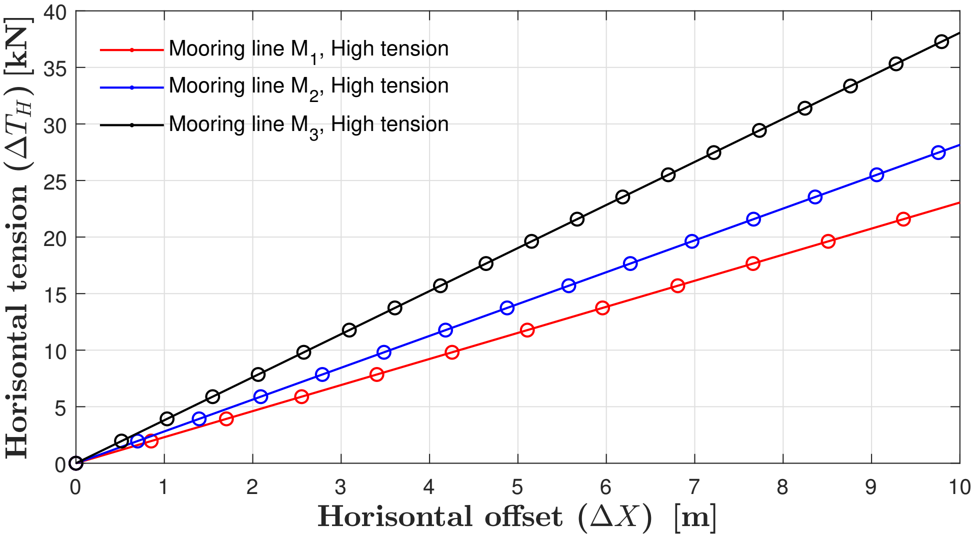

Figure 60: Line characteristic for mooring lines with bottom chain stiffness at T_{Hh} = 10000kg

Figure 59 and 60 shows the linear line characteristic for M_4, M_5 and M_6 when the bottom chain stiffness is taken at T_{Hp} = 13000kg and T_{Hh} = 30000kg respectively.

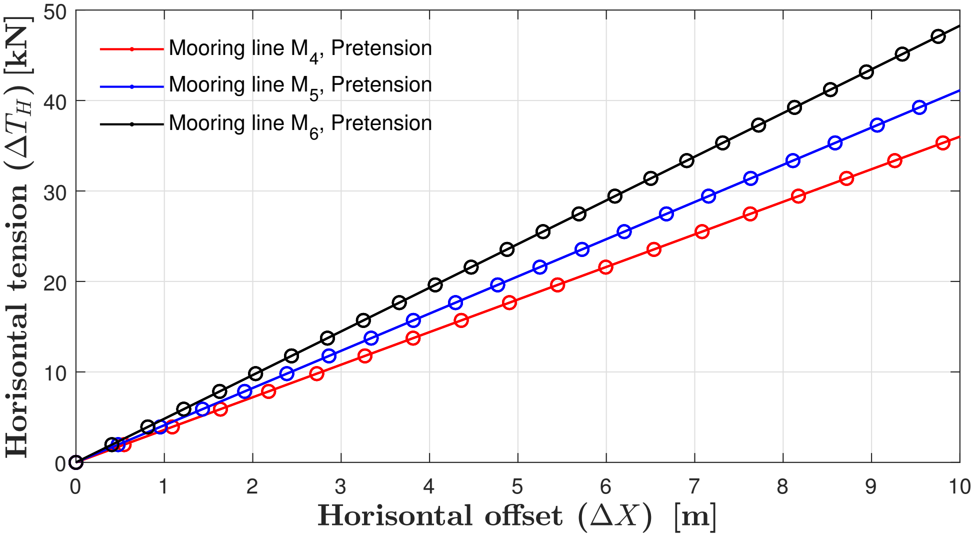

Figure 61: Line characteristic for mooring lines with bottom chain stiffness at T_{Hp} = 13000kg

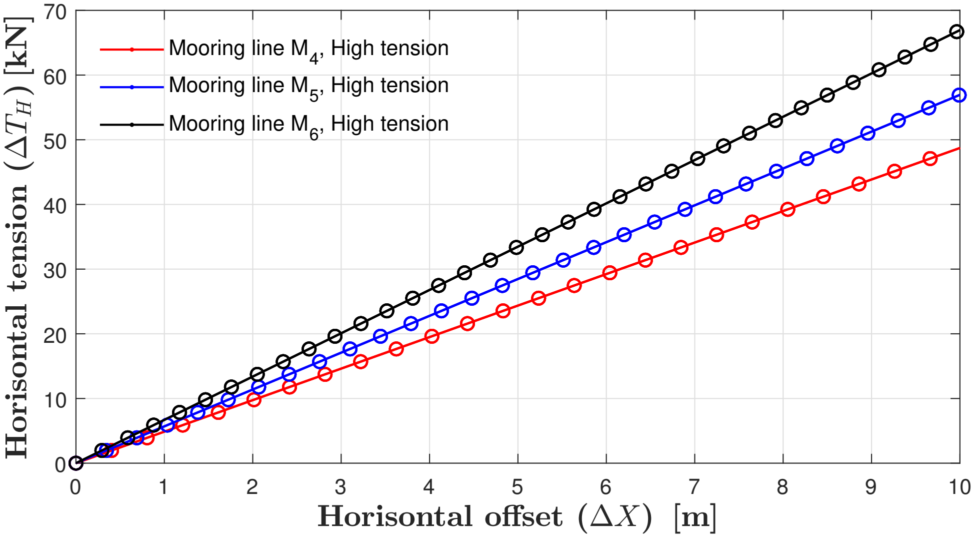

Figure 62: Line characteristic for mooring lines with bottom chain stiffness at T_{Hh} = 30000kg

3.3 Damping effects

This section highlights the damping effects outside potential damping limited to surge and sway motion. As WAMIT accounts for the potential damping through the coefficients included in the B matrix, other effects are included by the user in the user-specified damping matrix. In this paper, this is done by evaluating data from an experimental decay test conducted by SINTEF Ocean in the SJØFLO project [8]. The decay test is used to find reasonable values when accounting for viscous damping effects.

The decay test was performed for a cylindrical model which is different from the spherical and semi ellipsoid shaped design investigated in this paper mainly due to the draft and shape of the structure in the vertical plane. However, the top side diameter of the two structures in full scale is the same. Due to the deviations in shape, the damping coefficients from the decay test must be handled with care. The difference in shape from the decay test model and the CFFC structures investigated in this paper is illustrated in figure 63 for the full scale structures.

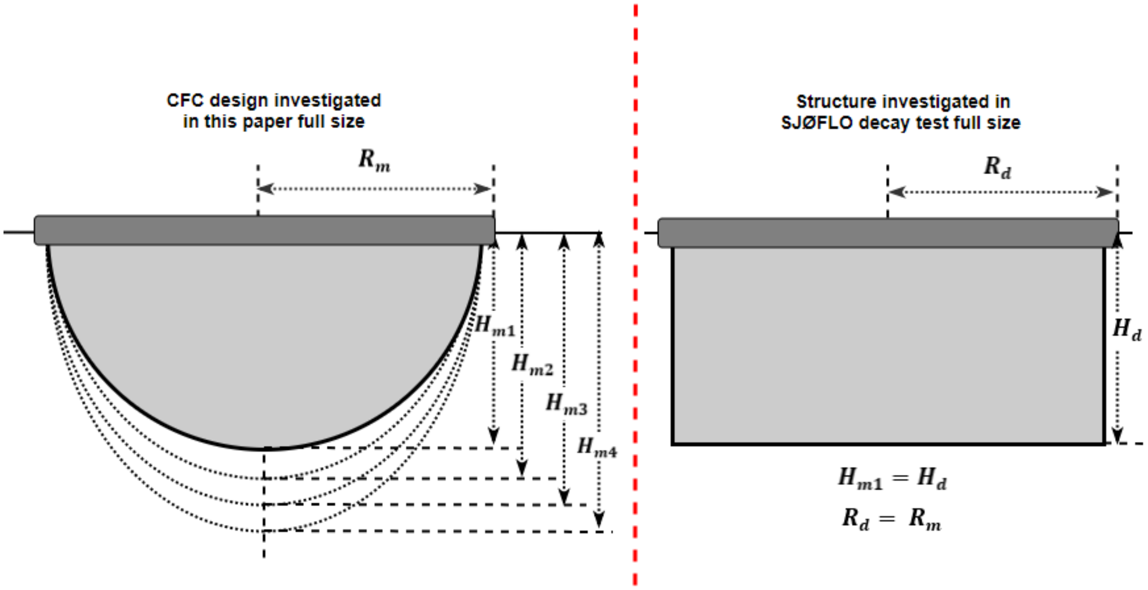

Figure 63: Comparison between the decay test design and the designs evaluated in this paper

The smooth surface of the CFFC and assumed to be small KC number, makes it even more important that the added damping effects is not overestimated. To make sure that this doesn't happen, the coefficient is compared to the critical damping of all four designs. This makes it possible to use the critical damping in combination with the decay test to qualitatively estimate a realistic percentage of the critical damping, that can be added to the user-specified damping matrix in WAMIT. The eigenperiod of the cylindrical model scaled system in the decay test was T_m = 22.3 seconds, the radius R_d = 0.75 meters and drought $H_d = R_d$ [8]. Figure 64 shows the decay test performed for the cylindrical design by SINTEF Ocean. The test was performed in the testing facilities at SINTEF in Trondheim, Norway, in model scale with Froude scaling factor λ_f = 27 representing the ratio between the full and model scale facility. The figures containing the p_1 and p_2 coefficients was provided by David Kristiansen, Senior Scientist at SINTEF Ocean.

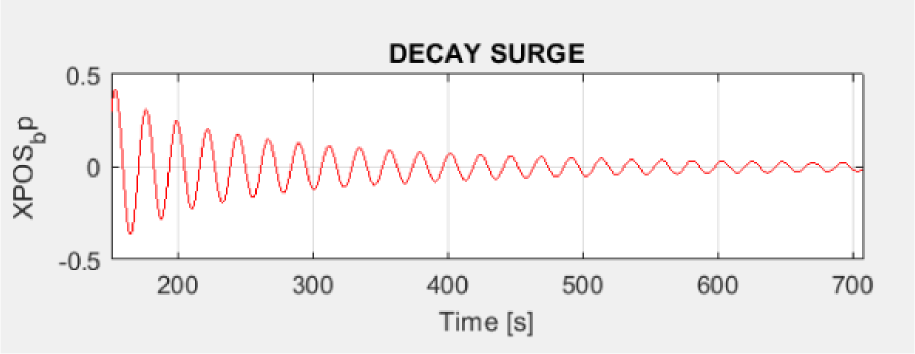

Figure 64: Decay test from the *SJØFLO* project [8]

From the decay test the damping coefficients (p_1 and p_2) was found by using the least square method and the logarithmic decrement highlighted in section 2.3.6. Figure 65 shows the plot found by solving the left and right hand side og Equation 17 including estimates for $p_1 = B_{lin}/(M_{11}+A_{11})$ and $p_2 = B_{qd}/(M_{11}+A_{11})$.

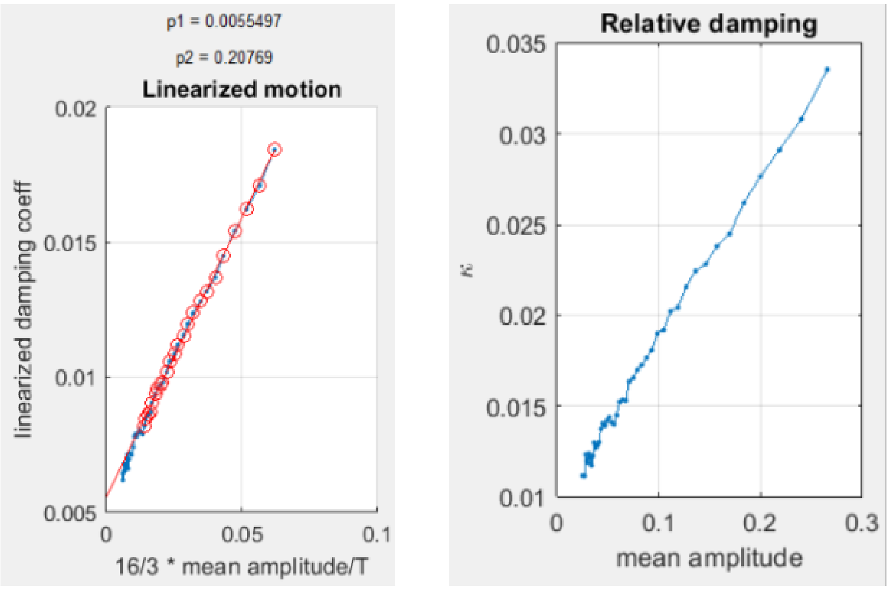

Figure 65: Plot for finding the damping coefficients $\boldsymbol{p_1}$ and $\boldsymbol{p_2}$ and the relative damping [8]

It is crucial to emphasize that the coefficients in figure 65 represent results from the cylindrical model scale structure and not the full-scale coefficients. Using the Froude scaling factor used in the SJØFLO investigation, the full-scale diameter of the cylindrical structure becomes R_d = 40 meters. This is the same as the diameter of the structures investigated in this paper, which means that λ_f = 27 applies when using p_1 and p_2.

Using equation 55 the total linear damping for the four different designs can be estimated. As p_1 represents the model scale coefficient from the decay test, the mass including water filling (M_{11}) and added mass (A_{11}) for the four different designs has to be scaled to model size using $(\lambda_f)^3$. The potential damping and added mass were estimated in WAMIT for the full-size structures at T_m = 116 seconds equivalent to T_m = 22.3 seconds for model scale using Froude scaling. This was done without accounting for the motion of the internal water mass, modeling the mass as a solid within the structure.

As specified in section 2.6 the damping coefficient scales with $(\lambda_f)^{2.5}$ from model to full scale. Table 11 shows the different model and full-scale linear damping coefficients when using data from the decay test ($B_{11\,lin}$), the linear damping contribution to the user-specified damping matrix found from equation 56, mass including the internal water mass and added mass.

Linear damping coefficients					
Design number		Design (D_1)	Design (D_2)	Design (D_3)	Design (D_4)
Model size data					
Added mass (A_{11})	$[kg]$	437	582	656	734
Mass (M_{11})	$[kg]$	873	1005	1130	1220
linear damping ($B_{11\,lin}$)	$[kg/s]$	7.28	9.01	9.96	10.9
Potential damping (B_{11})	$[kg/s]$	$0.31 \cdot 10^{-3}$	$0.49 \cdot 10^{-3}$	$0.59 \cdot 10^{-3}$	$0.71 \cdot 10^{-3}$
Full size data					
Mass (M_{11})	$[kg]$	$1.72 \cdot 10^7$	$2.07 \cdot 10^7$	$2.24 \cdot 10^7$	$2.41 \cdot 10^7$
Added mass (A_{11})	$[kg]$	$0.86 \cdot 10^6$	$1.14 \cdot 10^7$	$1.29 \cdot 10^7$	$1.44 \cdot 10^7$
linear damping ($B_{11\,lin}$)	$[kg/s]$	$2.75 \cdot 10^4$	$3.44 \cdot 10^4$	$3.77 \cdot 10^4$	$4.11 \cdot 10^4$
Potential damping (B_{11})	$[kg/s]$	1.20	1.86	2.26	2.69
Added linear (${B_{11}}^{(1)}$)	$[kg/s]$	$2.75 \cdot 10^4$	$3.43 \cdot 10^4$	$3.77 \cdot 10^4$	$4.11 \cdot 10^4$

Table 11: Full and model scale potential and linear damping coefficients

To find reasonable estimates for the linearized quadratic damping coefficient (${B_{11}}^{(2)}$) the decay test in figure 64 was used in combination with the p_2 coefficient from figure 65. This was done with respect to the physical meaning of the quadratic damping, which is dependent on the oscillation amplitude of the system.

As the matrix added by the user in WAMIT contains a constant value for the damping, equation 65 was used in combination with the decay test to find an upper and lower value for the model scaled linearized quadratic damping coefficient. The upper and lower value is based on two different values for the oscillation amplitude in the decay test. The upper value, ${\eta_{A1}}^{(H)}$ = 0.3 meters was chosen at the start of the test when the amplitude was large, while the lower value, ${\eta_{A1}}^{(L)}$ = 0.01 meters was chosen at the end of the test when the amplitude was small.

Table 12 shows the parameters including the linearized damping coefficient used for the four designs investigated in this paper. It also shows the upper and lower coefficient based on the amplitude of oscillation from the decay test in figure 64, calculated from equation 65. These two coefficients were used to find a respectable linearized damping coefficient for model scale (${B_{11.mod}}^{(2)}$). This was simply done by taking the mean value of the coefficient in the upper and lower part of the decay test. The mass and added mass for the four different structures are listed in table 11, both for the full scale and model scaled structure.

The table also includes the total damping ${B_{11}}^{(e)}$ = ${B_{11}}^{(1)}$ + ${B_{11}}^{(2)}$ and the added mass for T_∞ used to calculate the critical damping. The added mass for T_∞ was found from simulations in WAMIT for the four different structures. The total damping added to the user-specified matrix has been calculated from table 11 and 12. As for the linear damping coefficient, the full scale linearized damping coefficient has been found from using the Froude scaling factor.

Linearized quadratic damping coefficients					
Design number		Design (D_1)	Design (D_2)	Design (D_3)	Design (D_4)
Model size data					
Low damping (${B_{11(L)}}^{(2)}$)	$[kg/s]$	3.83	4.78	45.25	5.73
High damping (${B_{11(H)}}^{(2)}$)	$[kg/s]$	23.02	28.70	31.50	34.40
Avarage damp. (${B_{11.mod}}^{(2)}$)	$[kg/s]$	13.43	16.73	18.37	20.06
Full size data					
Added quadratic (${B_{11}}^{(2)}$)	$[kg/s]$	$5.09 \cdot 10^4$	$6.34 \cdot 10^4$	$6.96 \cdot 10^4$	$7.60 \cdot 10^4$
Total damping (${B_{11}}^{(e)}$)	$[kg/s]$	$0.78 \cdot 10^5$	$0.98 \cdot 10^5$	$1.07 \cdot 10^5$	$1.17 \cdot 10^5$
Added mass at T_∞	$[kg]$	$0.86 \cdot 10^7$	$1.14 \cdot 10^7$	$1.29 \cdot 10^7$	$1.45 \cdot 10^7$

Table 12: Full and model scale quadratic damping coefficients

The critical damping and damping ratio is included for all the different combinations between mooring systems and design in Appendix A. Here, the critical damping is estimated from equation 68 in surge for the system when suspected to oscillation with period T_∞.

The critical damping in surge is calculated based on the horizontal stiffness in surge (K_{11}), created by the different mooring systems and the total mass of the system ($M_{11} + A_{11}$). The stiffness is taken in the pretensioned state and higher tension state of the mooring system listed in table 10. In addition, based on the critical damping and the actual damping from the decay test, the damping ratio (ζ) has been calculated from equation 69. The damping parameters, including the damping ratio has been estimated for all four designs in MATLAB, when kept in place by the six different mooring systems with parameters highlighted in table 10.

The results for the damping ratio indicate that using the decay test, the damping ratio roughly varies between 5 to 13 $\%$. As the system investigated in this paper is limited to a maximum exposure of T_p = 6.7 seconds, the decay test has to be used with care. Looking at the definition of the KC number, it is evident that the large oscillation period of the system in the decay test equivalent to T_m = 116 seconds in full scale, compared to the lower oscillation regime in the frequency domain could lead to very different viscous damping effects.

Also, due to the presence of sharp corners and edges on the cylindrical design compared to the hemispherical and semi ellipsoid geometries in this paper, the viscous damping effect could be significantly larger for the cylindrical design. On the other hand, damping effects from vortex shedding in and around the mooring lines and mooring components has not been accounted for, which can be considerable. From the evaluation of the decay test, the KC number, the difference in geometry, the damping ratio (ζ), the nature of the first-order motion and the lack of added damping from mooring system components, damping from viscous effects and linear effects outside potential damping is modeled as 10% of the critical damping when running the WAMIT simulations.

4 Test conditions and systems suspected to testing

4.1 System testing in WAMIT

Table 13 shows the different systems suspected to testing in the dynamic and static wave analysis in WAMIT. The systems are decided according to the design and the mooring system used for stationkeeping. The table also includes the eigenperiod of the systems in surge when the bottom chain stiffness is taken in the pretensioned (T_{Hp}) and the high tension state (T_{Hh}) respectively, calculated from equation 101.

Systems suspected to testing				
	System ID	Design ID	Mooring ID	Eigenperiod $\boldsymbol{T_{n1}}[\boldsymbol{s}]$
System 1	SY_1	D_1	M_1	429, 332
System 2	SY_2	D_2	M_3	372, 288
System 3	SY_3	D_3	M_5	291, 247
System 4	SY_4	D_4	M_6	280, 238
System 5	SY_5	D_1	M_4	265, 228
System 6	SY_6	D_2	M_5	277, 236
System 7	SY_7	D_3	M_6	269, 228

Table 13: Systems suspected to testing in dynamic and static analysis in WAMIT

Table 14 shows the different tests carried out in WAMIT for the different systems highlighted in table 13. The table also highlights the main parameters added to the user-specified stiffness and damping matrix, if the test is with or without a free surface, the heading angle and the maximum wave period (T_{max}). Due to the symmetrical geometry of the structure and the layout of the mooring system, the critical damping in surge and sway is the same, meaning that $B_{11}^{cr} = B_{22}^{cr}$ can be used when modeling damping effects for the horizontal motion. The same goes for the stiffness modeled in the stiffness matrix as $K_{11} = K_{22}$ due to the orthogonal layout of the mooring system. All parameters for the mooring system stiffness and critical damping for the different combinations of mooring systems and designs are listed in table 10 - 12 and in Appendix A. All tests are performed for regular waves with varying wave periods, depending on the purpose of the test.

The mass and inertia is listed for all the structures excluded water mass in table 6. When the water mass is modeled as a solid within the structure, the user-specified mass and inertia matrix is modeled accordingly, with the full-size mass and inertia including that of the internal water mass. Here, the inertia is estimated based on standardized equations from [30] by Jack.A.Myers.

Test $1-7$ highlights different combinations between mooring systems and designs denoted as system $1-7$ in table 13. These tests are used directly in the mooring system analysis in section 5.3. The combinations between designs and mooring systems have been chosen according to the size of the CFFC structure and the linear stiffness coefficient of the mooring system. In test $1-4$ the smallest designs (D_1 and D_2) has been combined with the mooring systems with smallest dimensions, and the largest designs (D_3 and D_4) with the mooring systems with large dimensions. In test $5-7$ the D_1, D_2 and D_3 is combined with more robust mooring systems.

Test 8 and 9 illustrate the effect of the free surface and its effect on the RAO's in Surge for system 2 and 4. Test 10 to 13 which has the purpose of highlighting the eigenperiod of system $1-4$ in surge has been conducted both when the stiffness of the mooring systems are modeled in the pretension and high tension state.

This is to see how the eigenperiod changes when the nonlinear stiffness for the bottom chain is modeled differently. Test 14 illustrates the difference in RAO when the bottom chain of the mooring line is modeled in a higher tensioned state for the relevant wave periods limited to high exposure.

Different tests for WAMIT simulation						
Test ID	System ID	Stiff. $C_{11}^{(e)}$	Damp. $B_{11}^{(e)}$	T_{max} $[s]$	Heading β	Free surface
Test 1	SY_1	K_{11p}	$0.1 \cdot B_{cr}$	15 , 60	0°	Yes
Test 2	SY_2	K_{11p}	$0.1 \cdot B_{cr}$	15 , 60	0°	Yes
Test 3	SY_3	K_{11p}	$0.1 \cdot B_{cr}$	15 , 60	0°	Yes
Test 4	SY_4	K_{11p}	$0.1 \cdot B_{cr}$	15 , 60	0°	Yes
Test 5	SY_5	K_{11p}	$0.1 \cdot B_{cr}$	15 , 60	0°	Yes
Test 6	SY_6	K_{11p}	$0.1 \cdot B_{cr}$	15 , 60	0°	Yes
Test 7	SY_7	K_{11p}	$0.1 \cdot B_{cr}$	15 , 60	0°	Yes
Test 8	SY_2	K_{11p}	$0.1 \cdot B_{cr}$	7	0°	Both
Test 9	SY_4	K_{11p}	$0.1 \cdot B_{cr}$	7	0°	Both
Test 10	SY_1	K_{11p} , K_{11h}	$0.1 \cdot B_{cr}$	600	0°	No
Test 11	SY_2	K_{11p} , K_{11h}	$0.1 \cdot B_{cr}$	600	0°	No
Test 12	SY_3	K_{11p} , K_{11h}	$0.1 \cdot B_{cr}$	600	0°	No
Test 13	SY_4	K_{11p} , K_{11h}	$0.1 \cdot B_{cr}$	600	0°	No
Test 14	SY_4	K_{11p} , K_{11h}	$0.1 \cdot B_{cr}$	20	0°	Yes
Test 15	SY_4	K_{11p}	$0.1 \cdot B_{cr}$	20	0, 30, 45 °	Yes
Test 16	SY_3	K_{11p}	$0.1 \cdot B_{cr}$	20	0, 30, 45 °	Yes

Table 14: Different tests conducted in WAMIT

In test $10-13$ the internal water mass is modeled as a solid within the structure when investigating the eigenperiod of the system, neglecting the free surface effect. This had to be done due to computational limits when running a large span of wave periods $T \in [0, 600]$ seconds. Test $15-16$ is carried out to investigate the effect of the heading angle, used further when evaluating if other than $\beta = 0°$ heading angles has to be considered in the mooring system analysis.

4.2 Irregular sea states

Table 15 shows the different irregular sea states used in combination with the RAO's from the frequency domain analysis in WAMIT, and when estimating the total mean drift force. The sea states has been chosen randomly for $T_p \in$ [2.0, 6.7] seconds and $H_s \in$ [0.5, 3.0] meters. The table also shows different parameters such as the zero upcrossing period (T_z) for the different sea states used to find the total number of waves (N_w) estimated from equation 120. All sea states are measured over a duration of t = 10800 seconds, equivalent to 3 hours.

Irregular Sea-states and wave conditions							
Sea state ID	T_P $[s]$	H_s $[s]$	T_z $[s]$	$S(\omega)_m$ $[\frac{m^2}{rad/s}]$	ζ_A $[m]$	ζ_{max} $[m]$	N_w
$\boldsymbol{ST_1}$	2.0	0.5	1.42	0.007	0 - 0.05	0.37	7586
$\boldsymbol{ST_2}$	3.0	1.0	2.13	0.043	0 - 0.08	0.78	5057
$\boldsymbol{ST_3}$	4.0	1.5	2.84	0.128	0 - 0.10	1.23	3792
$\boldsymbol{ST_4}$	5.0	2.0	3.56	0.285	0 - 0.13	1.71	3034
$\boldsymbol{ST_5}$	6.0	2.5	4.27	0.534	0 - 0.14	2.18	2529
$\boldsymbol{ST_6}$	6.7	3.0	4.77	0.860	0 - 0.16	2.76	2264

Table 15: Irregular sea states utilized to obtained results from static and dynamic analysis

The wave amplitudes for the different regular waves in the sea state, taken at steps of ($\Delta\omega$) is calculated from equation 121, while the maximum amplitude is decided from plotting the wave elevation in MATLAB. Figure 66 shows the wave elevation as function of time for t = 3 hours, for the maximum sea state (ST_6) limited by high wave exposure.

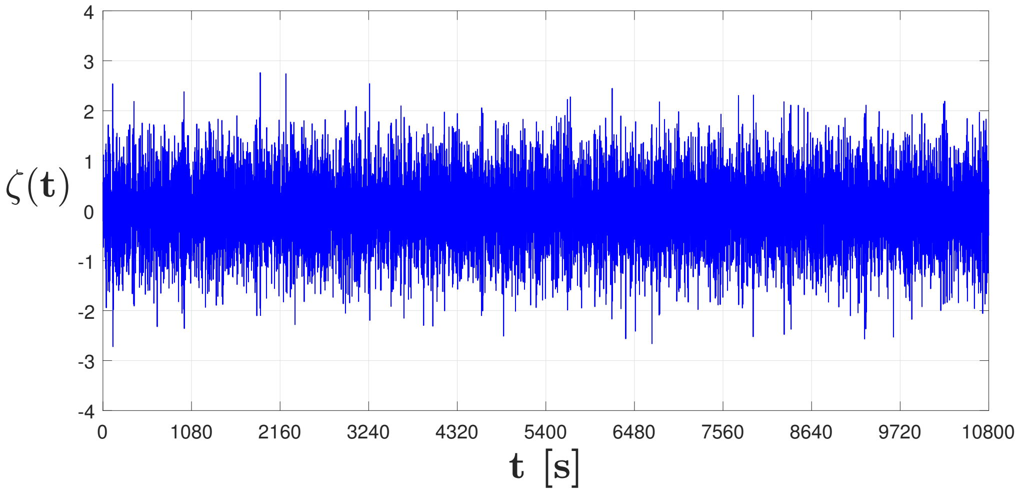

Figure 66: Sea state 6 surface elevation

5 Results and discussions

This section involves the results from the dynamic analysis in WAMIT and the static analysis including mean drift forces and forces from current. Based on the static and dynamic analysis, the mooring system is analyzed from the total force exerted on one mooring line by environmental forces ($F_{x\,tot}$).

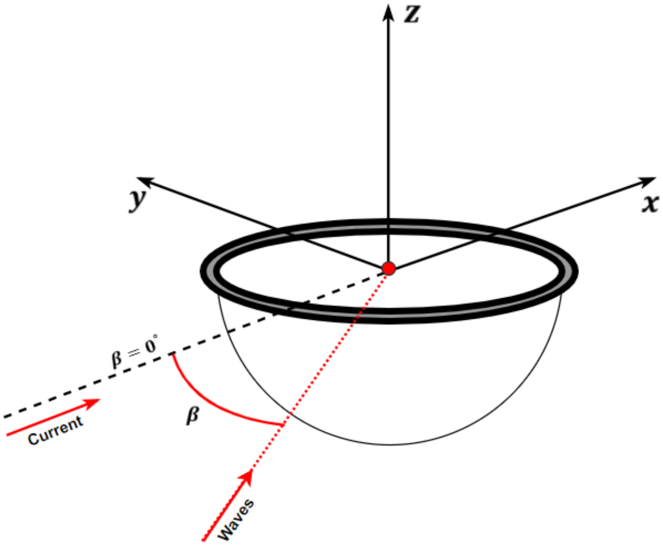

Figure 67: Orientation and illustration of Current and wave direction

The dynamic analysis is based on RAO's, used in combination with a PM-spectrum to obtain the most probable maximum dynamic offset of the systems. From this, the equivalent dynamic force is found from the mooring system stiffness.

The static analysis is based on transfer functions in form of nondimensional mean drift forces coefficients from WAMIT, calculating the total drift force by combining the coefficients with regular wave component in the PM-spectrum, and by manual estimation of the current force using MATLAB and Morison's equation. The MATLAB code used when estimating the dynamic offset and static force are included in Appendix C,D and E.

Based on the results from the static and dynamic analysis, the mooring system is evaluated according to NS9415. The mooring lines are evaluated according to their breaking strength (MBL) listed in section 3.2. In addition, the layout of the bottom chain is evaluated to see if vertical forces on the anchor have the ability to compromise the integrity of the system, and the rope components with respect to its ability to elongate. Discussion regarding the different results are carried out after the dynamic and static analysis respectively, and in the end of the mooring system analysis.

5.1 Dynamic analysis

The numerical wave analysis in WAMIT are subject to the different test conditions listed in table 14. The following results include different setups, where the different designs highlighted in table 6 is paired with the different mooring systems in table 10. The systems consisting of designs and mooring systems are listed in table 13.

Test 1−7 has been performed for Δ T = 0.1 representing the different wave periods for $T \in$ [0, 15] seconds. The tests has also been performed for $T \in$ [0, 60] seconds with ΔT = 0.5. Test 8−9 has been performed for $T \in$ [0, 7] seconds with Δ T = 0.05. Test 10−13 is suspected to a much wider set of regular waves $T \in$ [0, 600] seconds, with ΔT = 3. Test 13 is suspected to $T \in$ [0, 100] seconds with Δ T = 0.5.

Test 1 through 14 has been tested for β = 0 heading angle, as defined in figure 26, while Test 15 and 16 has been suspected to three different heading angles β = 0°, 30°, 45°.

Due to the purpose of investigating CFFC mooring system integrity, the motion and forces have been investigated with respect to surge motion in the horizontal plane, emphasizing on test 1−7 representing the different systems further used in the mooring system analysis. The RAO in heave motion for test 1−4 is also listed primarily to confirm that the results from the analysis give realistic results.

When investigating the eigenperiod of the system, the difference when modeling the stiffness differently and the effect of the heading angle, only the RAO's showing important results have been emphasized. This means that if several system's show the same behavior with minor differences, a selection of RAO's is presented to highlight the important parameters and confirm the system behavior.

All tests have been performed when the geometry of the structure is represented by a constant number of panels, using the low order panel method in WAMIT. Both the membrane and internal tank is represented by 1680 panels, and the floating collar by 86 panels.

As for the wave periods, this was decided according to time available and computing power. Several tests was also performed when the body was divided into a finer mesh of panels. These tests often had the tendency to fail when approaching the end of the test, leading to the decision to lower the number of panels. However, the tests with a higher number of panels that didn't fail towards the end showed that the results where close to identical to the tests performed with a lower number of panels.

The direct solver used in the simulation when running the POT file is based on standard Gauss reduction with partial pivoting when solving the potential problem, further discussed in section 3. This solver had to be used due to problems with the iterative solver for low wave periods. When solving for the forces, both the direct and iterative solver was used. Here, the direct solver had to be used in instances when the iterative solver failed to converge.

5.1.1 RAO's from dynamic analysis in WAMIT

Surge motion dynamic analysis

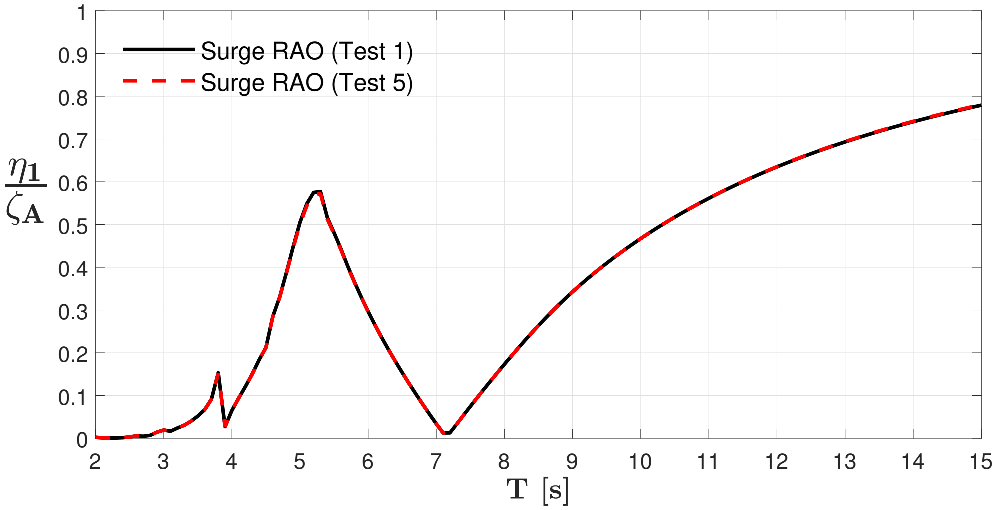

Figure 68: Response Amplitude operator in surge for System 1 *(Test 1)* and System 5 *(Test 5)*

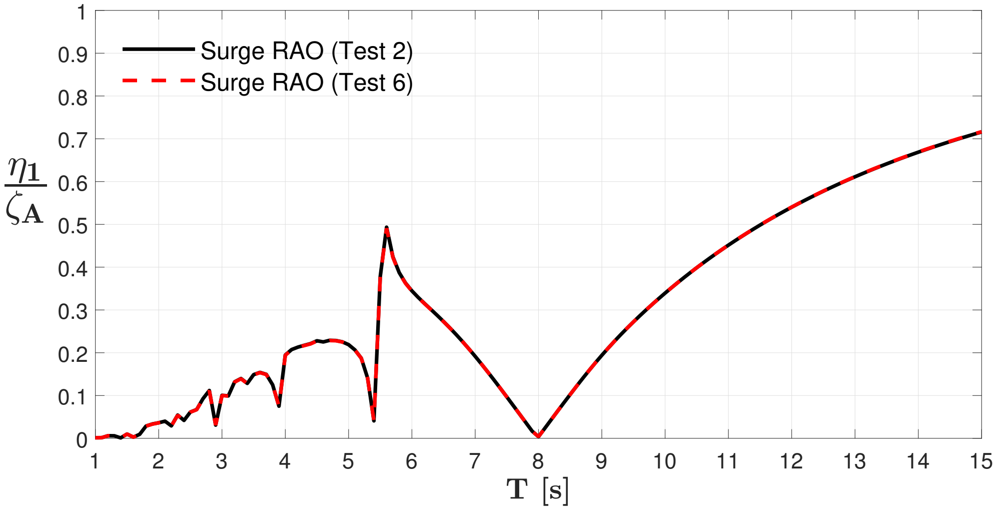

Figure 69: Response Amplitude operator in surge for System 2 *(Test 2)* and System 6 *(Test 6)*

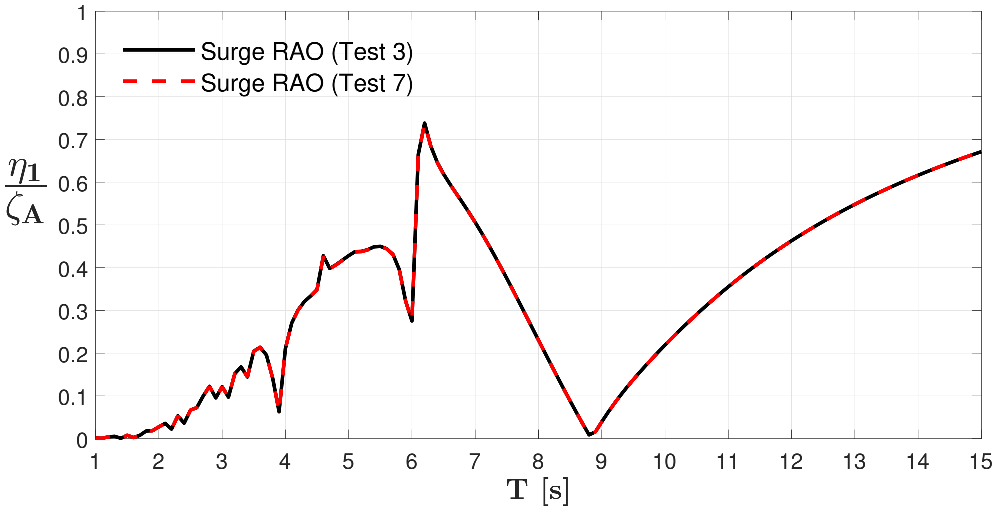

Figure 70: Response Amplitude operator in surge for System 3 *(Test 3)* and System 7 *(Test 7)*

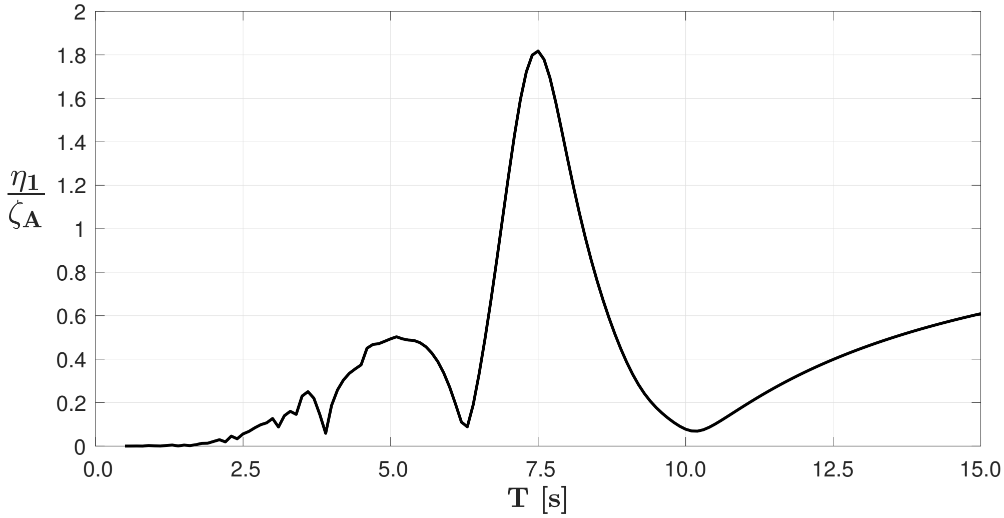

Figure 71: Response Amplitude operator in surge for System 4 *(Test 4)*

Heave motion dynamic analysis

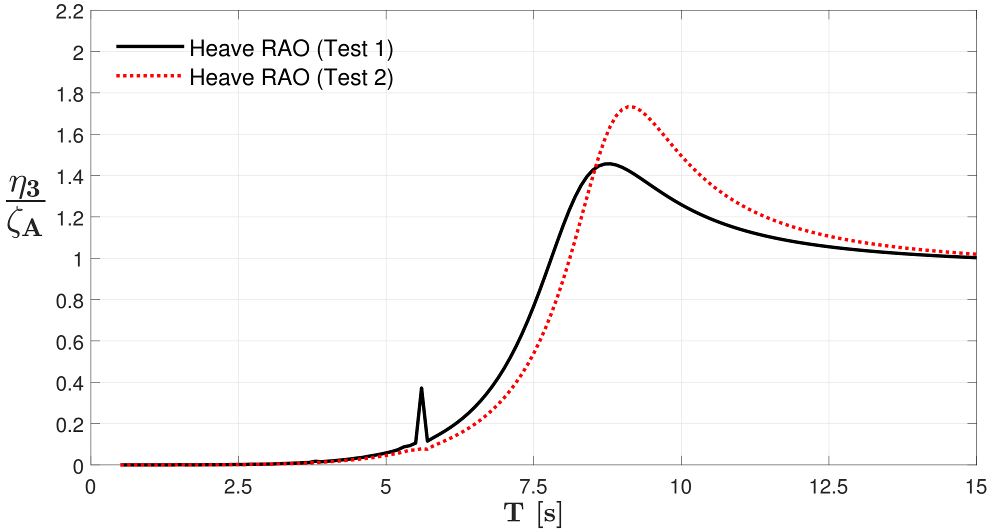

Figure 72: Response Amplitude operator in heave for System 1 *(Test 1)* and System 2 *(Test 2)*

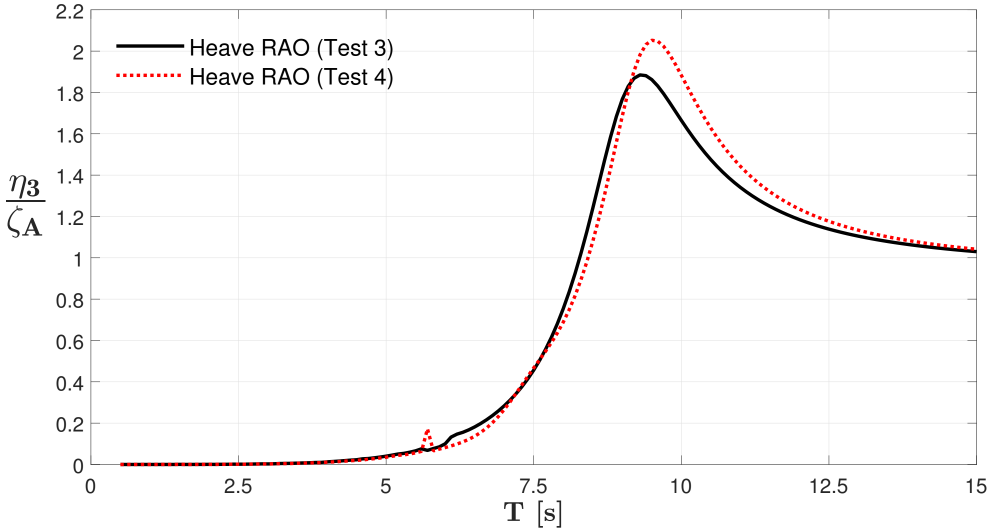

Figure 73: Response Amplitude operator in heave for System 3 *(Test 3)* and System 4 *(Test 4)*

Potential damping

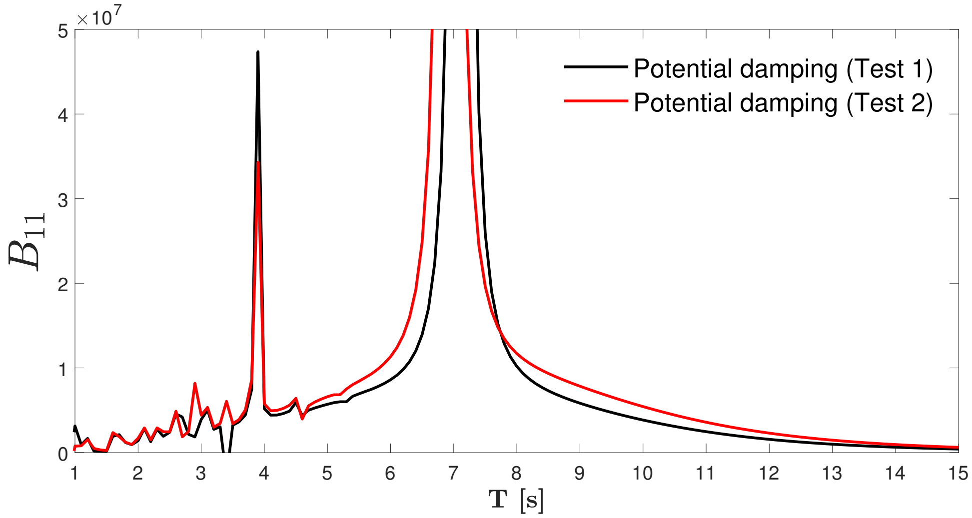

Figure 74: Potential damping B_{11} $[kg/s]$ for *Test 1* and *Test 2* as function of Wave period

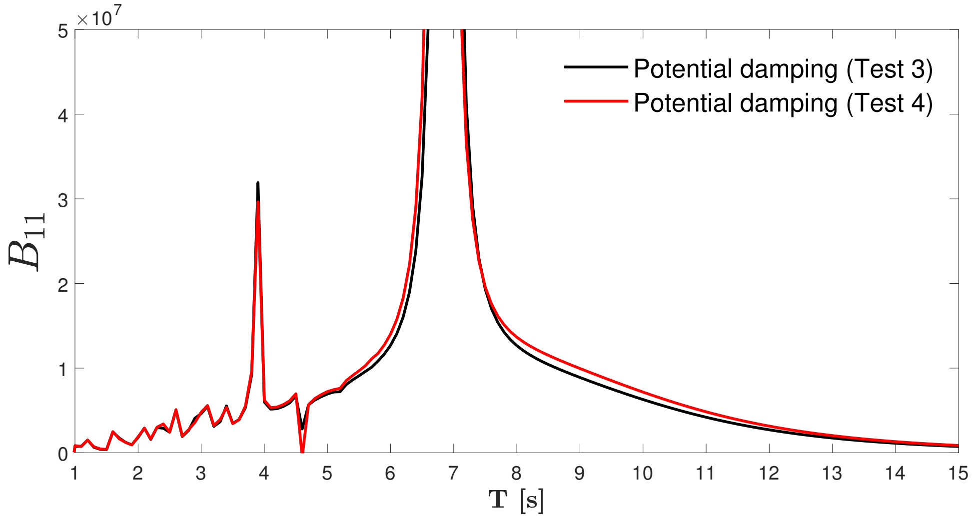

Figure 75: Potential damping B_{11} $[kg/s]$ for *Test 3* and *Test 4* as function of Wave period

Surge motion when using different mooring system and different bottom chain tension

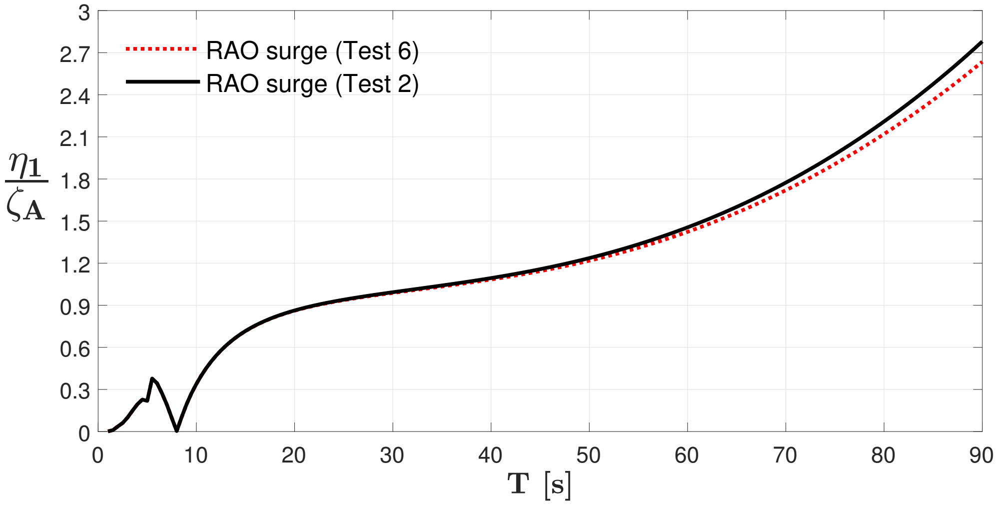

Figure 76: Response Amplitude operator in surge for System 2 *(Test 2)* and System 6 *(Test 6)*, illustrating the effect of using two different mooring system's

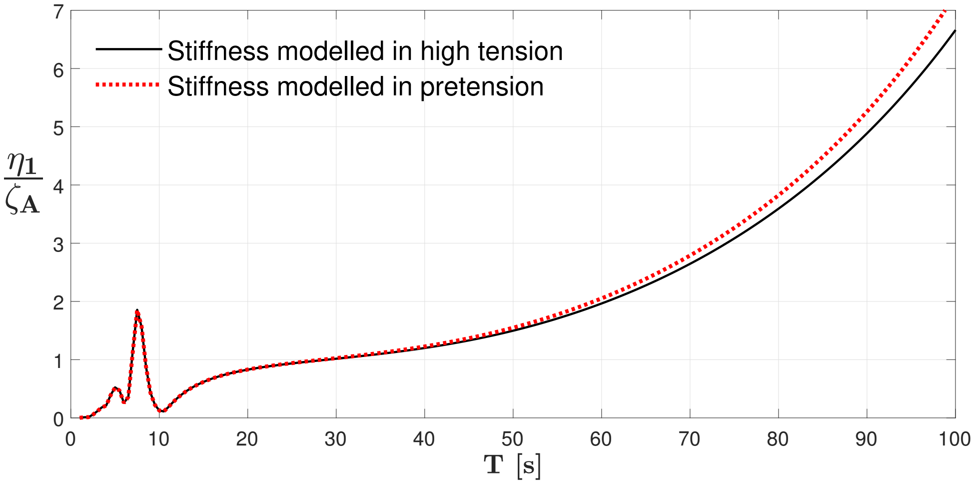

Figure 77: Response Amplitude operator in surge for System 4 *(Test 14)* illustrating the difference when modeling the bottom chain stiffness in T_{Hp} and T_{Hh}

The free surface effect

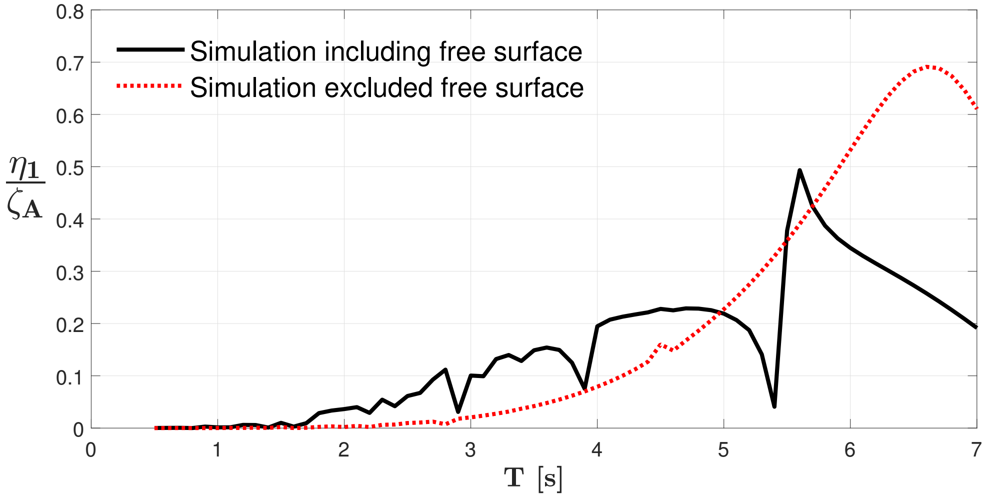

Figure 78: Response amplitude operator for System 2 *(Test 8)* modeled with and without a free surface to investigate influence of the internal water mass

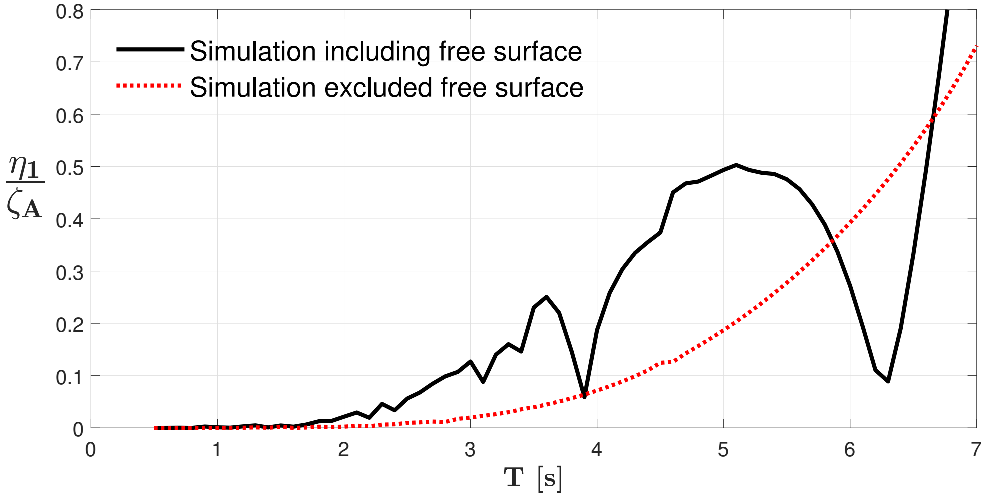

Figure 79: Response amplitude operator for System 4 *(Test 9)* modeled with and without a free surface to investigate influence of the internal water mass.

RAO's used to find damped Eigenperiod

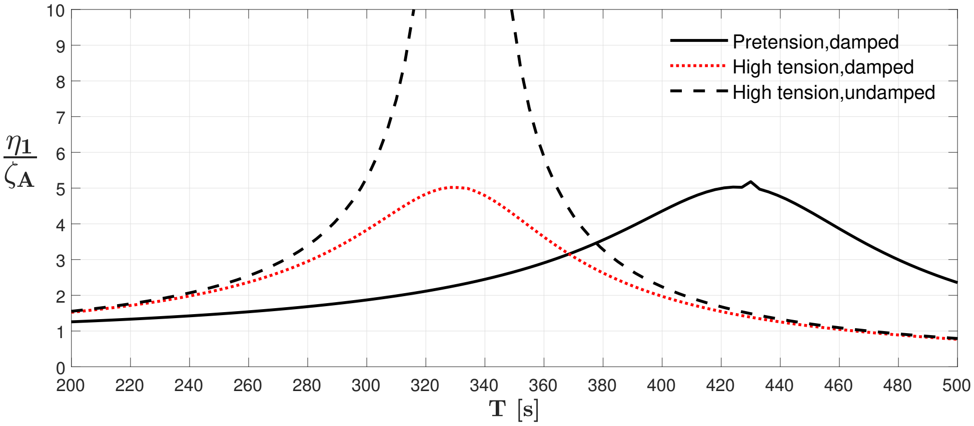

Figure 80: Response Amplitude operator in surge for System 1 *(Test 10)* to find damped eigenperiod

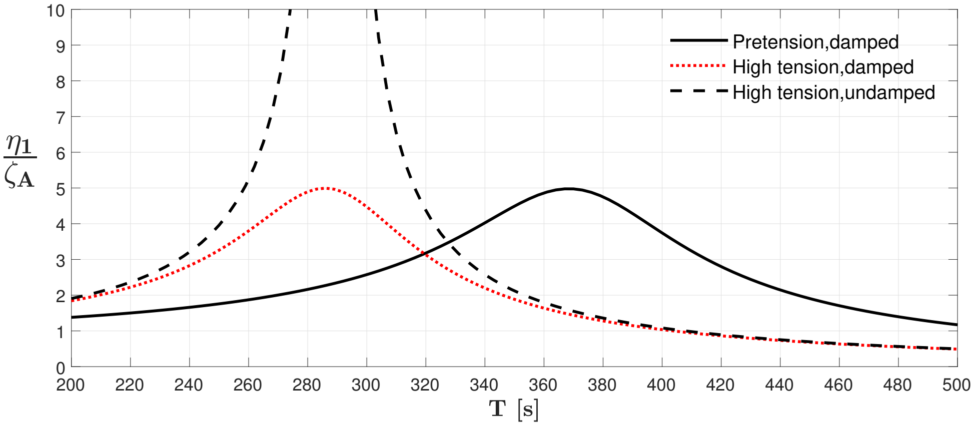

Figure 81: Response Amplitude operator in surge for System 2 *(Test 11)* to find damped eigenperiod

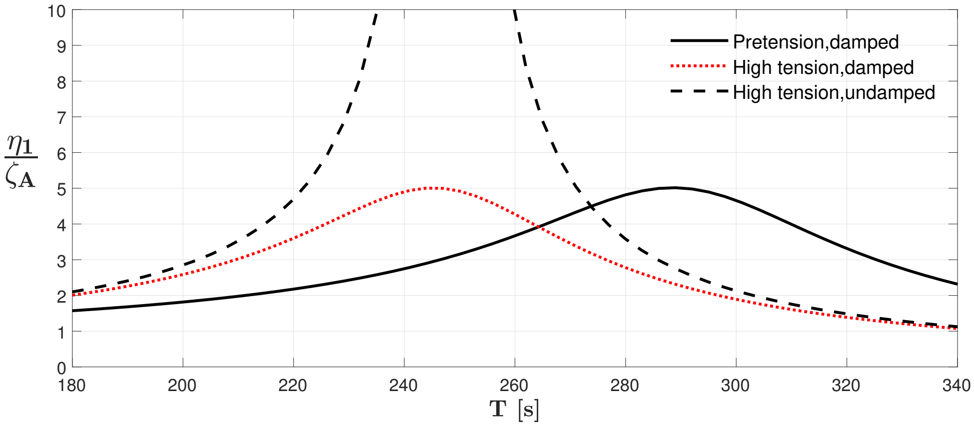

Figure 82: Response Amplitude operator in surge for System 3 *(Test 12)* to find damped eigenperiod

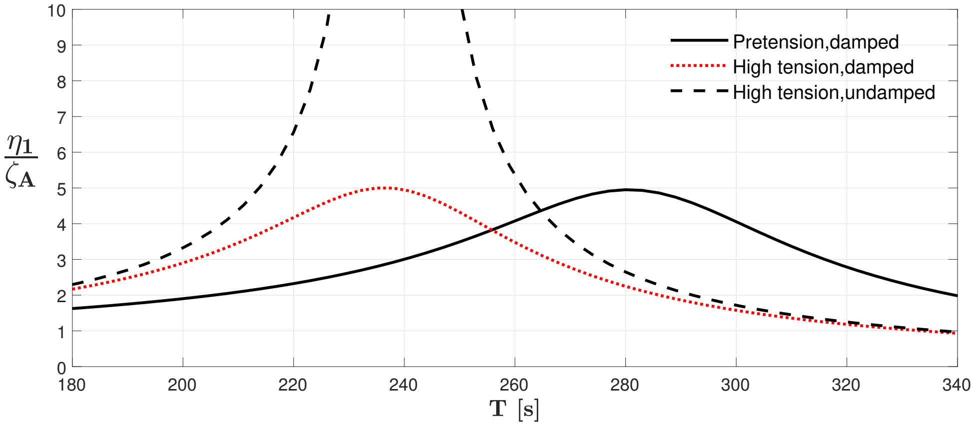

Figure 83: Response Amplitude operator in surge for System 4 *(Test 13)* to find damped eigenperiod

Effect of different heading angles

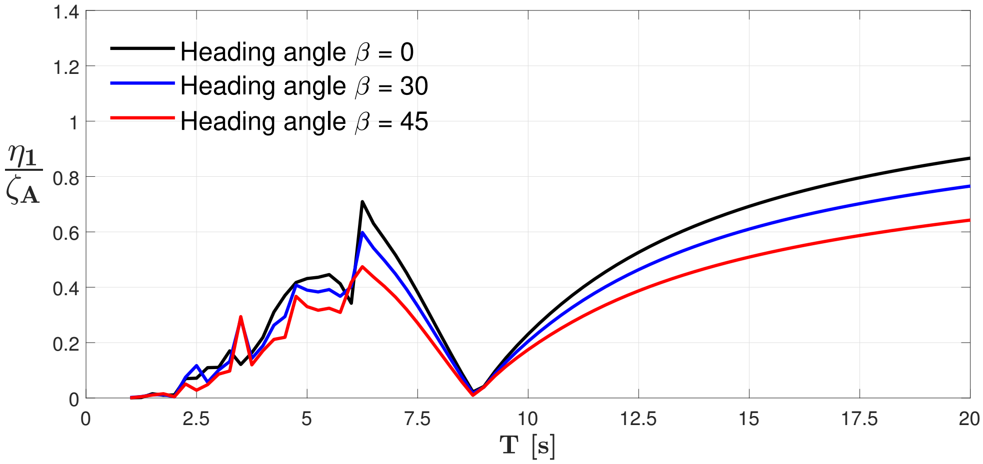

Figure 84: Response Amplitude operator in surge for System 3 *(Test 15)* for three different heading angles ($\beta = 0$, 30, 45 °)

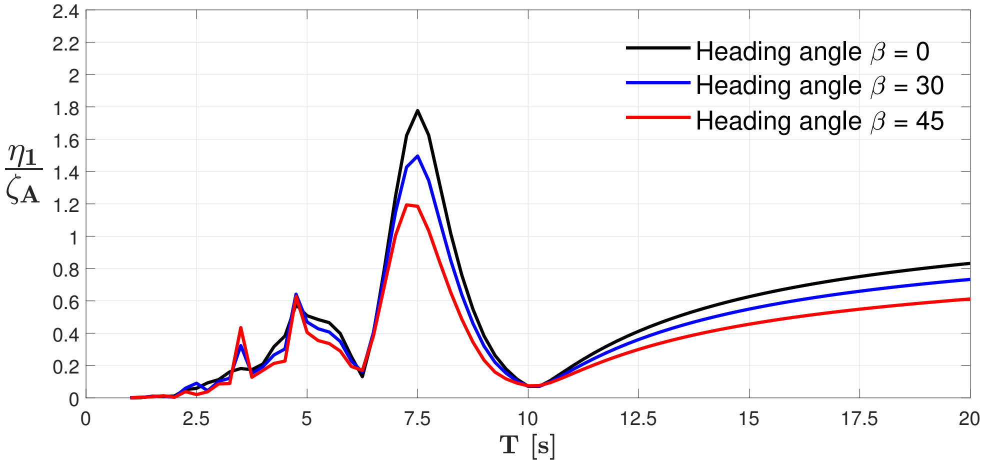

Figure 85: Response Amplitude operator in surge for System 4 *(Test 16)* for three different heading angles ($\beta = 0$, 30, 45 °)

5.1.2 Response spectrum's from dynamic analysis

To enable the dynamic analysis to be used in the mooring system analysis, the response spectrum discussed in section 2.5 has been found for the six combinations of sea states and relevant RAO's from WAMIT. Relevant RAO's from the dynamic analysis in WAMIT include test $1-7$, whilst the six randomly chosen sea states limited to high exposure is listed in table 15. Based on the combinations between the RAO's and the sea states, the most probable maximum motion of the different systems (X_{max}) is calculated from equation 119 using MATLAB. The dynamic force (F_{dyn}) equivalent to the maximum dynamic offset has been found from equation 70, using the relevant system stiffness representing the different mooring systems listed in table 10. The MATLAB plot used to calculate the response spectrum is included in Appendix C.

Table 16 shows the most relevant results from the dynamic analysis. As the purpose of the dynamic analysis is to find the largest motion of the system, the table only include the sea state that imposes the largest horizontal motion on the different systems. The table also includes results for sea state 4, which falls within substantial exposure, defined by NS9415. This is further used when assessing if the classification of the system has to be lowered from high to substantial, discussed later in section 5.3. In addition, the table includes the maximum spectral value for the response and wave spectrum.

Tests including different heading angles and stiffness modeled in high tension have been neglected. Neglecting the tests containing different heading angles has been done due to the results from Test 14 and 15, showing that the RAO is largest for heading angle $\beta = 0$. As mentioned earlier, Test 13 shows that modeling the stiffness in the higher tension state only affects oscillation in the lower frequency domain compared to the relevant wave periods between $T = 0-15$ seconds, making them irrelevant for the response analysis.

Results from dynamic analysis							
Response ID			$S(\omega)_m[\frac{m^2}{rad/s}]$	$S_x(\omega)_m[\frac{m^2}{rad/s}]$	$\sigma_x[m]$	$X_{max}[m]$	$F_{dyn}[kN]$
Sea state limited to high exposure							
XD 1	Test 1	ST_6	0.860	0.19	0.21	0.84	4.6
XD 2	Test 2	ST_6	0.860	0.16	0.18	0.70	6.4
XD 3	Test 3	ST_6	0.860	0.44	0.31	1.23	20.2
XD 4	Test 4	ST_6	0.860	2.48	0.57	2.26	43.6
XD 5	Test 5	ST_6	0.860	0.19	0.21	0.84	12.1
XD 6	Test 6	ST_6	0.860	0.16	0.18	0.69	11.3
XD 7	Test 7	ST_6	0.860	0.44	0.31	1.23	23.7
Sea state limited to substantial exposure							
XD 8	Test 1	ST_4	0.285	0.093	0.141	0.56	3.1
XD 9	Test 2	ST_4	0.285	0.060	0.107	0.43	3.9
XD 10	Test 3	ST_4	0.285	0.083	0.17	0.67	11.0
XD 11	Test 4	ST_4	0.285	0.073	0.18	0.73	14.1
XD 12	Test 5	ST_4	0.285	0.09	0.14	0.56	8.1
XD 13	Test 6	ST_4	0.285	0.060	0.11	0.43	7.1
XD 14	Test 7	ST_4	0.285	0.08	0.17	0.67	12.9

Table 16: Results from the dynamic analysis combing wave spectrum with relevant RAO's

Figure 86 - 89 shows the Response and wave spectrum for Test 1−4 when combined with sea state 6.

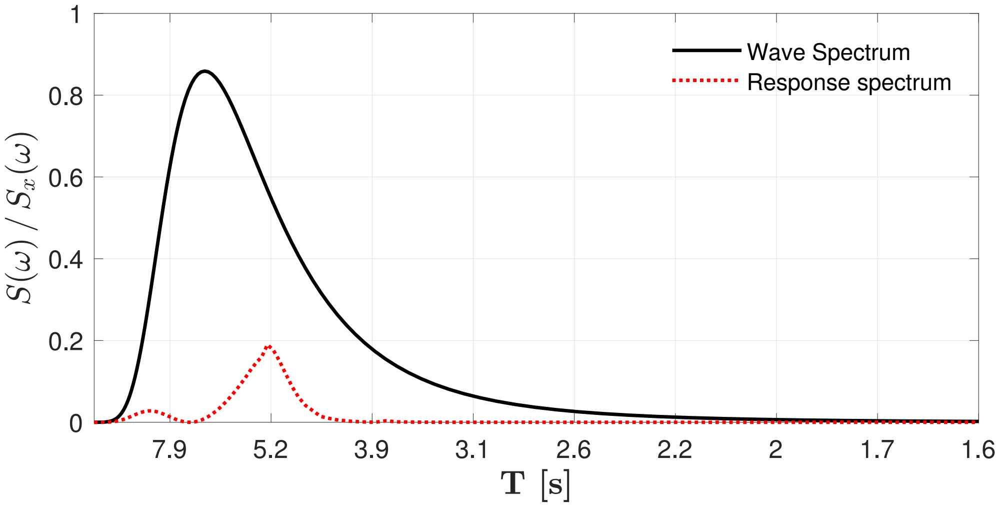

Figure 86: Response spectrum for System 1 *Test 1* combined with Sea state 6. The figure also shows the frequency dependent wave spectrum representing sea state 6

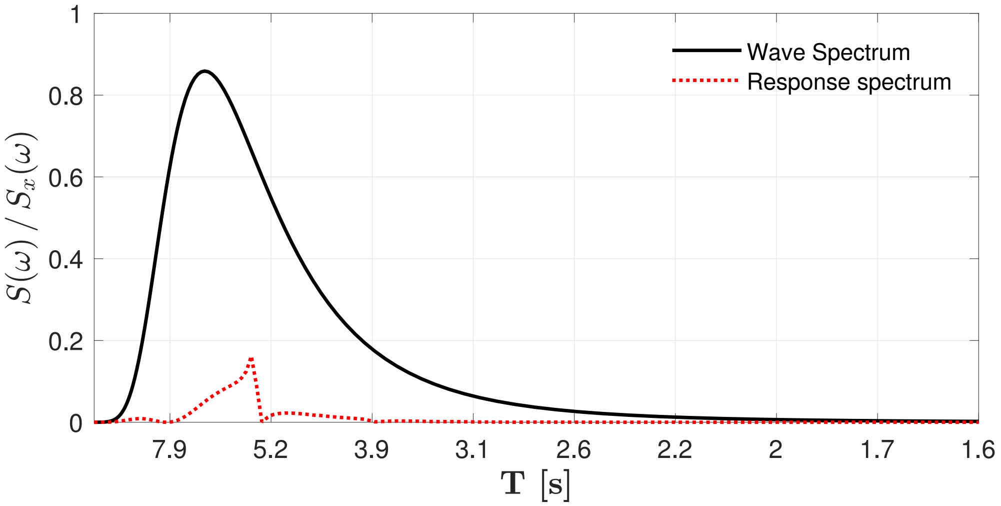

Figure 87: Response spectrum for System 2 *Test 2* combined with Sea state 6. The figure also shows the frequency dependent wave spectrum representing sea state 6

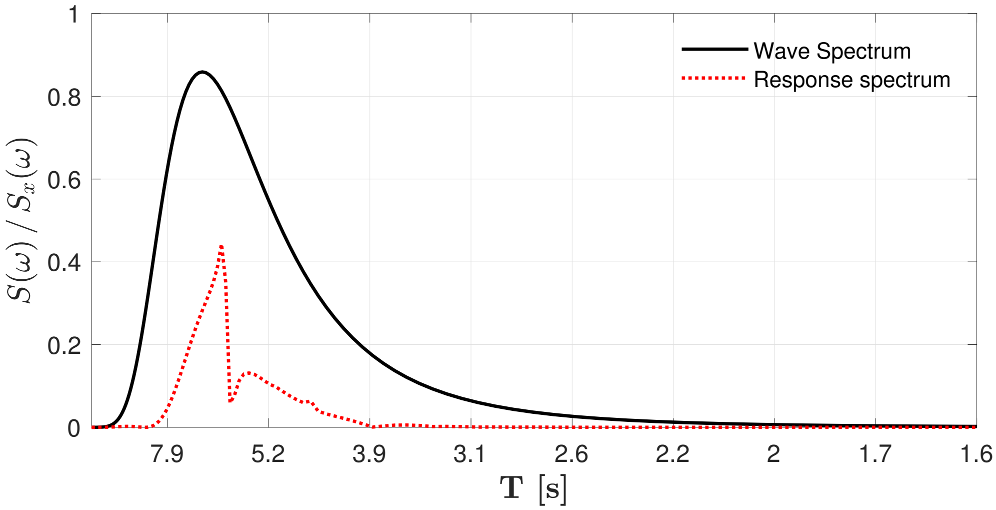

Figure 88: Response spectrum for System 3 *Test 3* combined with Sea state 6. The figure also shows the frequency dependent wave spectrum representing sea state 6

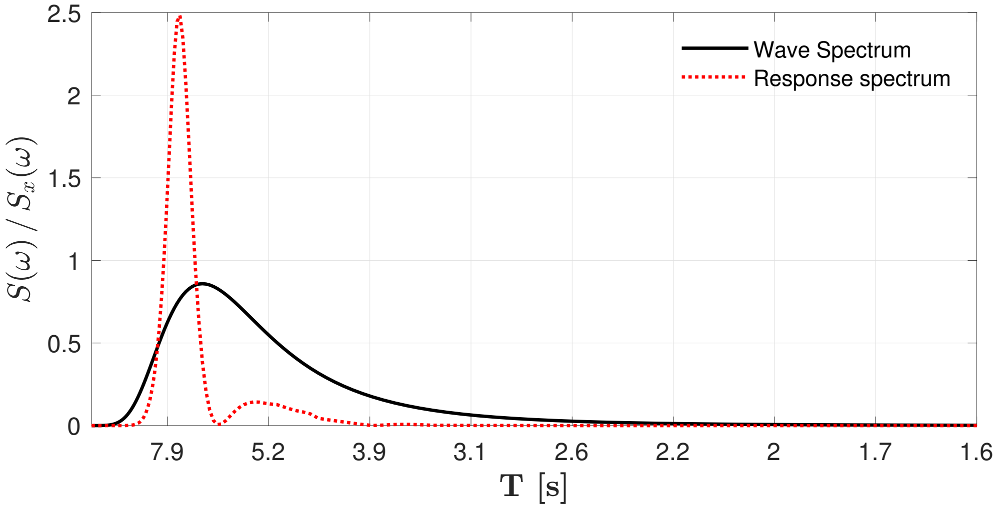

Figure 89: Response spectrum for System 4 *Test 4* combined with Sea state 6. The figure also shows the frequency dependent wave spectrum representing sea state 6

5.1.3 Eigenmodes for sloshing

Table 17 shows typical eigenmodes for sloshing for the designs investigated in the dynamic analysis. The eigenmodes are interesting with regards to the RAO's, where the motion of the internal water mass coincide with the motion of the system as discussed in section 2.3.8. The eigenmodes will be used to evaluate Test 8−9, which compares design 2 and 4 with and without the addition of the free surface. This is to verify that the free surface has been modeled correctly in the dynamic analysis in WAMIT. The eigenmodes are also used when assessing other relevant tests for the mooring system analysis.

The Eigenmodes in the table are based on information from [27] By P.McIver for a spherical design unable to deform. The article highlights different eigenmodes for different geometries depending on the depth of the water mass within a spherical cylinder. For the designs in this paper, the eigenmodes have been taken when the water filling level is in the middle of the sphere, thus representing a hemisphere. This means that the eigenmodes can be used with high accuracy for the hemispherical design, but with less accuracy when evaluating the semi-ellipsoid shapes of design 2−4. A possible solution to account for the different geometrical shape of design 2−4 could have been to alter the water depth, using a larger drought for the internal water mass when using the sphere in [27]. However, this would lead a more egg formed shape representing design 2−4, which would lead to decreased free surface due to a smaller diameter in the water plane. Due to this and after careful consideration, the decision was made to use the hemispherical approach when finding the eigenmodes for sloshing from [27] for design 1−4.

The effect of elasticity is uncertain, and not evaluated in this paper. More information about the mathematical model can be found in [27] by P.McIver. The eigenperiods have been calculated based on equation 93 for the m = 0, 1, 2, 3 azimuthal wavenumbers and the four lowest modes n = 1, 2, 3, 4 using the table for spherical designs in [27].

	Eigenperiods $T_{L\,nm}$ $[s]$ of the internal water-mass			
Azimuth wavenumber	*n = 1*	*n = 2*	*n = 3*	*n = 4*
m = 0	4.64	7.18	5.35	4.49
m = 1	3.40	3.91	3.48	3.18
m = 2	2.82	3.08	2.85	2.67
m = 3	2.45	2.62	2.46	2.34

Table 17: Four lowest eigenperiods for sloshing (T_L) at $m = 0, 1, 2, 3$

It is assumed that the results can be used for all the different designs, even though design 2−4 has a slight deviation from the hemispherical geometry. This means that when evaluating test 8 and 9, there may be deviations from the WAMIT simulation when evaluating the eigenmodes with respect to the RAO.

5.1.4 Discussion - Dynamic analysis

This section aims to shortly discuss the most important results from the dynamic analysis. Also, the validity of the results will be highlighted based on comparisons and interpretation of both internal and external tests.

As seen from figure 68 to 71 (Test $1-7$) highlighting the motion of system $1-7$ when suspected to wave periods relevant for high exposure, it is clear that different geometry leads to different dynamic behavior. This is important to emphasize since the difference is solely due to the height and mass of the structures, where the first design is hemispherical and design $2-4$ is increasingly semi-elliptical shaped in the xz and yz-plane. From the analysis, it becomes evident that design $2-4$ which is heavier and larger is subject to overall larger motion for small wave periods. It can also be seen that the peak in RAO gets increasingly larger for design 3 and 4 compared to design 1, but that design 2 has a lower peak than design 1. This can possibly be explained by the wave period intervals when running the tests in WAMIT, where a narrow peak may disappear due to the interval being too large for specific wave periods. This is illustrated in figure 90, where the same test (Test 2) was conducted for a smaller wave increment ΔT = 0.05 seconds for T = 6.5 seconds, and then compared to figure 69 with ΔT = 0.1 seconds. The difference can also be due to the internal water mass having different sloshing modes and behavior within the structures, affecting the local minima and maxima in the RAO between the structures differently.

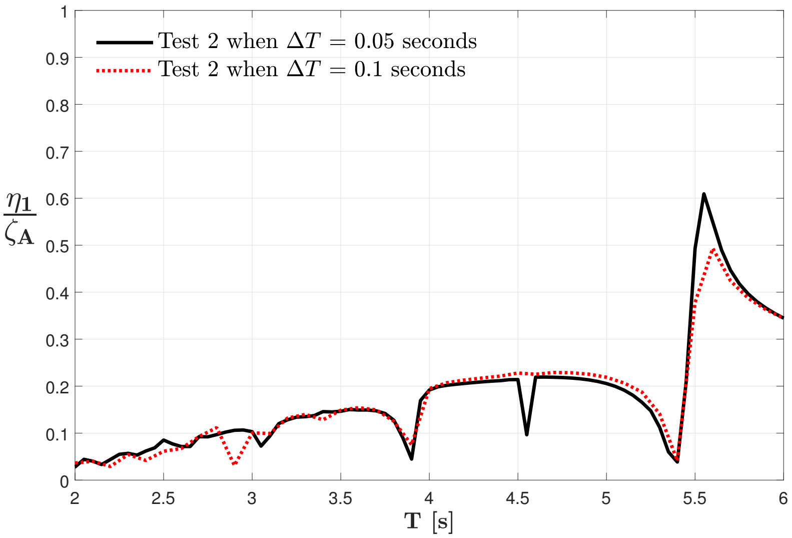

Figure 90: Graph showing how the RAO of test 2 changes as ΔT is larger/smaller in the simulation

Here, it is important to mention that the ΔT steps for the simulations presented in figure $68-71$ is chosen according to computing power and time available when running each simulation. Due to the very small deviations between the results illustrated in figure 90 the wave intervals of ΔT = 0.1 seconds used in test $1-7$ is assumed to be a reasonable ΔT when running the simulations used directly in the mooring analysis. The larger RAO is also evident in heave motion for the same oscillation regime, highlighted in figure 72 and 73 (Test $1-4$), where the motion becomes increasingly larger when the system mass and size increase. Used earlier when assessing the degree of viscous damping on the structure, the SJØFLO investigation by

SINTEF Ocean [8] is used to assess the integrity of the WAMIT simulation. The heave RAO can be used as a reasonable interpretation of the motion obtained in WAMIT due to the similar diameter and water plane area of the structures investigated in this paper compared to the cylindrical design. Here, it is important to emphasize that the heave RAO is comparable to the results obtained for a cylindrical model with $H = R/2$ = 10 meters, which has close to similar mass compared to the hemispherical design (D_1) investigated in this paper.

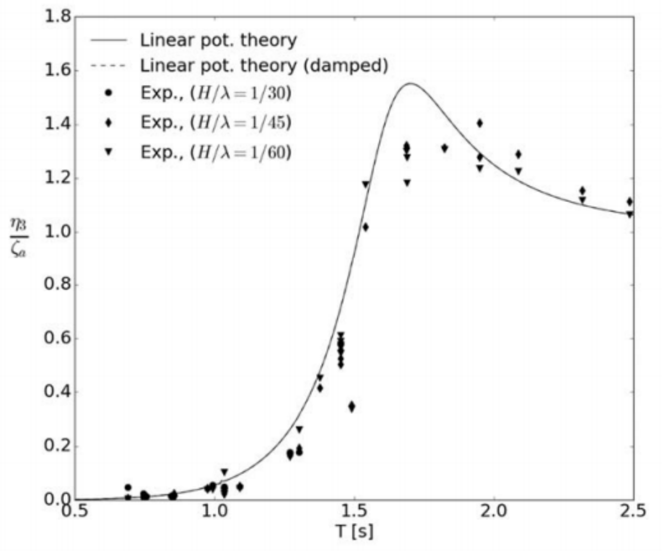

Figure 91: Heave RAO from the SJØFLO project for a model scale cylindrical structure with H = 10 meters and D = 40 meters [8]

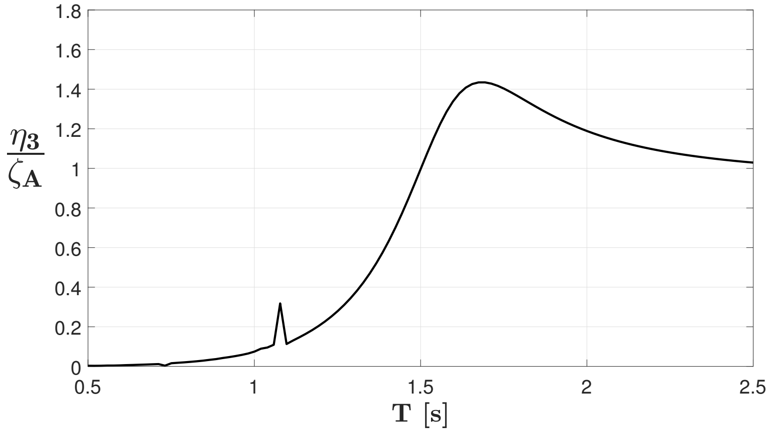

Figure 92: Heave RAO from for test 1 scaled to model scale using Froude scaling with λ_f = 27

Figure 92 shows the heave RAO for test 1 (figure 72) when the wave period regime is scaled to model scale using the Froude scaling factor $\lambda_f = 27$, making it easier when comparing to the SJØFLO result in figure 91. From the results highlighted in figure 91 from the SJØFLO project, it can be seen that the heave RAO is close to identical for system 1 (Test 1) investigated in this paper and the heave RAO for the cylindrical structure, which has close to equal mass. Regarding system 2, 3 and 4 which is represented in test 2, 3 and 4 in figure 72 and 73 the larger RAO's can be justified by the increased system size.

Figure 74 and 75 shows the potential damping coefficient for system $1-4$ (Test $1-4$). As seen from the figures, all tests are prone to two distinct peaks. These peaks are due to the sloshing phenomenon, occurring at anti symmetric sloshing periods, which is a numerical effect due to singularity of the internal problem in free surface tank [8]. In addition, several local maxima and minima can be observed at low wave periods, which can also be familiarized with sloshing periods for the system. Figure 93 Shows the phenomenon occurring due to the internal free surface by comparing the damping coefficient for system 4 (test 4) when the system is modeled in WAMIT with and without the free surface.

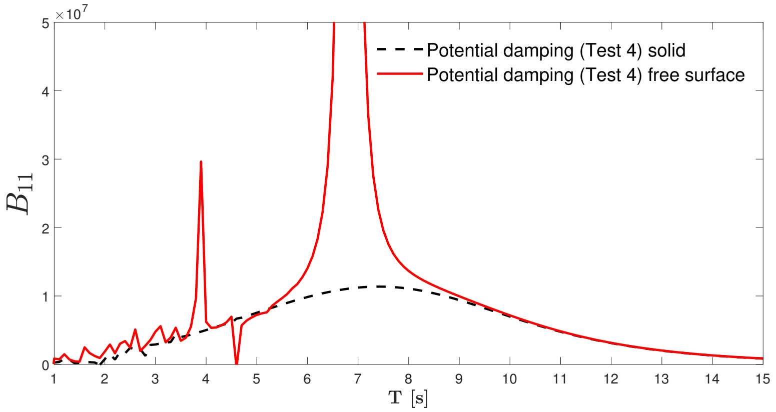

Figure 93: Potential damping for system 4 (Test 4) with and without the free surface

The important takeaway from the damping results is that the incline and decline in the front of and back of the largest peak makes physical sense with regards to wave making from horizontal motion. It is also important when evaluating the integrity of the low potential damping coefficient obtained in table 11, when finding a reasonably added damping coefficient to account for Viscous effects in section 3.3. The low damping coefficient is due to the very high oscillation period of T_m = 116 seconds which is confirmed by the declining damping coefficient in figure 93 for high wave periods. As seen from table 11 using the decay test in the SJØFLO project, it is evident that the linear damping from the test most likely originates from other than potential damping effects. Another explanation for the large linear damping compared to the potential damping could be the difference in geometry, where the SJØFLO model may be suspect to more wave making for large oscillation periods compared to the designs investigated in this paper. This uncertainty doesn't significantly affect the results, as the user specified damping matrix has been modeled according to a percentage of the critical damping of the different system's. However, it could mean that the damping should have been modeled at a lower level ($< 10\%$) based on the results from the decay test. Figure 93 also indicate that due to the free surface, the potential damping may be overpredicted at certain oscillation periods relevant for the analysis in WAMIT due to the singularity of the internal problem.

Figure 76 (Test 2 and 6) and 77 (Test 14) highlights how the RAO change when the total stiffness (K_{11}) is increased using a more robust mooring system and how the RAO change when modeling the bottom chain stiffness in a higher tension state respectively. Here it can be seen that even for substantially higher wave periods, the mooring system has minimal effect on the wave-frequency dynamic motion of the system. This is mainly due to the nature of the mooring systems used in the aquaculture industry, where the stiffness is insufficient to significantly affect the rapid dynamic motion of the system in the wave frequency regime. This is supported by figure 68 - 70, where the RAO when T = $0-15$ seconds is unaffected when changing the mooring system for design 1-3.

This is even further supported by figure 80 - 83 which highlights the eigenperiod of system $1-4$ in surge. It can also be seen that modeling the stiffness of the bottom chain in a higher tension state largely affects the eigenperiod of the system for high oscillation periods. This means that the mooring system only has a significant effect on the RAO's for very high oscillation periods, outside the high exposure regime. This amplifies the importance of second-order slowly varying forces, discussed in the mooring system discussion in section 5.3.4. It also means that the nonlinear characteristic of the bottom chain in the mooring system has the ability to largely affect the eigenperiod of the system depending on the line tension and horizontal offset. This is important to emphasize due to the linear stiffness modeled in WAMIT, not accounting for the changing stiffness of the bottom chain as the system moves horizontally.

Figure 78 (Test 8) and 79 (Test 9) illustrates system 2 and 4 respectively when the internal water mass is modeled as a solid within the structure compared to when the structure has a free surface. Here, it is evident that the free surface has a significant effect on the surge motion of the system, as the motion is highly inconsistent when the free surface is active compared to the solid structure with equal mass. When comparing the eigenperiods for sloshing (T_L) highlighted in table 17 with the results in figure 78 and figure 79, two different effects is noticeable, for some periods there is cancellation effect, and for some periods there is an amplification of the motion. These periods coincide reasonably well with the lowest eigenperiods for sloshing, but there is some deviations.

For figure 78 representing design 2 the three first significant cancellation periods at $T \approx$ 2.9 seconds, $T \approx$ 3.9 seconds and $T \approx$ 5.3 seconds coincide very well with T_{L32} = 2.85 seconds, T_{L21} = 3.91 seconds and T_{L30} = 5.35 seconds respectively. However, there is some deviation for the first amplification period at $T \approx$ 5.6 seconds.

For figure 79 representing design 4, the two first significant amplifications occur at $T \approx$ 3.6 seconds and $T \approx$ 5.0-5.2 seconds which coincide well with T_{L31} = 3.48 seconds and T_{L30} = 5.35 seconds respectively. The first cancellation significant cancellation period at $T \approx$ 3.9 seconds coincide with T_{L21} = 3.91 seconds.

The deviation between the sloshing periods and the behavior of the RAO's is most likely due to the nature of the sloshing periods, where the periods have been calculated based on the assumption that the geometry is hemispherical. This is not the case for the designs investigated in figure 78 and 79 which represent the semi-ellipsoid geometry of design 2 and 4 respectively.

However, if the Eigenperiods for sloshing is compared with figure 68 (Test 1) which investigates design 1 with a perfectly hemispherical geometry, it can be seen that the first cancellation period at $T \approx$ 3.9 seconds can be identified with T_{L21} = 3.91 seconds. It can also be seen that the significant peak at $T \approx$ 5.3 seconds coincide well with T_{L30} = 5.35 seconds. This means that the sloshing periods found from [27] By P.McIver, respond reasonably well with the results obtained in the dynamic analysis in WAMIT. The cancellation and amplification phenomenon connected to the internal water mass is dependent on the phase of the wave that occurs when the structure moves. If the wave is out of phase with the motion of the structure, there will be cancellation effects, whilst if the wave is in phase with the motion, there will amplification effects. From this interpretation, in combination with the RAO, it is possible to decide the relative phase of the internal wave from interpreting the results. It is also important to mention the possibility of local maxima and minima disappearing, or not leading to full cancellation or amplification if the ΔT step has been taken at a to large increment. This revolves around the same problem as seen in figure 90, further highlighting the importance of running the tests with a fine increment for ΔT.

Figure 80 - 83, which highlights the eigenperiods of system 1-4 both when the bottom chain is in the pre-tensioned and high tension state, is used to confirm that the eigenperiods calculated from equation 101 in table 13 coincide with the simulations in WAMIT. Here, it can be seen from the figures that the distinct peak highlighting the onset of resonance in the structure occurs at almost the exact same wave periods as the eigenperiods of the system listed in table 13. System $1-4$ is highlighted due to the similar trend between all structures, making it unnecessary to highlight the results for test $5-7$. Modeling the internal water mass as a solid within the structure when investigating the eigenperiod in surge, can be justified by the large period identified with the eigenperiod of the system, assuming that the internal water mass will have little effect when the system is oscillating with very low frequency. This was also necessary due to the large testing regime for wave periods, easing the strain on the solver in WAMIT.

Concerning figure 84 and 85 highlighting test 15 and 16, where different heading angles are plotted for system 3 and 4 respectively, it can be seen that $\beta = 0$ gives the overall largest RAO of the different systems. This is expected due to the orthogonal layout of the mooring systems, where several mooring lines in the transverse direction becomes active when the heading angle get altered counterclockwise, as illustrated in figure 27. Due to the results from test 15 and 16, the dynamic analysis accounting for irregular waves only concern $\beta = 0$. As for the other tests, all structures were tested for the different heading angles, but excluded from the results due to their similar outcome compared to system 3 and 4.

When evaluating the most probable maximum offset of the system denoted as X_{max}, it can be seen that sea state 6 gives the largest motion for all systems. Here, tests where conducted for all combinations between the six different sea states and test $1-7$, to investigate the possibility of larger response for sea state $1-5$. This could have been a possibility if large peaks in the RAO coincided with large peaks in sea state $1-5$ compared to sea state 6. The relatively small motion is expected in the wave frequency regime, especially for large volume structures when suspected to limited sea state exposure.

Figure $86-89$ shows the spectral energy of the response spectrum in surge motion plotted against relevant wave periods for test $1-4$. From figure 86 connected to test 1 it can be seen that the peak in the response spectrum coincides well with the peak in the RAO from figure 68 around $T = 4-7$ seconds. This is supported by the large spectral energy around the same wave periods seen from the spectral shape representing the sea state.

This is also the case for figure 87 and 88 showing that the response spectrum for test 2 and 3 coincide well with T = $5-8$ and $T \approx 4-8$ seconds respectively. Regarding figure 89 showing the response spectrum for test 4 combined with sea state 6, it can be seen that there is a large peak in the spectrum at $T \approx 7.5$ seconds. This is due to the large peak in the RAO for test 4, coinciding well with large spectral energy values for the sea state. From equation 117 it can be seen that the RAO is squared when obtaining the response spectrum, meaning that values $>>1$ will yield large response compared to $1>>$. This explains the significantly increased motion of test 4 compared to the other tests.

5.2 Static analysis

As for the dynamic analysis, the static analysis is subject to the test conditions listed in table 15 and the system's listed in table 13 denoted as test $1-7$ in table 14. When estimating forces from current, the drag coefficient has been decided by evaluating experimental results in figure 36 for the smooth sphere for relevant Reynolds numbers decided by the diameter of the structure and the current velocity.

The projected area has been estimated as described in section 2.4.2, and the drag force has been estimated from equation 112. When estimating the drag force, the collar has been excluded from the geometry. This is considered a reasonable assumption due to the small projected area of the collar outside the area of the membrane.

The nondimensional mean drift force coefficients are estimated from the WAMIT simulation using the conservation of fluid momentum method highlighted in section 2.4.1. This coefficient serves much of the same purpose as the RAO from the dynamic analysis when evaluating the effect of second-order mean drift forces on the system. Based on the nondimensional coefficient, the total mean drift force ($F_{1(md\,tot)}$) when the system gets suspected to the six different sea states in table 15 has been found using equation 111. As for the dynamic analysis, the table includes the largest force when the system gets suspected to the different sea states limited to high exposure in table 15. It also includes results for when the exposure is lowered to substantial.

The WAMIT files including the FRC, POT and GDF file used in test $1-7$ in the dynamic analysis are the same as when estimating the nondimensional mean drift force coefficients. This means that the geometry is represented by the same amount of panels. Here it is important to mention that the solver failed to converge for a large number of wave periods when using the iterative solver, meaning that the direct solver had to be used in many instances. To assure that the direct solver gave realistic results, valid results obtained when using the iterative solver were compared to results when using the direct solver.

As the WAMIT simulations for Test $1-7$ has been conducted for $T \in$ [0, 15] seconds with steps ΔT = 0.1, the amplitudes used to evaluate the total mean drift force has been decided according to equation 121, using the equivalent step for $\Delta\omega$. This method enables the irregular sea state to be treated as a series of regular waves inducing a combined mean drift force on the system.

All calculations have been performed in MATLAB. The MATLAB script used to estimate the total mean drift force is included in Appendix D. The following section includes the nondimensional mean drift force coefficient for test $1-4$ as a function of the wave period. Test $5-7$ is not included as graphs due to their close to similar shape compared to test $1-3$.

5.2.1 Nondimensional mean drift coefficients from WAMIT

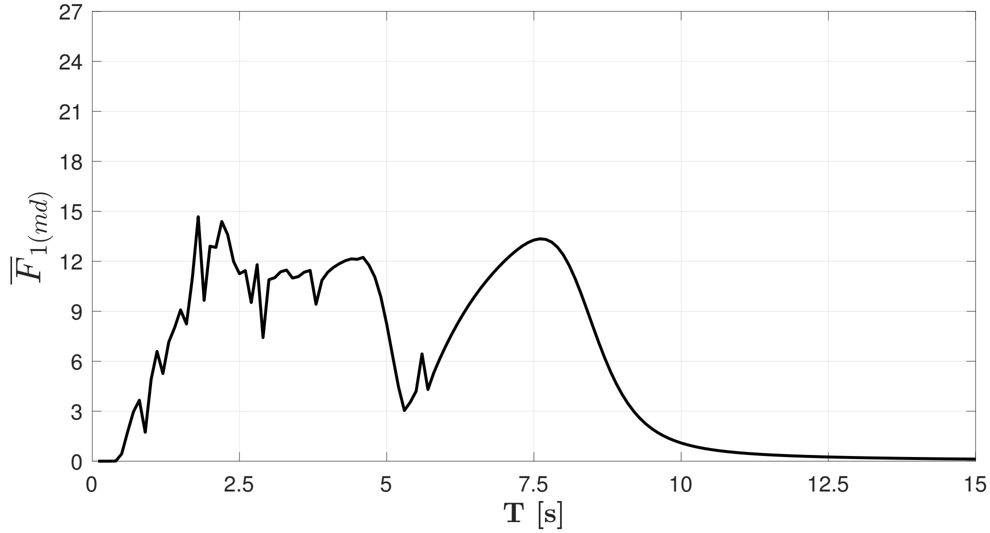

Figure 94: Nondimensional mean drift force coefficient in surge for System 1 *(Test 1)*

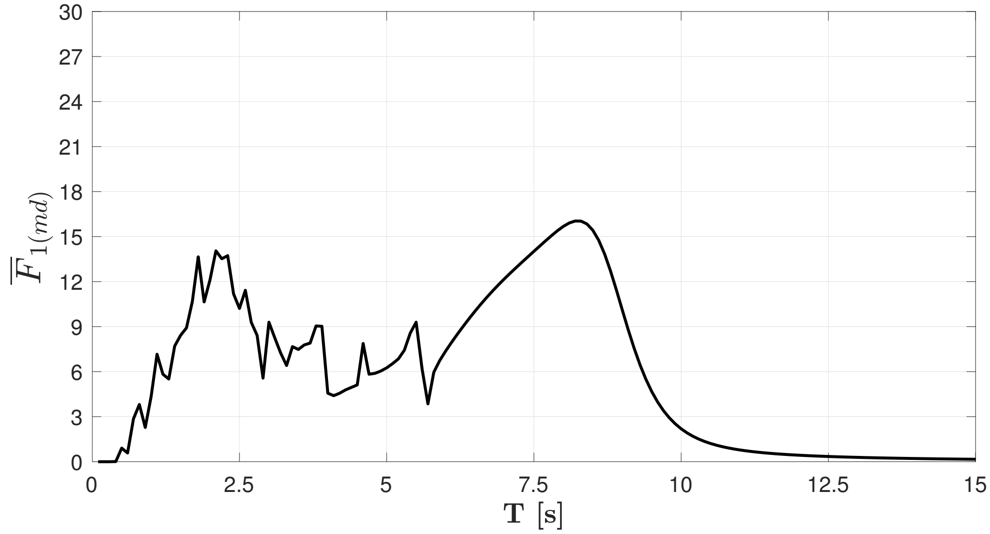

Figure 95: Nondimensional mean drift force coefficient in surge for System 2 *(Test 2)*

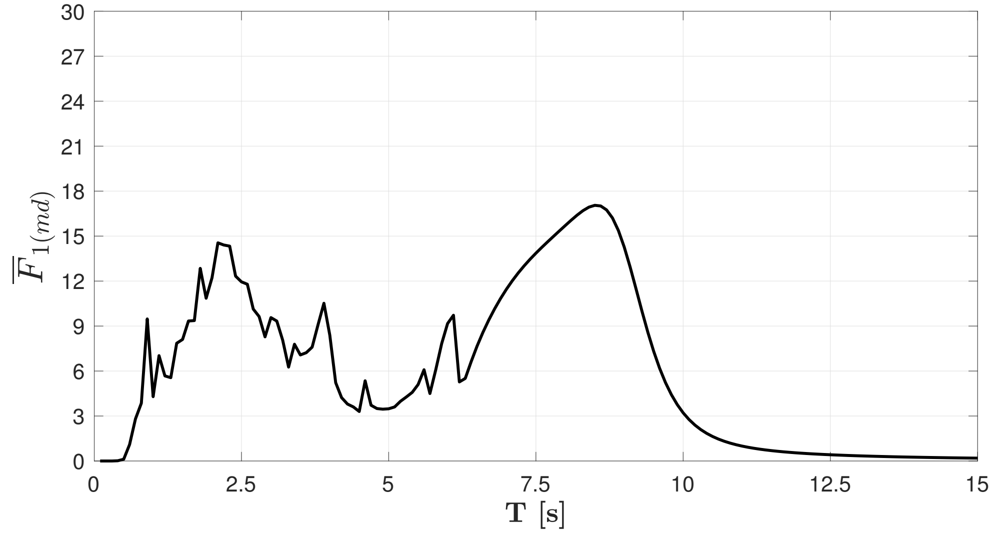

Figure 96: Nondimensional mean drift force coefficient in surge for System 3 *(Test 3)*

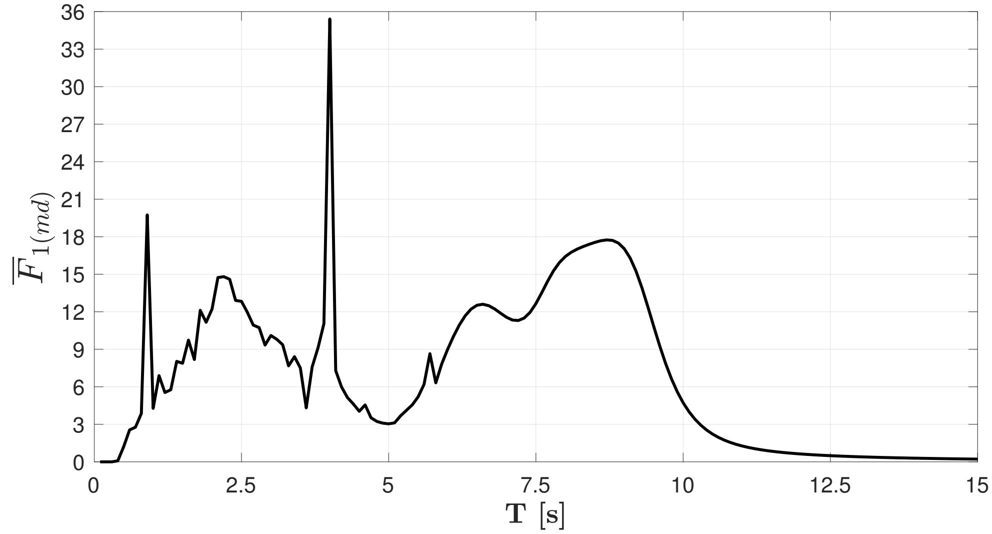

Figure 97: Nondimensional mean drift force coefficient in surge for System 4 *(Test 4)*

5.2.2 Total mean drift force

Table 18 shows the most relevant results when combining Test 1−7 by the six different sea states listed in Table 15. The most relevant results include the combination between the systems and the sea state which gives the largest total mean drift force on the structure. It also includes results for Sea state 4, used when assessing the classification of the system later in section 5.3.

The mean drift force is calculated for unidirectional waves. As for the dynamic analysis, this means that the only wave heading considered is β = 0. For the structures investigated in this paper, the geometry file contains the full-scale dimension of the four different structures. In the GDF file specified by the user, the acceleration of gravity defines the dimension of the physical parameters when using the nondimensional coefficients obtained from the simulations, set to g = 9.81 m/s.

The combination between g = 9.81 m/s and the GDF file containing the full scale dimension of the structure makes ULEN = L = 1 with dimension $[m]$, when calculating the total mean drift force from equation 111. If the structure was scaled to model scale when defining the geometry file in WAMIT, L would have a different size, representing the length scale when finding the full-scale values. This means that L serves much of the same purpose as the Froude scaling factor described in section 2.6. As the WAMIT simulation for test 1−7 is carried out for T = 0−15 seconds with ΔT = 0.1 seconds, equation 111 is solved by summation over N = 146 waves for the different irregular sea states to find the total mean drift force.

Results from Mean drift analysis					
Mean drift ID	Test ID	Sea state ID	$\zeta_A\ [m]$	$\overline{F}_{1\,(md)}$	$F_{1\,(md\,tot)}\ [kN]$
Sea state limited to high exposure					
MD 1	Test 1	ST_6	0 - 0.16	0 - 14.67	104.7
MD 2	Test 2	ST_6	0 - 0.16	0 - 16.04	100.3
MD 3	Test 3	ST_6	0 - 0.16	0 - 17.05	91.9
MD 4	Test 4	ST_6	0 - 0.16	0 - 35.41	106.3
MD 5	Test 5	ST_6	0 - 0.16	0 - 14.67	104.3
MD 6	Test 6	ST_6	0 - 0.16	0 - 16.04	100.4
MD 7	Test 7	ST_6	0 - 0.16	0 - 17.05	91.9
Sea state limited to substantial exposure					
MD 8	Test 1	ST_4	0 - 0.13	0 - 14.67	47.7
MD 9	Test 2	ST_4	0 - 0.13	0 - 16.04	35.6
MD 10	Test 3	ST_4	0 - 0.13	0 - 17.05	32.7
MD 11	Test 4	ST_4	0 - 0.13	0 - 35.41	39.4
MD 12	Test 5	ST_4	0 - 0.13	0 - 14.67	47.7
MD 13	Test 6	ST_4	0 - 0.13	0 - 16.04	36.0
MD 14	Test 7	ST_4	0 - 0.13	0 - 17.05	32.7

Table 18: Result from static analysis, Total mean wave drift force

5.2.3 Forces from current

Table 19 contains the results from analyzing the drag force from current on the four different designs using equation 112. The table shows the drag force for different current velocities ranging from V_c = 0.1−1 m/s. The projected area of the four different structures is listed in table 4. Due to the constant diameter (D_m = 40 meters) of the four different designs, the Reynolds number ranges from ($Re = 0.21 \times 10^7$) to ($Re = 2.19 \times 10^7$) for the minimum (V_c = 0.1 m / s) and maximum current velocity (V_c = 1.0 m/s) respectively. The viscosity of seawater has been set to $\nu = 1.83 \times 10^6$ and the Drag coefficient has been found from the span of the Reynolds number as C_d = 0.35 from figure 36.

Results from current analysis					
Current ID	Current velocity (V_c) [m/s]	Drag force ($F_{1(c)}$) [kN]			
		Design (D_1)	Design (D_2)	Design (D_3)	Design (D_4)
CU 1	0.1	1.127	1.353	1.465	1.578
CU 2	0.2	4.508	5.410	5.861	6.312
CU 3	0.3	10.143	12.172	13.187	14.201
CU 4	0.4	18.033	21.6407	23.443	25.246
CU 5	0.5	28.176	33.810	36.629	39.447
CU 6	0.6	40.578	48.689	52.746	56.803
CU 7	0.7	55.525	66.270	71.793	77.315
CU 8	0.8	72.131	86.557	93.770	100.983
CU 9	0.9	91.291	109.55	118.678	127.807
CU 10	1.0	112.71	135.30	146.516	157.789

Table 19: Drag force calculated from Morison's Equation for $V_c = 0 - 1.0\,m/s$

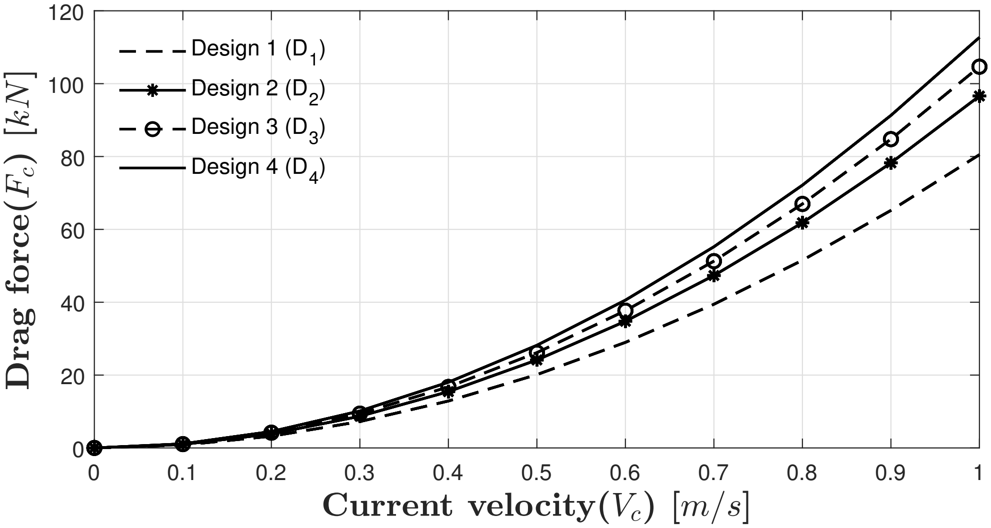

Figure 98: Drag force as function of current velocity for D_1, D_2, D_3 and D_4

5.2.4 Discussion - Static analysis

This section aims to shortly discuss the results obtained in the static analysis. Also, the validity of the results will be highlighted based on comparisons and interpretation of the different tests.

When evaluating the frequency dependent nondimensional mean drift force coefficients for test $1-4$, listed in figure $94-97$ it is evident that the drift coefficient has its largest values for low wave periods. This is due to the close connection between horizontal mean drift forces and body capability in generating waves. When the wave period increases, the body will more or less follow the motion of the wave, making it generate less waves than when suspected to motion in the low-frequency regime [16] (Chapter 6).

To be able to interpreter the results obtained from the WAMIT simulation regarding the nondimensional mean drift force coefficient and its validity, the SJØFLO investigation [8] will be used to compare the results for system 1. As for the dynamic analysis, system 1 represented by test 1 in figure 94 is chosen due to its close to equal full-scale mass to one of the cylindrical models investigated in the SJØFLO project, with $R = 2H$ denoted as model $K11$ in [8]. Here, H is the drought of the structure.

Equation 110 shows the correlation between the mean drift force and the drift coefficient. Here it is important to emphasize that L^k is the length scale used in the WAMIT simulation, set equal to 1 when running the simulations in this paper. This is due to the geometry file representing the full-scale structure with $D =$ 40 meters. In the SJØFLO report, the tests are carried out in model scale, making it natural to plot the nondimensional drift coefficient as listed in equation 110 by setting $L = D$ where D represent the diameter of the structure.

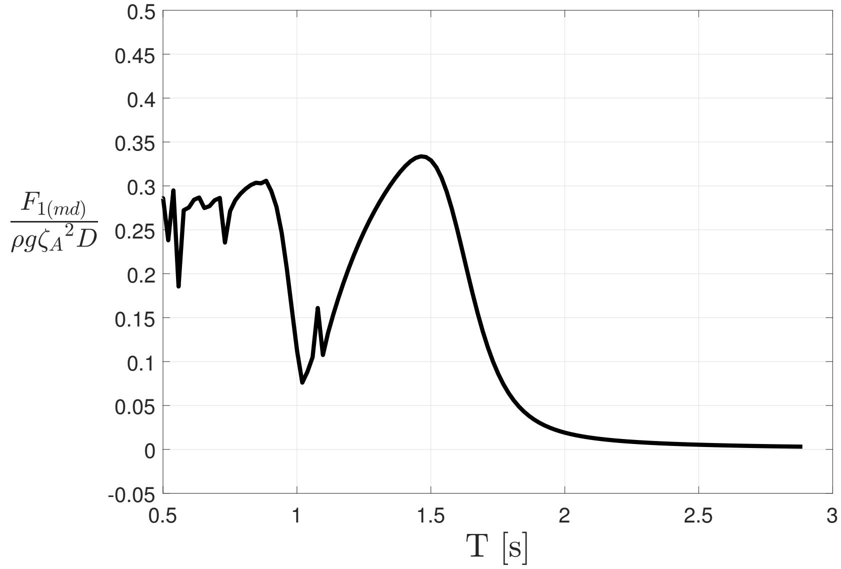

Figure 99: Nondimensional mean drift coefficient for test 1 as function of D and wave periods converted to model scale using λ_f

This means that to be able to compare the results from this paper to the results obtained in the SJØFLO report, the nondimensional mean drift force coefficient in figure 94 representing test 1 is divided by the diameter of the structure (D = 40 meters), obtaining the graph in figure 99. In addition, the wave period regime is scaled to model scale using the Froude scaling factor λ_f = 27.

Figure 100 shows the nondimensional mean drift force coefficient obtained from the experiments and from the WAMIT simulation in the SJØFLO project.

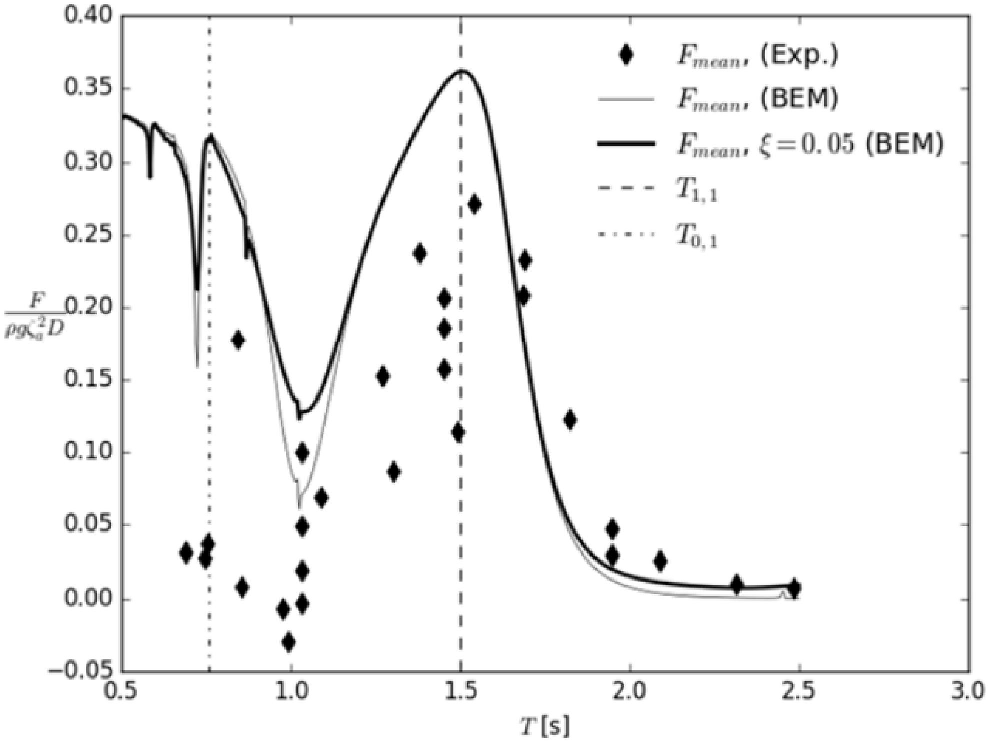

Figure 100: Nondimensional mean drift coefficient from *SJØFLO* project, $R = 2H$ (model $K11$), similar mass to System 1 and equal diameter (D = 40 meters) [8]

From the comparison between figure 99 and 100, the overall shape of the nondimensional mean drift force is fairly similar for the hemispherical design and the cylindrical design from the SJØFLO investigation. It can also be seen that the scatter is larger for the hemispherical design. The scatter and large amount of local maxima and minima is due to the internal water mass connected to sloshing, affecting the geometries differently, leading to different local behavior. This is especially evident for high-frequency motion, which can be justified by the large number of eigenmodes and periods for sloshing connected to small wave periods, as seen in table 17.

The influence of the free surface can be justified by figure 101, showing how the mean drift force coefficient for system 1 (test 1) in figure 94 is largely influenced by the internal water mass in the CFFC. This enables the possibility to compare the results with good accuracy. Here, it is important to emphasize that the user specified mass matrix ($M^{(e)}$) is the only parameter modeled differently in WAMIT when accounting for the solid structure, which may lead to small deviations from real time results.

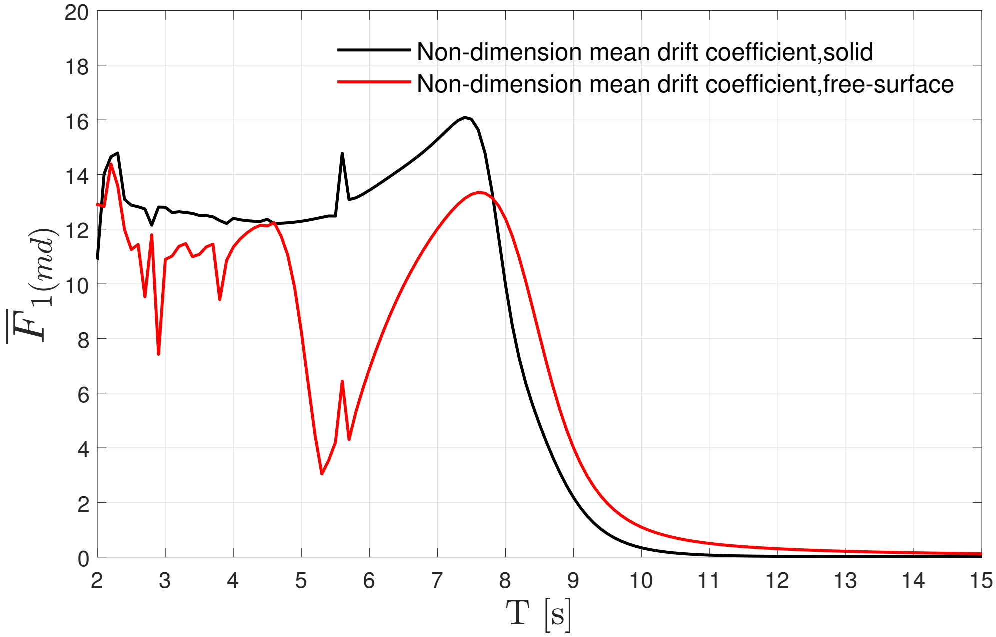

Figure 101: Nondimensional mean drift coefficient for system 1 (test 1) with and without the free surface effect

Using figure 101, evaluating the eigenmodes for sloshing listed in table 17 it can be seen that the first significant trough for the nondimensional drift coefficient for system 1 (test 1) is close to T_{L30} for sloshing. This eigenmode is also evident in the RAO for test 1 in figure 68, where the structure experiences a significant amplification in motion around T_{L30}. In addition, at $T \approx 7.5$ seconds in figure 101 there is an increase in the mean drift force, corresponding with eigenmode for sloshing T_{L20}. Correspondingly, the RAO for test 1 in figure 68 is suspect to a cancellation effect, due to sloshing. The opposite behavior of the RAO in the wave-frequency analysis compared to the mean drift force is much likely due to the phase of the dynamic motion and drift force. Here it is assumed that the force is out of face compared to the motion of the system. The same trend can be observed for test $2-4$, in figure 95 to 97. For figure 97 representing test 4, there are two significantly distinct local peaks at $T = 1$ seconds and $T = 4$ seconds respectively. This can possibly be explained by the numerical effect seen for the damping coefficient in figure 74 and 75, due to the singularity of the internal sloshing problem.

As the sloshing phenomenon is highly nonlinear, the effect highlighted in figure 101 has to be considered when using the mean drift force from the simulation. This means that the mean drift force obtained from the different sea states has to be used conservatively, especially when evaluating its effect on the mooring.

From the results in table 18, highlighting the sea state that gives the maximum mean drift force for high and significant exposure, it can be seen that sea state 6 gives the largest force on the structure. The force is fairly similar for all structures ranging from $\approx 90-110$ kN. This is expected due to the similar results for the nondimensional mean drift coefficient. It is also important to notice that the drift force is larger for test 1 (system 1) compared to test 2 (system 2) which is most likely connected to the decreased motion of the system as highlighted in figure 16. This can again be connected to the internal water mass and sloshing, where the different designs experience amplified and decreased motion at different oscillation periods.

It is important to mention that due to the largely varying coefficient, there may be numerical errors when using the coefficient in combination with the different amplitudes in the sea state, using equation 111. It is also worth to mention that test $1-3$ is practically suspect to the same mean drift force as test $5-7$. This is most likely due to the very small motion difference connected to the different mooring systems. It can also be seen that reducing the exposure from high to substantial gives a large reduction in the total mean drift force, due to the significant decrease in T_p and H_s.

Regarding the mean force from current, table 98 shows how the total force change based on the projected area and current speed. Comparing the force from current to the mean drift force, which both leads to a static offset of the system, it is evident that current has a large contribution to the total horizontal contribution. When estimating the current force, the drag coefficient is decided according to uniform drag on a solid sphere. As the drag coefficient has the ability to largely affect the total force, the results are prone to errors due to the interpretation of the drag coefficient, using a solid sphere for the hemispherical and semi ellipsoid shaped designs. Also, due to its nonlinear behavior dependent on the uniform current speed (V_c), reducing or increasing the current exposure has a significant effect on the total force. Due to the assumptions of uniform current and interpretation of the drag coefficient, the drag force needs to be handled with care when used in the mooring system analysis. This means that the results obtained in table 98 should be used conservatively when analyzing the mooring system.

It is also important to mention the elasticity of the membrane which is neglected throughout the analysis. The elasticity is especially important when the water filling level is decreased, leading to a highly deformable bag that has the ability to alter its shape depending on the exposure. This can alter the drag coefficient of the structure largely affecting the motion, damping and forces on the structure. Deformation and its effect on drag forces from current have been investigated in [21], concluding that the forming of a concave surface upstream of the current direction has the ability to increase the drag coefficient substantially as illustrated in figure 102.

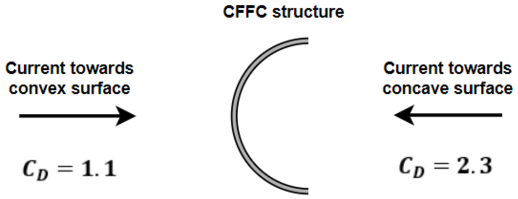

Figure 102: Forming of concave/convex surface and its effect on the drag coefficient

5.3 Mooring system analysis

The mooring system analysis is based on the results from the dynamic and static analysis in the two previous sections. The analysis is force driven, rather than based on the horizontal motion of the system. The mooring system is evaluated based on the force (F_{dyn}) equivalent to the dynamic offset (X_{dyn}) in the dynamic analysis, in addition to the mean wave drift ($F_{1(md\,tot)}$) and current (F_{1c}) force from the static analysis. This is done by following the principle illustrated in figure 7, testing the mooring system integrity when the system is suspected to the maximum force ($F_{x\,tot}$).

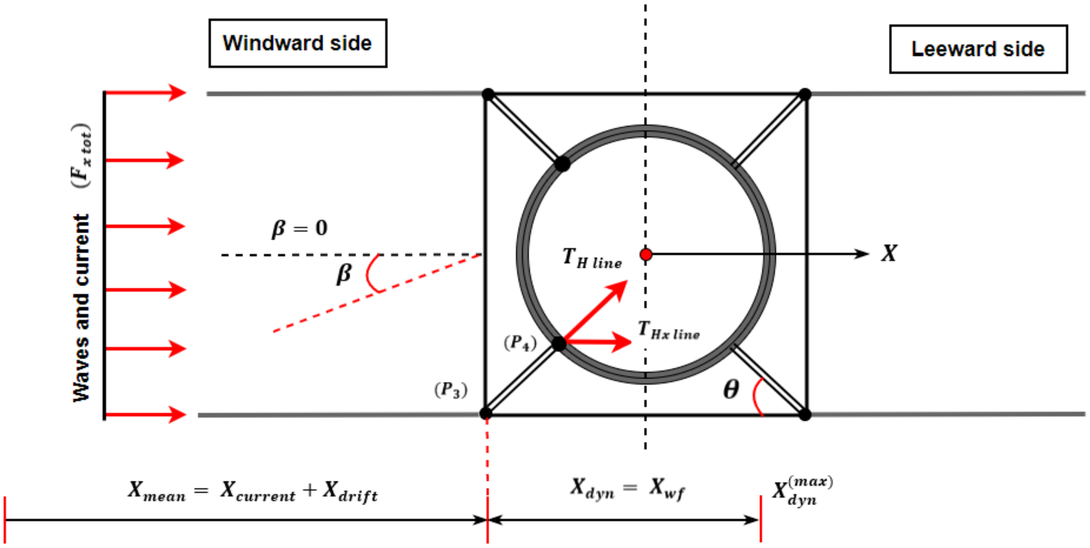

Figure 103: Notation and illustration of mooring system analysis, horizontal plane

Due to the orthogonal layout of the mooring system illustrated in figure 48, and unidirectional waves from $\beta = 0$, one single mooring line on the windward side of the mooring system will be evaluated. This means that half the contribution from mean drift and current forces is absorbed in each mooring line at the windward side of the structure. From the dynamic analysis (X_{dyn}) is used in combination with the mooring system stiffness (K_{11}) relevant for any given mooring system, to find the equivalent force ($F_{x\,tot}$).

$$F_{x\ tot} = F_{dyn} + F_c + F_{(md\,tot)} \tag{126}$$

$$T_{Hx\ line} = \frac{1}{2}(F_c + F_{(md\,tot)}) + F_{dyn\,(l)} + T_{H\ pre} \tag{127}$$

It is important to emphasize that the top connection point (P_4) is assumed to move with the same amplitude as the center of the structure from the WAMIT analysis. In addition, equation 126 and 127 defines the total force from waves and current and the mooring line tension in x-direction for a single mooring line respectively. Here, $F_{dyn\,(l)}$ is the maximum dynamic force in one single mooring line equivalent to the offset (X_{dyn}). The force is obtained from equation 70 using the total stiffness for one single mooring line ($k_{11\,M}$) listed in table 10, in combination with the horizontal offset (X_{dyn}).

The mooring system analysis is conducted for Test 1−7 in table 14, combined with the different sea states in table 15 to obtain X_{dyn} and $F_{1(md\,tot)}$ in table 16 and 18 respectively. In addition, current conditions are evaluated from table 19. Firstly, the sea states giving maximum offset and forces will be evaluated limited to high exposure for waves and substantial exposure for current. Secondly, the sea states limited to substantial exposure for waves will be evaluated.

Throughout the analysis, the anchor line rope component and bridle lines are treated as rigid members when assessing the bottom chain. This means that the horizontal line tension in x-direction ($T_{Hx\,line}$) is assumed to be the same in P_2, P_3 and P_4 with the notation illustrated in figure 103 and 104. This is a reasonable assumption as the rope components of the mooring line have a significantly higher stiffness compared to the bottom chain. Due to the relatively small horizontal extension of the system, it is also assumed that α_1 is constant when the system moves, taken when the system is in its pretensioned state. When evaluating the bridle lines, it is assumed that the angle α_1 = α_2 and that θ illustrated in figure 56 remains constant. This means that the force created by the buoy supporting the connector plate in point P_3 is neglected. In figure 103, $T_{Hx\,pre}$ is the pretension of the system in x-direction.

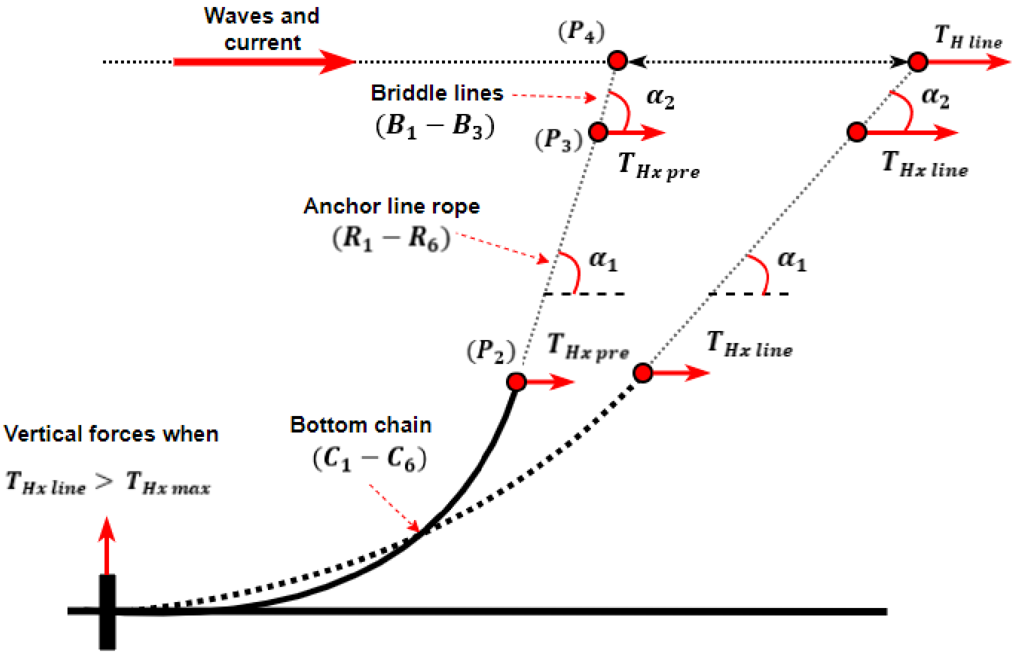

Figure 104: Notation and illustration used in the mooring analysis, vertical plane

,

The bottom chain is evaluated based on the horizontal tension in the connection point P_2 between the chain and the anchor line rope illustrated in figure 55, to see if the tension exceeds operational limits. The operational limit is decided by the nature of the plow anchor used in different mooring systems highlighted in section 3.2.2.

As the anchor is unable to absorb vertical forces, the operational limit is decided according to the active line length (l_s), which has to remain lower than the total length of the bottom chain (L_C) [6]. Here, the maximum force before the entire bottom chain gets active is calculated by manipulating equation 82. This is done by estimating the maximum horizontal tension in x-direction ($T_{Hx\,max}$), setting $l_s = L$ in equation 82 for T_H.

When the maximum horizontal force ($T_{Hx\,max}$) at the instance of activating the entire bottom chain in the water column has been found, the criterion can be compared to the total force ($T_{Hx\,line}$) in the bottom chain. This means that for the bottom chain to fulfill the criterion regarding no vertical forces on the anchor, $T_{Hx\,max} > T_{Hx\,line}$. In addition to evaluating operation limits with regards to vertical forces on the anchor, the bottom chain is evaluated with regards to the breaking strength (MBL) for steel using material and load factors from NS9415 [43].

The anchor line rope is evaluated based on the average line tension in point P_3 illustrated in figure 104, using material and load factors from NS9415 to determine if the line tension is within requirements defined by the Norwegian government. The material properties considered is the Breaking strength (MBL). In addition, the elongation of the supertec 8 rope is considered with regards to the material properties, stated by the supplier Løvold AS [3]. Here it is important to emphasize that the elongation is evaluated solely with respect to the material properties and not when evaluating the complete system illustrated in figure 104. The bridle lines are evaluated in the same manner as the anchor line rope.

Table 20 shows the complete force exerted on the system from test $1-7$. The results are based on information highlighted in table 16 - 19 when the system is suspected to substantial and high wave exposure, and substantial exposure for current (CU 10). Here, $F_{x\,tot}$ and $T_{Hx\,line}$ is defined by equation $126-127$.

Total forces exerted on one windward mooring line and entire system						
Force ID	Test ID	Response ID	Drift ID	$F_{x\,tot}\ [kN]$	$\Delta T_{Hx\,line\,[kN]}$	$T_{Hx\,line}\ [kN]$
High wave exposure, substantial current exposure						
$\boldsymbol{F_1}$	Test 1	XD 1	MD 1	222.1	109.9	144.2
$\boldsymbol{F_2}$	Test 2	XD 2	MD 2	242.4	119.4	153.7
$\boldsymbol{F_3}$	Test 3	RS 3	MD 3	258.6	124.3	251.8
$\boldsymbol{F_4}$	Test 4	XD 4	MD 4	307.7	142.9	270.5
$\boldsymbol{F_5}$	Test 5	XD5	MD 5	229.1	111.5	239.1
$\boldsymbol{F_6}$	Test 6	XD6	MD 6	247.1	120.7	248.2
$\boldsymbol{F_7}$	Test 7	XD 7	MD 7	262.1	125.1	252.7
Substantial wave exposure, substantial current exposure						
$\boldsymbol{F_8}$	Test 1	XD8	MD 8	163.5	80.1	115.3
$\boldsymbol{F_9}$	Test 2	XD 9	MD 9	174.8	86.4	120.8
$\boldsymbol{F_{10}}$	Test 3	XD 10	MD 10	190.2	92.4	219.9
$\boldsymbol{F_{11}}$	Test 4	XD 11	MD 11	211.3	102.1	229.6
$\boldsymbol{F_{12}}$	Test 5	XD 12	MD 12	168.5	82.2	209.7
$\boldsymbol{F_{13}}$	Test 6	XD 13	MD 13	178.4	87.4	214.9
$\boldsymbol{F_{14}}$	Test 7	XD 14	MD 14	192.1	92.8	220.4

Table 20: Total forces exerted on one mooring line

The next subsection uses the results from table 20 in combination with the mooring line particulars to evaluate the integrity of the bottom chain, the anchor line rope and bridle lines for one continuous mooring line. The entire analysis is under the assumptions and using the notation highlighted in this section.

5.3.1 Bottom chain analysis

Table 21 shows relevant data when analyzing the integrity of the bottom chain for test 1−7. The table shows the parameters taken when the system is suspected to maximum conditions limited by high exposure for waves and substantial exposure for current. It also shows the effect of lowering the exposure for waves from high to substantial. All lines are prone to the parameters and properties listed in table 7, with equal line length (L = 110m). The breaking strength of the chain is compared to the in-line tension (T_{line}) with material factor γ_m = 2.0 and load factor γ_l = 1.15. This means that the breaking strength is compared to T_{des} which is the design load when accounting for the load and material factor [22]. All factors have been chosen according to NS9415 [43]. Equation 128 shows the relation between T_{line} and T_{des}.

$$T_{des} = T_{line} \cdot \gamma_m \cdot \gamma_l \tag{128}$$

α_1 is taken when the system is in its pretensioned state, further used to estimate the inline tension (T_{line}) from its geometric relation to ($T_{Hx\,line}$). As seen from table 8, α_1 is close to equal for every mooring system setup. Due to this, α_1 = 25 ° has been set as a constant when estimating (T_{line}).

Bottom chain analysis							
	Chain	Force	$T_{Hx\,line}$	$T_{Hx\,max}\,[kN]$	$T_{des}\,[kN]$	$T_{real}\,[kN]$	$MBL\,[kN]$
High wave exposure, substantial current exposure							
Test 1	C_1	F_1	144.2	**126.9**	159.1	365.9	**812**
Test 2	C_3	F_2	153.7	**361.9**	169.6	390.1	**1370**
Test 3	C_5	F_3	251.8	**440.3**	277.8	639.1	**981**
Test 4	C_6	F_4	270.5	**600.8**	298.5	686.5	**1370**
Test 5	C_4	F_5	239.1	**382.5**	263.8	606.8	**812**
Test 6	C_5	F_6	248.2	**440.3**	273.9	629.9	**981**
Test 7	C_6	F_7	252.7	**600.8**	278.8	641.3	**1370**
Substantial wave exposure, substantial current exposure							
Test 1	C_1	F_8	115.3	**126.9**	127.2	292.6	**812**
Test 2	C_3	F_9	120.8	**361.9**	133.3	306.6	**1370**
Test 3	C_5	F_{10}	219.9	**440.3**	242.6	558.1	**981**
Test 4	C_6	F_{11}	229.6	**600.8**	253.3	582.7	**1370**
Test 5	C_4	F_{12}	209.7	**382.5**	231.4	532.2	**812**
Test 6	C_5	F_{13}	214.9	**440.3**	237.1	545.4	**981**
Test 7	C_6	F_{14}	220.4	**600.8**	243.2	559.3	**1370**

Table 21: Bottom chain integrity analysis

5.3.2 Anchor line analysis

Table 22 shows the relevant data when analyzing the integrity of the anchor line rope for Test $1-7$. The material factor used when evaluating the integrity of the anchor line rope has been set to γ_m = 3.0 and the load factor γ_m = 1.15, according to NS9415 [43]. As for the bottom chain equation 128 is used to obtain T_{des}, used when comparing the in-line tension to the breaking strength of the material.

$$\Delta L = T_{line} \cdot \frac{L_0}{A_0 E} \qquad \% EL = \frac{\Delta L}{L_0} \tag{129}$$

In addition, the elongation of the rope component is considered from equation 129. As the anchor line rope is of the supertec 8 type it has the ability to elongate 20% according to Løvold AS. The anchor line parameters is highlighted in table 8. Since L_R is the length of the mooring line when the system is already is in its pretensioned state, the table also includes the original length of the mooring line when suspected to zero tension (L_0). This is to be able to evaluate if the anchor line component stretches beyond the 20% criterion from the zero tension state, when the system is suspected to T_{line}. The zero tension length (L_0) is found from manipulating equation 129 setting ($L_0 + \Delta L = L_R$) with tension T_{pre}.

Anchor line rope analysis							
	Rope ID	Force ID	$T_{des}\,[kN]$	$MBL\,[kN]$	$L_0\,[m]$	$\Delta L_R[m]$	$\%EL$
High wave exposure, Substantial current exposure							
Test 1	R_1	F_1	548.9	**637**	184.6	5.97	**3.23**%
Test 2	R_3	F_2	658.5	**1034**	191.1	3.98	**2.08**%
Test 3	R_5	F_3	958.5	**823**	187.3	8.31	**4.43**%
Test 4	R_6	F_4	1029.7	**1034**	195.3	7.16	**3.66**%
Test 5	R_4	F_5	910.2	**637**	183.0	9.80	**5.36**%
Test 6	R_5	F_6	944.8	**823**	187.3	8.19	**4.37**%
Test 7	R_6	F_7	961.9	**1034**	195.3	6.69	**3.42**%
Substantial wave exposure, Substantial current exposure							
Test 1	R_1	F_8	438.9	**637**	184.6	4.77	**2.58**%
Test 2	R_3	F_9	459.8	**1034**	191.1	3.13	**1.64**%
Test 3	R_5	F_{10}	837.1	**823**	187.3	7.26	**3.88**%
Test 4	R_6	F_{11}	874.0	**1034**	195.3	6.08	**3.11**%
Test 5	R_4	F_{12}	798.3	**637**	183.0	8.60	**4.70**%
Test 6	R_5	F_{13}	818.0	**823**	187.3	7.09	**3.78**%
Test 7	R_6	F_{14}	839.0	**1034**	195.3	5.83	**2.99**%

Table 22: Anchor line rope integrity analysis

5.3.3 Bridle line analysis

Table 23 shows the relevant data when analyzing the integrity of the bridle lines for test $1-7$. The bridle lines are suspect to the same method when analyzing one single bridle line, as the anchor line rope component. Here, it is important to mention that one complete mooring line consists of two bridle lines as illustrated in figure 103.

When analyzing the bridle lines, one single line will be evaluated. Due to the layout and geometry illustrated in figure 103, the force from environmental effects in one line is assumed to be absorbed equally between the two lines connecting P_3 to the top side connection point P_4 on the structure. It is also important to remember that the line is shifted both in the vertical and horizontal plane relative to the x-axis when finding the inline tension T_{lineB}. This is illustrated in figure 21. Equation 130 shows the relation between the inline tension of the anchor and bottom chain component (T_{line}) compared to the inline tension of one bridle line (T_{lineB}).

$$T_{lineB} = \frac{T_{line}}{2 \cdot \cos\theta} \tag{130}$$

The material factors used when estimating T_{des} is the same as for the anchor line rope. When evaluating the elongation of the line length has been set to $L_B = 37.6m$ as defined in figure 55. According to Løvold AS the supertec 3 rope has the ability to elongate 20% of their original length when the rope is suspected to zero tension.

Bridle line analysis							
	Bridle ID	Force ID	$T_{line\,B}\,[kN]$	$T_{des\,B}\,[kN]$	$MBL\,[kN]$	$\Delta L_B[m]$	$\%EL$
High wave exposure, Substantial current exposure							
Test 1	B_1	F_1	112.5	388.1	**416.9**	1.15	**3.06%**
Test 2	B_3	F_2	119.9	413.7	**613.1**	0.79	**2.10%**
Test 3	B_2	F_3	196.4	677.8	**543.5**	1.44	**3.84%**
Test 4	B_3	F_4	211.0	728.1	**613.1**	1.35	**3.60%**
Test 5	B_1	F_5	186.5	643.6	**416.9**	1.84	**4.66%**
Test 6	B_2	F_6	193.6	668.1	**543.5**	1.42	**3.78%**
Test 7	B_3	F_7	197.2	680.2	**613.1**	1.27	**3.37%**
Substantial wave exposure, Substantial current exposure							
Test 1	B_1	F_8	89.9	310.4	**416.9**	0.92	**2.45%**
Test 2	B_3	F_9	94.2	325.2	**613.1**	0.62	**1.65%**
Test 3	B_2	F_{10}	171.6	591.9	**543.5**	1.26	**3.35%**
Test 4	B_3	F_{11}	179.1	618.0	**613.1**	1.15	**3.06%**
Test 5	B_1	F_{12}	163.6	564.5	**416.9**	1.61	**4.28%**
Test 6	B_2	F_{13}	167.7	578.4	**543.5**	1.23	**3.27%**
Test 7	B_3	F_{14}	172.0	593.3	**613.1**	1.10	**2.94%**

Table 23: Bridle line integrity analysis

5.3.4 Discussion - Mooring system analysis

This section aims to shortly discuss the results from the mooring system analysis, and qualitatively assess the importance of second-order slowly varying drift forces, due to its importance for the mooring system integrity.

Treating the exposure uniformly in the horizontal plane according to NS9415 with maximum conditions limited to high exposure is considered a conservative assumption, as waves and current affect one side of the structure with maximum effect. However, bidirectional waves have not been considered when accounting for mean drift forces and wave frequency motion, which could lead to larger strain on the mooring system.

The analysis is force-driven, using the horizontal offset from the dynamic analysis to calculate an equivalent dynamic force, combined with the mean wave drift and force from current at the top side connection point of one single mooring line. The dynamic force ($F_{dyn\,(l)}$) in one mooring line is calculated based on the horizontal offset (X_{max}) and the mooring line stiffness (k_{11}). Calculating the dynamic force using the stiffness when the bottom chain is in its pretensioned state could be considered non-conservative. If the stiffness was modeled in a higher tension state, the force from the dynamic motion would be larger, leading to a more conservative approach. This is due to the small effect of mooring line stiffness in the wave frequency regime, meaning that the RAO for test $1-7$ would stay close to unchanged when modeling the bottom chain stiffness differently in the user-specified stiffness in WAMIT. However, as the dynamic contribution to the total force is very small, this effect is assumed to be minimal.

From table 20 highlighting the total force exerted on the system in x-direction, it can be seen that the force gets increasingly larger for system 1 to 4 (test 1 to 4). This is mainly due to the force from current, which is highly dependent on the projected area, getting increasingly larger for structure $1-4$. It can also be seen that system $5-7$ (test $5-7$) almost matches system $1-3$ respectively. This is expected from the results in the dynamic and static analysis, where the mooring system is the only parameter separating the systems. The large effect from current forces means that there is large uncertainty tied to the assumption of uniform current, which may be over conservative.

From table 21 highlighting the bottom chain analysis for test $1-7$, it can be seen that system 1 is the only system where $T_{Hx\,line} > T_{Hx\,max}$ for high wave exposure, meaning that the anchor gets suspected to vertical forces. This can be accounted for by simply adding more clump weights to the bottom chain, or changing the anchor solution to a bolt or suction anchor. Comparing the design load to the MBL of the different chain's it can be seen that all systems are within the requirements specified by NS9415, including the material and load factor for steel components [43].

From table 22 highlighting the anchor line rope analysis, the results indicate that the design load (T_{des}) for system 3, 5, 6 (test 3, 5, 6) exceed the breaking strength of the anchor line rope. This simply means that to maintain the classification of the system limited to high exposure, the anchor line rope needs to be upgraded. Here it is important to emphasize that using the design load (T_{des}) could be overly conservative based on the large material and load factor. Again, this depends on the accuracy from the dynamic and static analysis and the conservatism of the different assumptions made throughout the process.

The bridle line analysis highlighted in table 23 follows the same trend as the results for the anchor line rope. This means that when using the design inline tension (T_{des}) system 3, 4, 5, 6, 7 (test 3, 4, 5, 6, 7) fails to fulfill the dimensional criterion decided by NS9415 when the system is suspected to high exposure for waves and substantial exposure for current. For the bridles it can also be seen that the design load exceeds the breaking load when the exposure is lowered to substantial wave exposure for several systems. This could be solved by exchanging the supertec 3 rope components with the more robust supertec 8 option. Through the analysis, it can also be seen that the elongation of the anchor and bridle lines fulfills the elongation criterion in all test instances according to Løvold AS [3]. Here, the tension used to calculate the elongation is the tension without accounting for the load and material factor. In addition to forces induced by first-order motion, mean drift and current, it is important to consider how the simplifications and assumptions have the possibility to affect the integrity of the system. Here, second-order loads in the form of sum-frequency and difference-frequency effects have to be mentioned, originating from interaction between waves in the irregular sea state.

The sum frequency forces, also known as high-frequency forces, mainly has the ability to affect vertical motion due to its high-frequency oscillation. This means that it mainly affects motion in heave, roll and pitch. Regarding the horizontal motion of the system, critical for the mooring system, slowly varying effects has the ability to significantly amplify the motion of the system if the eigenperiod in surge/sway coincides with the mean oscillation period of the force [11]. Looking at the physical origin of the slowly varying force, arising due to interaction between different waves in the irregular sea state, the force is subject to large oscillation periods ($\omega_2 - \omega_1$). As highlighted in table 13 and figure 80−80, the eigenperiods of system 1−7 in surge varies between $T_{1n} \approx$ 270−430 seconds, increasing the importance of considering slowly varying effects.

To be able to roughly compare the eigenperiods to slowly varying forces, experimental results from the SJØFLO project can be used to qualitatively evaluate their significance for the designs investigated in this thesis. The experimental test was performed for a flexible hemispherical structure with $D = 2H$ = 0.75 meter denoted as model $K51$ in [8], which coincides very well with design 1 investigated in this paper when using λ_f = 27. In the experiment, the sea state was represented by a JONSWAP spectrum with γ = 3.81, H_s = 1.5 meters and T_p = 4,7 seconds. Figure 105 shows the results from the experiment, where the period of the slowly varying force can be interpreted from the windward and leeward mooring line tension.

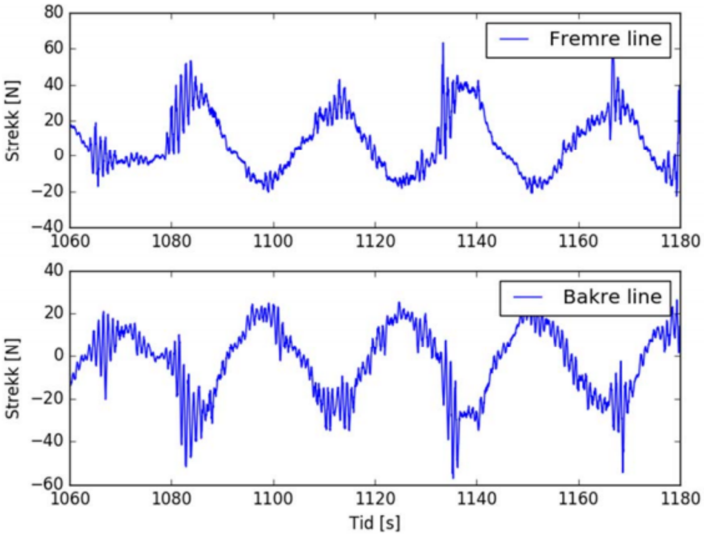

Figure 105: Windward and leeward mooring line tension when investigating slowly varying forces [8]

From the experiment, it was found that the slowly varying force had a oscillation period of T_{sv} = 28 seconds in model scale, which is equivalent to T_{sv} = 145 seconds in full scale using λ_f = 27. Here it is important to highlight that the JONSWAP spectrum used in the SJØFLO project is more narrow, with its energy more focused around certain wave frequencies, while the PM-spectrum used for the sea states in table 15, has a wider distribution of energy over a larger set of wave frequencies [10]. It is also important to notice that the JONSWAP spectrum used in the SJØFLO project has T_p = 4.7 seconds and H_s = 1.5 meters, while the sea states investigated in the mooring system analysis uses a PM-spectrum with T_p = 6.7 / 5.0 seconds and H_s = 3.0 / 2.0 meters.

From figure 106 it can be seen how the shape of the JONSWAP spectrum with γ = 3.0 change as T_p gets increasingly larger. This can be used to qualitatively estimated the effect from the larger sea states evaluated in this paper, compared to the results from the SJØFLO project.

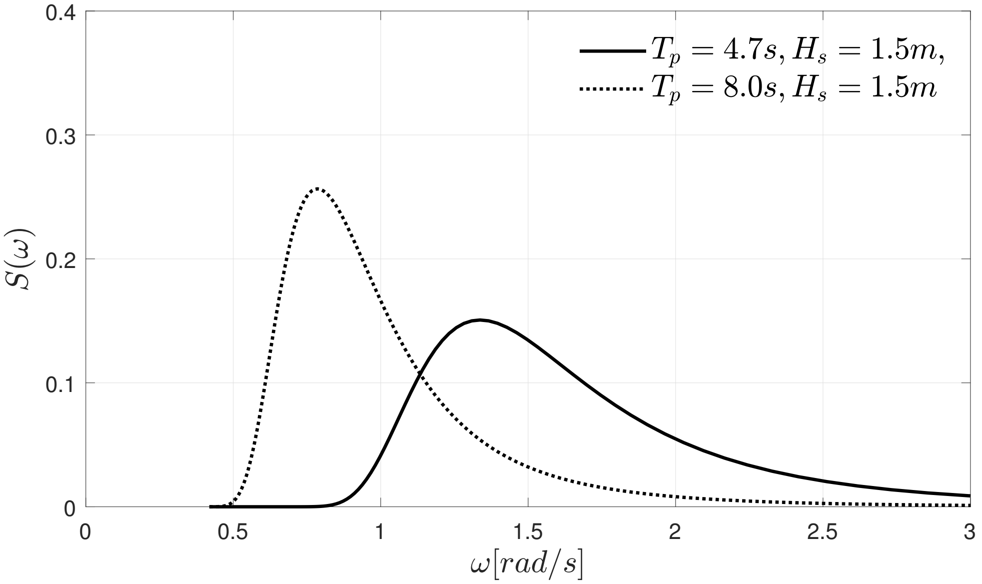

Figure 106: Comparison of spectral shape for JONSWAP spectrum with different T_p, γ = 3.3

The figure clearly shows that increasing T_p leads to a larger spectral peak and that the energy gets more focused around the T_p area. From the interpretation of the slow drift force, this means that relevant spectral energy able to excite the structure will be found at a finer increment of $\omega_2 - \omega_1$. This means that the relevant period of the slowly varying force will increase when T_p increases.

From personal communication with professor Sverre Steen, Head of Department of Marine Technology NTNU, the peak period can be used directly when scaling the mean period of the slowly varying force in a qualitative approach. In addition to the influence of the peak period, larger H_s will also affect the spectral shape. This can be seen from figure 107, illustrating the ratio between the spectrum in the SJØFLO project compared to the PM-spectrums investigated in this paper.

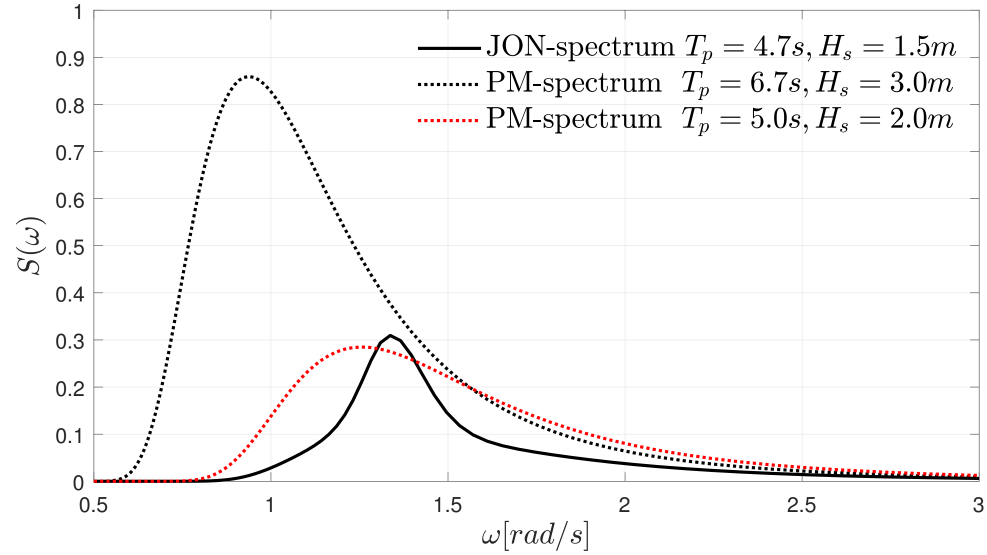

Figure 107: The JONSWAP spectrum from the *SJØFLO* investigation, and the PM-spectrum for High and significant exposure investigated in this paper

Figure 107 shows that sea state 6 representing high exposure according to NS9415 has a significantly larger spectrum compared to the JONSWAP spectrum used in the SJØFLO project. This means that relevant energy able to excite the structure from slowly varying effects will have a larger mean period compared to the sea state and model in the SJØFLO investigation. With T_p = 4.7 seconds from the SJØFLO investigation and T_p = 6.7 seconds equivalent to high exposure in this paper, the ratio used to scale the mean period of the drift force becomes $6.7 : 4.7$ = 1.42. From this qualitative approach, the slowly varying forces from sea state 6 may have relevant oscillation periods up to T_{sv} = 206 seconds. Evaluating sea state 4, figure 107 shows that the JONSWAP spectrum has more narrow distribution of energy, but that the peak period is very similar. This means that more energy will be connected to a small increment of $\delta\omega$ around the peak period for the JONSWAP spectrum, but making a qualitative estimation of the difference becomes difficult.

Using the information from the qualitative approach together with the eigenperiod of the different systems in the pretensioned state, ranging from $T_{1n} \approx$ 270−430 seconds, it can be seen that T_{sv} = 206 seconds < T_{1n}. Interpreting the results should be done with upmost caution, as the evaluation is purely based on a qualitative approach. This means that ignoring the slowly varying drift force when assessing the mooring system is a highly non-conservative approach.

In addition to the slowly varying forces, vertical and angular motions have not been investigated, which can be important for the overall integrity, but especially with regards to mooring system fatigue. This leads to forces and motions used in the analysis to be even less conservative. On the other hand, material and load factors can be considered to be relatively high, ranging from γ_m = 2.0-3.0 and γ_l = 1.15 when finding the design load, making up for some of the uncertainty.

6 Conclusion

The simulation software WAMIT based on linear theory and the BIEM low order panel method, has been used to numerically estimate wave forces on four different CFFC structures, treated as rigid bodies neglecting the elasticity of the membrane. The analysis is limited to wave frequency motion and second-order mean drift forces. To obtain relevant data for the mooring system analysis, RAO's from the dynamic analysis have been combined with sea states limited to high and substantial wave exposure, estimating the most probable maximum offset of the systems for surge motion. Mean drift effects in surge have been found as the total mean drift force from the different sea states. Current has been calculated based on Morison's equation. From this, the total force exerted by waves and current has been used to analyze the integrity of one single mooring line in the orthogonal mooring system.

The internal sloshing problem has been investigated in the dynamic and static analysis in WAMIT, responding well with recognized literature when interpreting the outcome from the different tests. In addition, similar investigations confirm that the results from the static and dynamic analysis give realistic results for the different simulations.

The results from the dynamic, static and mooring system analysis indicate overall concern for the different systems investigated. The line tension induced by waves and current in the top point of the mooring lines facing the incoming environmental effects is either in the vicinity or exceeding the material properties for the different components in the mooring system. From the results, it can be seen that the anchor and bridle line rope poses the greatest threat to the integrity of the system. This is highlighted by the design load exceeding the MBL of the material in several cases. By reducing the exposure from high to substantial, the difference between MBL and the inline tension significantly improves the integrity of the anchor line rope, but the bridles are still exposed to possible fracture. This means that the bridles should be exchanged from Supertec 3 to Supertec 8, or improved in other ways.

Modeling the stiffness from the bottom chain and damping from viscous effects linearly makes the analysis suspect to large uncertainty, especially when evaluating the mooring system integrity. In addition, the mooring system analysis has been carried out from solely evaluating the top side tension in one mooring line, neglecting the elasticity of the rope components. This further increases the uncertainty of nonlinear effects. There is also uncertainty tied to nonlinear effects such as slowly varying drift forces and varying current. The design load is calculated based on load and material factors specified by NS9415, suspect to large conservatism. From a sole qualitative perspective, this means that some of the uncertainty can be justified by the large material and load factors used in the mooring system analysis. However, this makes it increasingly hard to evaluate the integrity of the analysis as a whole.

Overall, it is evident that the mooring system should be investigated more closely using numerical software considering nonlinear effects. In addition, more attention to the elasticity of the bag, and its effect on mooring system should be carried out in future work. Here, the WAMIT files containing the geometry of the structure, MATLAB codes to interpret nondimensional coefficients and RAO's is valuable when further evaluating the system.

7 Further work

This section highlights further work that is necessary for an improved analysis of the mooring system and system components. The WAMIT data and MATLAB plots obtained for the different structures investigated in this paper, including the geometry file will be provided by request if the work is continued.

- Use simulation tools such as SIMO (*Simulations of complex marine operations*) or similar software, to account for second-order effects from wave and current, including non-linear damping and mooring line stiffness contributions.
- Investigate membrane elasticity and its possible effect on structure response and integrity.
- Use real time wave and current data for fish farm locations relevant for implementing closed technology.
- Analyze a fish farm facility consisting of several CFFC's connected in one continuous mooring grid.
- Investigate relative motion between several CFFC's connected in one continuous mooring grid.
- Investigate Different mooring system layouts used by the aquaculture industry, relevant for closed technology.
- Use real time location data for fish farm locations relevant for implementing closed technology.
- Investigate motion in vertical and angular motion, and its effect on mooring system fatigue and integrity.
- Investigate Snap loads caused by negative tension in the fabric relevant for fatigue in mooring and membrane components.
- Further investigate sloshing modes for different geometrical shapes relevant for closed fish farm technology.

Appendix A Critical damping and damping ratio

Critical damping and damping ratio							
Mooring		$\boldsymbol{M_1}$	$\boldsymbol{M_2}$	$\boldsymbol{M_3}$	$\boldsymbol{M_4}$	$\boldsymbol{M_5}$	$\boldsymbol{M_6}$
Tension (T_{Hp})	$[kN/m]$	5.53	6.70	9.17	14.40	16.45	19.30
Design 1							
Critical ($B^{(cr)}$)	$[kg/s]$	$0.75 \cdot 10^6$	$0.83 \cdot 10^6$	$0.97 \cdot 10^6$	$1.22 \cdot 10^6$	$1.30 \cdot 10^6$	$1.41 \cdot 10^6$
Ratio (ζ)		**10.38 %**	**9.43 %**	**8.06 %**	**6.43 %**	**6.02 %**	**5.56 %**
Design 2							
Critical ($B^{(cr)}$)	$[kg/s]$	$0.84 \cdot 10^6$	$0.935 \cdot 10^6$	$1.09 \cdot 10^6$	$1.36 \cdot 10^6$	$1.45 \cdot 10^6$	$1.57 \cdot 10^6$
Ratio (ζ)		**11.59 %**	**10.53 %**	**9.00 %**	**7.18 %**	**6.72 %**	**6.20 %**
Design 3							
Critical ($B^{(cr)}$)	$[kg/s]$	$0.88 \cdot 10^6$	$0.97 \cdot 10^6$	$1.13 \cdot 10^6$	$1.42 \cdot 10^6$	$1.52 \cdot 10^6$	$1.65 \cdot 10^6$
Ratio (ζ)		**12.13 %**	**11.02 %**	**9.42 %**	**7.52 %**	**7.04 %**	**6.50 %**
Design 4							
Critical ($B^{(cr)}$)	$[kg/s]$	$0.92 \cdot 10^6$	$1.02 \cdot 10^6$	$1.19 \cdot 10^6$	$1.49 \cdot 10^6$	$1.59 \cdot 10^6$	$1.73 \cdot 10^6$
Ratio (ζ)		**13.25 %**	**12.03 %**	**10.30 %**	**8.21 %**	**7.68 %**	**7.09 %**
Tension (T_{H1})	$[kN/m]$	9.22	11.26	15.23	19.49	22.78	26.78
Design 1							
Critical ($B^{(cr)}$)	$[kg/s]$	$97 \cdot 10^6$	$1.08 \cdot 10^6$	$1.25 \cdot 10^6$	$1.41 \cdot 10^6$	$1.53 \cdot 10^6$	$1.66 \cdot 10^6$
Ratio (ζ)		**8.04%**	**7.27%**	**6.25%**	**5.53%**	**5.11%**	**4.71%**
Design 2							
Critical ($B^{(cr)}$)	$[kg/s]$	$1.09 \cdot 10^6$	$1.20 \cdot 10^6$	$1.40 \cdot 10^6$	$1.58 \cdot 10^6$	$1.71 \cdot 10^6$	$1.86 \cdot 10^6$
Ratio (ζ)		**8.98 %**	**8.12 %**	**6.98 %**	**6.17 %**	**5.71 %**	**5.27 %**
Design 3							
Critical ($B^{(cr)}$)	$[kg/s]$	$1.14 \cdot 10^6$	$1.26 \cdot 10^6$	$1.46 \cdot 10^6$	$1.66 \cdot 10^6$	$1.79 \cdot 10^6$	$1.95 \cdot 10^6$
Ratio (ζ)		**9.40 %**	**8.50 %**	**7.31 %**	**6.47 %**	**5.98 %**	**5.51 %**
Design 4							
Critical ($B^{(cr)}$)	$[kg/s]$	$1.19 \cdot 10^6$	$1.32 \cdot 10^6$	$1.53 \cdot 10^6$	$1.73 \cdot 10^6$	$1.87 \cdot 10^6$	$2.03 \cdot 10^6$
Ratio (ζ)		**10.26 %**	**9.28 %**	**7.98 %**	**7.05 %**	**6.53 %**	**6.02 %**

Table 24: Damping relative to the critical damping including damping ratio from decay test

Appendix B MATLAB code - geometry file WAMIT

```
%% GEOMETRIPLOT FOR DESIGN 1,2,3,4
n = 20;                    %antall noder
k = n-1;                   %antall noder
q = 4;                     %antall noder
f= q-1;                    %antall noder
Twall = 0.01;     %[m]     %Tykkelsen på membranen 1cm

%MEMBRAN DIMMENSJONER
D1 = 40;              %[m]
H1 = 20;              %[m]
R1 = (D1/2);          %[m]
O1 = pi()*D1;         %[m]
AREA_M = pi()*H1*R1;  %(m2)

%TANK DIMMENSJONER
D2 = D1-2*Twall;  %[m]
H2 = H1-Twall;    %[m]
R2 = (D2/2);      %[m]
O2 = pi()*D2;     %[m]
D_F = 1.0;        %[m]

%KRAGE 1 DIMMENSONER
R_krage1 = D_F/2;                %[m]
R_torus1 = R1 + R_krage1;        %[m]

%KRAGE 2 YTTERSTE FLYTERØR
R_krage2 = D_F/2;                %[m]
R_torus2 = R1 + D_F + R_krage2;  %[m]

%VINKLER FOR SPHÆRISKE OF TORUS KOORDINATER
theta = linspace(2*pi,0,n);                 %[rad]
phi =  linspace(-pi()/2,-pi(),n);           %[rad]
theta_torus = linspace(0,-pi(),q);              %[rad]
phi_torus = linspace(2*pi()+pi(),pi(),n); %[rad]

%PLOT AV MEMBRAN I KONSTUKSJONEN OG MATRISEFIL TIL WAMIT
X1 = R1.*sin(phi).'*cos(theta);   %x-koordinater membran
Y1 = R1.*sin(phi).'*sin(theta);   %y-koordinater membran
Z1 = meshgrid(H1.*cos(phi))';     %z-koordinater membran

for t=1:k          %antall paneler i hver ring mellom to z-verdier -1
   for p=1:k       %antall ringer med paneler mellom to z-verdier -1

    m1_X1 = [X1(1:t,1:p)]';       %Hjørne 1 koordinater for membran
```

```
     m1_Y1 = [Y1(1:t,1:p)]';
     m1_Z1 = [Z1(1:t,1:p)]';

     m2_X1 = [X1(1:t,2:p+1)]';     %Hjørne 2 koordinater for membran
     m2_Y1 = [Y1(1:t,2:p+1)]';
     m2_Z1 = [Z1(1:t,2:p+1)]';

     m3_X1 = [X1(2:t+1,2:p+1)]';   %Hjørne 3 koordinater for membran
     m3_Y1 = [Y1(2:t+1,2:p+1)]';
     m3_Z1 = [Z1(2:t+1,2:p+1)]';

     m4_X1 = [X1(2:t+1,1:p)]';     %Hjørne 4 koordinater for membran
     m4_Y1 = [Y1(2:t+1,1:p)]';
     m4_Z1 = [Z1(2:t+1,1:p)]';
    end
end
mesh(X1,Y1,Z1);
hold on;

%PLOT AV TANK PÅ INNSIDEN AV MEMBRANEN OG MATRISEFIL TIL WAMIT
X2 = R2.*sin(phi).'*cos(theta);  %x-koordinater membran
Y2 = R2.*sin(phi).'*sin(theta);  %y-koordinater membran
Z2 = meshgrid(H2.*cos(phi))';    %z-koordinater membran

for t=1:k        %antall paneler i hver ring mellom to z-verdier -1
    for p=1:k    %antall ringer med paneler mellom to z-verdier -1

     m1_X2 = [X2(1:t,fliplr(2:p+1))]';     %Hjørne 1 koordinater for tank
     m1_Y2 = [Y2(1:t,fliplr(2:p+1))]';
     m1_Z2 = [Z2(1:t,fliplr(2:p+1))]';

     m2_X2 = [X2(1:t,fliplr(1:p))]';       %Hjørne 2 koordinater for tank
     m2_Y2 = [Y2(1:t,fliplr(1:p))]';
     m2_Z2 = [Z2(1:t,fliplr(1:p))]';

     m3_X2 = [X2(2:t+1,fliplr(1:p))]';     %Hjørne 3 koordinater for tank
     m3_Y2 = [Y2(2:t+1,fliplr(1:p))]';
     m3_Z2 = [Z2(2:t+1,fliplr(1:p))]';

     m4_X2 = [X2(2:t+1,fliplr(2:p+1))]';   %Hjørne 4 koordinater for tank
     m4_Y2 = [Y2(2:t+1,fliplr(2:p+1))]';
     m4_Z2 = [Z2(2:t+1,fliplr(2:p+1))]';

    end
end
mesh(X2,Y2,Z2);
```

```
hold on;

%PLOT AV FLYTEKRAGE1 OG MATRISEFIL TIL WAMIT
[theta_torus, phi_torus] = meshgrid(theta_torus,phi_torus);
X3 = (R_torus1 + R_krage1.*cos(theta_torus)).*cos(phi_torus);
Y3 = (R_torus1 + R_krage1.*cos(theta_torus)).*sin(phi_torus);
Z3 = (R_krage1.*sin(theta_torus));

for t=1:k          %antall paneler -1
    for p=1:f      %antall paneler -1

     m1_X3 = [X3(1:t,1:p)];      %Hjørne 1 koordinater
     m1_Y3 = [Y3(1:t,1:p)];
     m1_Z3 = [Z3(1:t,1:p)];

     m2_X3 = [X3(2:t+1,1:p)];    %Hjørne 2 koordinater
     m2_Y3 = [Y3(2:t+1,1:p)];
     m2_Z3 = [Z3(2:t+1,1:p)];

     m3_X3 = [X3(2:t+1,2:p+1)];   %Hjørne 3 koordinater
     m3_Y3 = [Y3(2:t+1,2:p+1)];
     m3_Z3 = [Z3(2:t+1,2:p+1)];

     m4_X3 = [X3(1:t,2:p+1)];    %Hjørne 4 koordinater
     m4_Y3 = [Y3(1:t,2:p+1)];
     m4_Z3 = [Z3(1:t,2:p+1)];
    end
end
mesh(X3,Y3,Z3)
xlabel('X','FontSize',10);
ylabel('Y','FontSize',10);
zlabel('Z','FontSize',10);
colormap([0 0 0]);
axis equal;
grid off;
hold on

%PLOT AV FLYTEKRAGE2 PÅ OG MATRISEFIL TIL WAMIT
X4 = (R_torus2 + R_krage2.*cos(theta_torus)).*cos(phi_torus);
Y4 = (R_torus2 + R_krage2.*cos(theta_torus)).*sin(phi_torus);
Z4 = (R_krage2.*sin(theta_torus));

for t=1:k              %antall paneler -1
    for p=1:f          %antall paneler -1

     m1_X4 = [X4(1:t,1:p)];       %Hjørne 1 koordinater
```

```
    m1_Y4 = [Y4(1:t,1:p)];
    m1_Z4 = [Z4(1:t,1:p)];

    m2_X4 = [X4(2:t+1,1:p)];    %Hjørne 2 koordinater
    m2_Y4 = [Y4(2:t+1,1:p)];
    m2_Z4 = [Z4(2:t+1,1:p)];

    m3_X4 = [X4(2:t+1,2:p+1)];  %Hjørne 3 koordinater
    m3_Y4 = [Y4(2:t+1,2:p+1)];
    m3_Z4 = [Z4(2:t+1,2:p+1)];

    m4_X4 = [X4(1:t,2:p+1)];    %Hjørne 4 koordinater
    m4_Y4 = [Y4(1:t,2:p+1)];
    m4_Z4 = [Z4(1:t,2:p+1)];
  end
end
mesh(X4,Y4,Z4)
xlabel('X','FontSize',10);
ylabel('Y','FontSize',10);
zlabel('Z','FontSize',10);
colormap([0 0 0]);
axis equal;
grid off;

M_Membran = [m1_X1(:) m1_Y1(:) m1_Z1(:) m2_X1(:) m2_Y1(:) m2_Z1(:) ...
    m3_X1(:) m3_Y1(:) m3_Z1(:) m4_X1(:) m4_Y1(:) m4_Z1(:)];
M_tank = [m1_X2(:) m1_Y2(:) m1_Z2(:) m2_X2(:) m2_Y2(:) m2_Z2(:) ...
    m3_X2(:) m3_Y2(:) m3_Z2(:) m4_X2(:) m4_Y2(:)  m4_Z2(:)];
M_krage1 = [m1_X3(:) m1_Y3(:) m1_Z3(:) m2_X3(:) m2_Y3(:) m2_Z3(:) ...
    m3_X3(:) m3_Y3(:) m3_Z3(:)  m4_X3(:) m4_Y3(:) m4_Z3(:)];
M_krage2 = [m1_X4(:) m1_Y4(:) m1_Z4(:) m2_X4(:) m2_Y4(:) m2_Z4(:) ...
    m3_X4(:) m3_Y4(:) m3_Z4(:)  m4_X4(:) m4_Y4(:) m4_Z4(:)];
```

Appendix C MATLAB code - Dynamic motion

```
%%PLOT USING RAO FROM WAMIT AND IRREGULAR SEASTATE TO GET Xmax

%PARAMETERS REPRESENTING THE DIFFERENT SEASTATES
T=[0.5:0.1:15];              %[s]      %wave periods
g = 9.81;                    %[m/s^2]  %Acceleration of gravity
omega = fliplr(2*pi()./T)    %[rad/s]  %wave frequency
del_omega = diff(omega)      %[rad/s]  %delta omega
del_omega = [del_omega(1) del_omega];  %[rad/s] %delta omega
h = 100;                               %[m]     %Water-depth
t = 10800;                        %[s]          %Seastate duration

T_p = [2.0 3.0 4.0 5.0 6.0 6.7];       %[s]
H_s = [0.5 1.0 1.5 2.0 2.5 3.0];       %[m]
T_Z = T_p/1.4049;                      %[s]
N = t./T_Z;
omega_p = 2*pi()./T_p;                 %[rad/s]

n = 4;           %Counter used when reading RAO from WAMIT to MATLAB
k = 6;           %Counter used to denote seasate

S_omega_DNV = (5/16)*H_s(k)^2*omega_p(k)...
    ^4.*omega.^(-5).*exp(-(5/4).*(omega./omega_p(k)).^(-4));
S_integral = trapz(omega,S_omega_DNV);
S_omega = ((H_s(k).^2)/16).*(1/S_integral).*S_omega_DNV;   %[M^2/rad/s]
Hs = 4*sqrt(trapz(omega,S_omega))                           %[m]

%RAO DATA FROM WAMIT TO MATLAB
fid1= fopen([]);
fgetl(fid1);
data1 = textscan(fid1,'%f %f %d %f %f %f %f');
fclose(fid1);

%RAO VECTOR FROM WAMIT TO MATLAB
RAO_all_surge = cell2mat(data1(n));
RAO_surge = RAO_all_surge(1:6:end)';
RAO_surge_flip = fliplr(RAO_surge);   %Adapting vector

Sx_surge = RAO_surge_flip.^2.*S_omega; %[m^2/rad/s] %Reponse spectrum
Sigmax = sqrt(trapz(omega, Sx_surge))  %[m] %Standard deviation
X_max = Sigmax*sqrt(2*log(N(k)))       %[m] %Maximum offset
S_omega_max = max(S_omega);            %[m^2/rad/s]  %Maximum value
Sx_max = max(Sx_surge)                 %[m^2/rad/s]  %Maximum value

S_omega_plot = fliplr(S_omega);
```

```
Sx_plot = fliplr(Sx_surge);

%% PLOTTING THE WAVE AND RESPONSE SPECTRUM
clf
p1 = plot(omega,S_omega,'-k');
grid on
hold on
p2 = plot(omega,Sx_surge,':r');
axis([0.5 4 0 1]);
xticks([0:0.4:4])
xticklabels(split(num2str(round(2*pi./xticks(),1))))
yticks([0:0.2:1])
set(gca,'linewidth',0.1);
set(gca,'FontSize',11);

p1.LineWidth = 1.5;
p2.LineWidth = 1.5;
```

Appendix D MATLAB code - Mean drift force

```
%% TOTAL MEAN DRIFT FORCE FROM NON DIMENSIONAL MEAN DRIFT COEFFICIENT

k = 6; %Counter for obtaining seastate
n = 5  %Counter for obtaining non dimensional mean drift force from WAMIT

%NON-DIMENSIONAL MEAN DRIFT FORCE FROM WAMIT SIMULATION
fid1= fopen([]);
fgetl(fid1);
data1 = textscan(fid1,'%f %f %f %d %f %f %f %f');
fclose(fid1);

Mean_all_surgeA = cell2mat(data1(n));
Mean_sA = Mean_all_surgeA(1:3:end)';  %Non-dimensional mean drift force

%REGULAR WAVE PARAMETERS
g = 9.81;                      %[m/s^2] %Acceleration of gravity
T = [0.1:0.1:15];              %[s]     %wave periods
del_T = 0.01;                  %[s]
omega = fliplr(2*pi()./T);     %[rad/s] %wave frequency
del_omega = diff(omega);       %[rad/s] %wave frequency
del_omega = [del_omega(1) del_omega]; %[rad/s]  %delta omega
omega_max = 2*pi/0.5;                 %[rad/s]  %omega max
omega_min = 2*pi/15;                  %[rad/s]  %omega min
h = 100;                              %[m]      %Water-depth
t_1 = 10800;                          %[s]      %Seastate duration
rho = 1025;                           %[kg/m3]  %Density of seawater

%WAVE AMPLITUDES FROM WAVE-SPECTRUMS
T_p = [2.0 3.0 4.0 5.0 6.0 6.7];       %[s]
omega_p = 2*pi()./T_p;                 %[rad/s]
H_s = [0.5 1.0 1.5 2.0 2.5 3.0];       %[m]

S_omega_DNV_2 = (5/16)*H_s(k)^2*omega_p(k)...
    ^4.*omega.^(-5).*exp(-(5/4).*(omega./omega_p(k)).^(-4));
S_integral = trapz(omega,S_omega_DNV_2);                       %[M^2/rad/s]
S_omega = ((H_s(k).^2)/16).*(1/S_integral).*S_omega_DNV_2; %[M^2/rad/s]

AmpN = sqrt(2*S_omega.*del_omega); %[m] %Wave amplitudes
AmpN_flip = fliplr(AmpN)           %[m] %Wave amplitudes

%CALCULATION OF TOTAL MEAN DRIFT FORCE
F_mean_i = zeros(size(AmpN));
for h = 1:numel(AmpN);
```

```
    F_mean_i(h) = AmpN_flip(h)^2*Mean_sA(h);
end

F_mean_total = (sum(F_mean_i)*rho*g)/1000
Mean_sA_max = max(Mean_sA)
AmpN_max = max(AmpN)
```

Appendix E MATLAB code - Current force

```matlab
%%FORCE FROM CURRENT CALCULATION

%CURRENT CONDITIONS SUBSTANTIAL
V = [0.0:0.1:1.0]; %[m/s] %Current velocity for substantial conditions
visk = 1.83e-06;
rho = 1025;
%DESIGN PARAMETERS
D = 40;
R = D/2;
H = [20 24 26 28];
A = 0.5*pi().*H*R;

%REYNOLDS NUMBER AND DRAG COEFFICIENT
Re = (V*D)/visk
ReMIN = Re(2)
ReMAX = Re(10)
Cd = 0.35;

F_current1 = (0.5*rho*Cd.*A(1).*V.^2)/1000 %[kN] %current forces D1
F_current2 = (0.5*rho*Cd.*A(2).*V.^2)/1000 %[kN] %current forces D2
F_current3 = (0.5*rho*Cd.*A(3).*V.^2)/1000 %[kN] %current forces D3
F_current4 = (0.5*rho*Cd.*A(4).*V.^2)/1000 %[kN] %current forces D4

%PLOT OF CURRENT FORCE AS FUNCTION OF CURRENT SPEED.
k1 = plot(V,F_current1,'--k');
grid on
hold on
k2 = plot(V,F_current2,'-k*');
hold on
k3 = plot(V,F_current3,'--ko');
hold on
k4 = plot(V,F_current4,'-k');
legend boxoff
k1.LineWidth = 1.2;
k2.LineWidth = 1.2;
k3.LineWidth = 1.2;
k4.LineWidth = 1.2;
```

References

[1] Mostafa Amini Afshar and Harry B Bingham. “Implementation of the far-field method for calculation of added resistance using a high order finite-difference approximation on overlapping grids”. In: *32nd International Workshop on Water Waves and Floating Bodies (IWWWFB 2017)*. 2017.

[2] Botngaard AS. *Closed technology*. http://www.botngaard.no/en/products. Accessed: 2019-02-02.

[3] Lovold AS. *Product catalogue 2016*. https://lovoldas.no/. Accessed: 06.05.2019.

[4] Marine Harvest ASA. *Salmon Farming Industry Handbook*. Marine Harvest, 2017.

[5] F Cardia and A Lovatelli. “Aquaculture operations in floating HDPE Cages, Chapter: Mooring and grid components”. In: *Rome: FAO and Ministry of Agriculture of the Kingdom of Saudi Arabia* (2015).

[6] Subrata Chakrabarti. *Handbook of Offshore Engineering (2-volume set)*. Elsevier, 2005.

[7] Subrata Kumar Chakrabarti. *Hydrodynamics of offshore structures*. WIT press, 1987.

[8] Pål Lader David Kristiansen and Vegard Aksnes. “Sjøegenskaper og forankring til flytende lukkede oppdrettsanlegg”. In: (2018).

[9] Qin De. http://www.qdrig.com. Accessed: 2019-06-02.

[10] W.Lian D.Myrhaug. *TMR 4180 Marine dynamics*. Department of marine technology - NTNU, 2009.

[11] Odd M Faltinsen and Arne E Løken. “Slow drift oscillations of a ship in irregular waves”. In: *Applied Ocean Research* 1.1 (1979).

[12] Odd Magnus Faltinsen. *Sealoads on ships and offshore structures*. The press syndicate of the university of Cambridge, 1990.

[13] Serge Ferrari. *Flexible semi closed cage systems (SCCS)*. www.sergeferrari.com. Accessed: 06.05.2019.

[14] FIS. *Cermaq starts farming in closed technology*. https://www.fis.com/fis/worldnews/worldnews. Accessed: 06.05.2019.

[15] A Fredheim and R Langan. “Advances in technology for off-shore and open ocean finfish aquaculture”. In: *New Technologies in Aquaculture*. Elsevier, 2009, pp. 924–925.

[16] Marilena Greco. *TMR 4215 Sealoads, Lecture notes*. Department of marine technology - NTNU, 2012.

[17] AKVA group. *Cage farming Aquaculture*. www.akvagroup.com. 2017.

[18] Indiamart. *HDPE and other plastic pipes*. ttps://www.indiamart.com/proddetail/140-mm-hdpe-pipe-12552414797.html/. Accessed: 2019-16-04.

[19] Stig Berge Jørgen Amdahl and Fredrik Dukan. *Havromsteknologi*. Fagbokforlaget Vigmostad og Bjørke AS, 2014, chapter2, 20–21.

[20] Jan Kvãlsvold. *Solution of exercises in the book ’Sea1oads on ship and offshore structures’ by Prof. O.Faltinsen*. Department of Marine Hydrodynamics - NTNU, 1993. Chap. Solution exercise 3.5.

[21] Pål Lader et al. “Drag forces on, and deformation of, closed flexible bags”. In: *Journal of Offshore Mechanics and Arctic Engineering* 137.4 (2015), p. 041202.

[22] Professor Kjell Larsen. *TMR4225 Marine Operations - Operability and weather windows*. Department of marine technology - NTNU, 2018.

[23] Professor Kjell Larsen. *TMR4225 Marine Operations - Station keeping and mooring of floating structures*. Department of marine technology - NTNU, 2018.

[24] C Lee and JN Newman. “Computation of wave effects using the panel method”. In: *Numerical Models in Fluid Structure Interaction* 42 (2005), pp. 211–251.

[25] Chang Ho Lee and John Nicholas Newman. “WAMITő User Manual, Versions 6.3, 6.3 PC, 6.3 S, 6.3 S-PC”. In: *WAMIT, Inc., Chestnut Hill, MA, USA* (2006).

[26] Hajime Maruo. “The Drift on a Body Floating in Waves”. In: *J. Ship Res.* 4.3 (1960), pp. 1–10.

[27] P McIver. “Sloshing frequencies for cylindrical and spherical containers filled to an arbitrary depth”. In: *Journal of Fluid Mechanics* 201 (1989), pp. 243–257.

[28] Jewel machinery Mooring Hardware Supplier. https://www.qdjwm.com/product-detail/plough-anchor/. Accessed: 2019-04-02.

[29] Ida M.Strand. *Sea loads on closed flexible fish cages*. NTNU - Norwegian University of science and technology), 2018.

[30] Jack A. Myers. *Handbook of equations for mass and area properties of various geometrical shapes*. NOTS technical publication, 1966. Chap. Solids, Thin shells.

[31] NASA. *Conservation of momentum*. https://www.grc.nasa.gov/www/k-12/airplane/conmo.html. Accessed: 2018-04-10.

[32] JN Newman. “Algorithms for the free-surface Green function”. In: *Journal of engineering mathematics* 19.1 (1985), pp. 57–67.

[33] Finn Gunnar Nielsen. *Lecture notes in marine operations*. Department of hydrodynamics - department of marine engineering - NTNU, 2007.

[34] NTNU. *Mooring of Aquaculture structures, Lecture presentation TMR4140, NTNU*. 2017.

[35] Alexander N. Timokha O.M.Faltinsen. *Sloshing*. Cambridge university press, 2009.

[36] Bjørnar Pettersen. *Marine dynamics compendium*. Department of marine technology - NTNU, 1990.

[37] Trond Waldemar Rosten et al. “Oppdrett av laks og ørret i lukkede anlegg-forprosjekt”. In: *SINTEF, Trondheim* (2011).

[38] Hermann Schlichting and Klaus Gersten. *Boundary-layer theory*. Springer, 2016.

[39] The Fish Site. *hackle cage mooring hardware*. https://thefishsite.com/articles/vonin-and-crosby-join-forces-on-cage-mooring-hardware/. Accessed: 2019-06-02.

[40] Sjøfartsdirektoratet. *Oversikt over alle forskningstillatelsene til matfiskoppdrett av laks, ørret og regnbueørret.* https://fiskeridir.no/iphone/Akvakultur/Tildeling-og-tillatelser/Saertillatelser/Forskningstillatelser-FoU/Alle-forskningstillatelsene. Accessed: 2018-04-11.

[41] Global Sources. https://www.globalsources.com/gsol/I/PP-rope/p/sm/1160154960. Accessed: 2019-04-02.

[42] Global Sources. https://www.globalsources.com/gsol/I/PP-rope/p/sm/1160197340. Accessed: 2019-04-02.

[43] Norsk Standard. *Flytende oppdrettsanlegg: Krav til utforming, dimensjonering, utførelse, installasjon og drift*. 2003.

[44] B Mutlu Sumer et al. *Hydrodynamics around cylindrical strucures*. Vol. 26. World scientific, 2006.

[45] Seamaster Commercial Fishing Supplies. https://pfg-group.com.au/seamaster/. Accessed: 2019-06-02.

[46] Det Norske Veritas. “Modelling and analysis of marine operations”. In: *Offshore Standard* (2011).

NTNU
Kunnskap for en bedre verden